INVESTIGATION OF ION DYNAMICS OF DEVICES WITH IONIC LIQUID MIXTURE ELECTROLYTES USING X-RAY PHOTOELECTRON SPECTROSCOPY WITH ELECTRICAL BIASING

A THESIS SUBMITTED TO
THE GRADUATE SCHOOL OF ENGINEERING AND SCIENCE
OF BILKENT UNIVERSITY
IN PARTIAL FULFILLMENT OF THE REQUIREMENTS FOR
THE DEGREE OF
MASTER OF SCIENCE
IN CHEMISTRY

By
Ezgi Kutbay

July 2025

INVESTIGATION OF ION DYNAMICS OF DEVICES WITH IONIC LIQUID MIXTURE ELECTROLYTES USING X-RAY PHOTOELECTRON SPECTROSCOPY WITH ELECTRICAL BIASING

By Ezgi Kutbay

July 2025

We certify that we have read this thesis and that in our opinion it is fully adequate, in scope and in quality, as a thesis for the degree of Master of Science.

_____

Şefik Süzer (Advisor)

_____

Mehmet Fatih Danışman

_____

Burak Ülgüt

_____

Pınar Aydoğan Göktürk

_____

Halil İbrahim Okur

Approved for the Graduate School of Engineering and Science:

_____

Orhan Arıkan

Director of Graduate School

ABSTRACT

INVESTIGATION OF ION DYNAMICS OF DEVICES WITH IONIC LIQUID MIXTURE ELECTROLYTES USING X-RAY PHOTOELECTRON SPECTROSCOPY WITH ELECTRICAL BIASING

Ezgi Kutbay

M. Sc. in Chemistry

Advisor: Prof. Dr. Şefik Süzer

July, 2025

X-ray Photoelectron Spectroscopy (XPS) has long been used to investigate surface composition, chemical states, and electronic environments in materials. In this study, XPS is employed not only for these traditional roles but also to extract local electrical potential profiles by monitoring shifts in core-level binding energies under applied DC and/or AC biases. Two complementary device architectures are utilized to achieve this objective: (i) platinum–platinum (Pt–Pt) coplanar capacitors, which are well-suited for investigating frequency-dependent charge screening, potential drop across the ionic liquid (IL) layer, and circuit modeling under square-wave excitation; and (ii) multilayer graphene–multilayer graphene (MLG–MLG) devices, which are employed to explore electrosorption dynamics, open-circuit potential (OCP) effects, and residual charge behavior after shorting. A Square Wave (SQW) AC signal with varying frequencies was employed to resolve dynamic charging and discharging processes in these systems.

The co-planar capacitor configuration used was featuring a polyethylene membrane (PEM) coated with either the ionic liquid N,N-Diethyl-N-methyl-N-(2-methoxyethyl)ammonium bis(trifluoromethanesulfonyl)imide (DEME-TFSI) alone, or a ~1:1 volume mixture of DEME-TFSI and N,N-Diethyl-2-methoxy-N-methylethanaminium tetrafluoroborate (DEME-BF4). The measurements were conducted under *operando* conditions, allowing simultaneous acquisition of XPS spectra and current data. Although ionic liquids offer advantages such as wide electrochemical windows and thermal stability, their high viscosity and cost can hinder ionic mobility and conductivity. A promising approach to address these limitations involves mixing different ILs to tailor their properties; for example, adjusting the ratio of DEME-TFSI and DEME-BF4 alters electrolyte characteristics. The pronounced size difference between the TFSI and BF4 anions provides an opportunity for detailed investigation via XPS. Additionally, a DEME-TFSI system containing ~10% rubidium bis(trifluoromethanesulfonyl)imide (Rb-TFSI) was explored to assess the influence of a small, mobile alkali cation (Rb^+) on surface composition and charge storage. XPS revealed polarity-sensitive surface accumulation of Rb^+, correlating with a sharp increase in currents. Overall, this non-invasive methodology, leveraging both Pt–Pt and MLG–MLG architectures, demonstrates that XPS is a powerful tool for probing local electrochemical processes. The technique offers valuable insights that can contribute to the development of next-generation energy harvesting and storage systems.

Key Words: *operando* X-Ray Photoelectron Spectroscopy, Ionic liquids, AC/DC modulation

ÖZET

ELEKTROLİT OLARAK İYONİK SIVI KARIŞIMI İÇEREN CİHAZLARDAKİ İYON DİNAMİKLERİNİN ELEKTRİKSEL MODÜLASYON ALTINDA X-IŞINI FOTOELEKTRON SPEKTROSKOPİSİ İLE İNCELENMESİ

Ezgi Kutbay

Kimya, Yüksek Lisans

Tez Danışmanı: Prof. Dr. Şefik Süzer

Temmuz, 2025

X-Işını Fotoelektron Spektroskopisi (XPS), uzun zamandır malzemelerin yüzey bileşimi, kimyasal konumları ve elektronik ortamlarını incelemek için kullanılmaktadır. Bu çalışmada ise XPS, yalnızca bu geleneksel amaçlar için değil, aynı zamanda uygulanan AC ve/veya DC gerilimleri altında iç yörüngelerindeki elektronların bağlanma enerjilerindeki kaymaları izleyerek yerel potansiyel profillerini ortaya çıkarmak amacıyla da kullanılmıştır. Bu hedefe ulaşmak için iki tamamlayıcı cihaz mimarisi seçilmiştir: (i) frekansa bağlı yük taramasını, iyonik sıvı tabakası boyunca potansiyel düşüşünü ve kare dalga uyarımı altında devre modellerini oluşturmak için uygun olan platin-platin (Pt -Pt) düzlemsel elektrot kapasitörler; ve (ii) elektrosorpsiyon dinamiklerini, açık devre potansiyeli (OCP) etkilerini ve kısa devre sonrasında kalan yük davranışını incelemek için kullanılan çok katmanlı grafen – çok katmanlı grafen (MLG-MLG) elektrot içeren aygıtlar. Bu sistemlerdeki dinamik şarj ve deşarj süreçlerini çözümlemek için değişen frekanslarda kare dalga (SQW) AC sinyali uygulanmıştır.

Düzlemsel kapasitör yapılandırması, iki elektrotu birleştiren polietilen membran (PEM) üzerine N,N-Dietil-N-metil-N-(2-metoksietil)amonyum bis(trifloromethansülfonil)imid (DEME-TFSI) iyonik sıvısı veya DEME-TFSI ile N,N-Dietil-2-metoksi-N-metiletanamonyum tetrafloroborat (DEME-BF4) iyonik sıvısının ~1:1 hacim karışımı ile kaplanarak elde edilmiştir. Ölçümler XPS spektrumları ile akım verilerinin eşzamanlı olarak kaydedilmesini sağlayan *in-operando* koşullarda gerçekleştirilmiştir. İyonik sıvılar, geniş elektrokimyasal pencere ve termal ve kimyasal kararlılık gibi avantajlar sunar, ancak yüksek viskoziteleri iyon hareketliliğini ve iletkenliğini kısıtlamaktadır. Bu olumsuzlukları aşabilmek için farklı iyonik sıvıların karıştırılması ve özelliklerinin istenilen şekilde ayarlanması planlanmıştır. Bu amaçla, DEME-TFSI ve DEME-BF_4 karışımı hazırlanmış ve TFSI ile BF4 anyonları arasındaki belirgin boyut farkının cihaz davranışına etkileri XPS yoluyla ayrıntılı olarak incelemiştir. Ayrıca, küçük bir katyon olan Rb'un yüzey bileşimi ve yük depolama üzerindeki etkisini değerlendirmek amacıyla yaklaşık %10 oranında Rb-TFSI içeren bir DEME-TFSI karışımı incelenmiştir. XPS ölçümleri, Rb^+ iyonlarının uygulanan voltajın polaritesine duyarlı şekilde yüzeyde biriktiğini göstermiştir. Bu durum, akımda gözlenen artış ile de uyumludur. Sonuç olarak, hem Pt-Pt hem de MLG-MLG mimarilerini kullanan bu metodoloji, XPS'in yerel elektrokimyasal süreçleri incelemede güçlü bir araç olduğunu göstermiştir. Bu teknik, gelecek nesil enerji toplama ve depolama sistemlerinin geliştirilmesine önemli katkılarda bulunabilecek yeni bilgiler sunmaktadır.

Anahtar Sözcükler: *operando* X-Işını Fotoelektron Spektroskopisi, İyonik sıvılar, AC/DC modülasyonu

Acknowledgement

I would like to begin by expressing my deepest gratitude to my thesis advisor and chemistry hero, Prof. Şefik Süzer. Şefik Hocam, you have taught me more than anyone ever could. I deeply cherish the discipline and confidence you instilled in me throughout this journey. Your mentorship has shaped not only my scientific thinking and my approach to research and academic life but has also had a profound impact on my personal growth. I am honored to have been one of your students and will carry your teachings with me always.

I am also thankful to Assoc. Prof. Burak Ülgüt and Prof. Coşkun Kocabaş for their contributions and support to our research. To my thesis committee members, Asst. Prof. Pınar Aydoğan Göktürk whose work before me in Süzer Lab gave me guidance, Asst. Prof. Halil İbrahim Okur for his immense support and generous teaching and Assoc. Prof. Mehmet Fatih Danışman for his valuable feedback and suggestions – thank you.

I would also like to acknowledge the Scientific and Technological Research Council of Türkiye (TÜBİTAK) for their financial support through project number 223Z097.

To the ones closest to my heart: my parents. Your strength and belief in me have made me, me. I will never forget the lessons you have taught me — most of all, that a woman should always stand on her own. I wish for many healthy, happy days together. I am also incredibly grateful to my aunts and cousins whose constant support always remind me that I am not alone.

To my dearest friends, Umut and Özlem, thank you for growing up with me and seeing me through every phase of life and grounding me in who I am. And to my one and only group member, Süleyman, who is always one call away even when he is 8082 km away from me. Your unwavering support has been one of the main reasons I've been able to keep following my dreams. Without your willingness to help, I might have given up long ago.

To the friends I officially met during this wild ride we call graduate school, Yaren and Ertan, thank you for being my home not so much away from home. From the day we met by the door in 101/1, you've been a constant source of laughter, warmth and comfort. You've seen me at my most exhausted and most ecstatic, and I believe that I have found lifelong friends with you.

Finally, with all my heart, I thank my best friend, Umut Mert, who has been by my side through this journey and hopefully many more to come. Thank you for being in my life and simply being you.

I dedicate this thesis to my mom, who has been through so much in the past couple of years and yet still finds a way to keep on smiling. I love you the most.

Table of Contents

Chapter 1

1. Introduction 1

1.1 **X-Ray Photoelectron Spectroscopy 1**

1.1.1 Principles of X-Ray Photoelectron Spectroscopy 1

1.1.2 Common Applications of XPS 6

1.1.3 Local Potential Developments under DC/AC Bias 8

1.1.3.1 Operando-XPS 11

1.1.3.2 Electrical Double Layer: Concept and Significance ... 12

1.2 Analyzing Liquid Surfaces with XPS 13

1.3 Ionic Liquids: Structure, Properties and Applications 15

1.4 Frequency-Modulation Techniques in Electrochemical Probing 19

1.4.1 Square-Wave and Other AC Modulations 20

1.5 Aim of the Study 23

Chapter 2

2. Experimental Methodology 25

2.1 Materials 25

2.2 Device Design 26

2.2.1 Coplanar Capacitor Geometry 26

2.2.2 Pt-Pt Devices 26

2.2.3 Multilayer Graphene-Multilayer Graphene Devices 27

2.2.3.1 Pure DEME-TFSI Device 27

2.2.3.2 10% Rb-TFSI – 90 %DEME-TFSI Device 28

2.3 Instrumentation 29

2.3.1 Characterization Techniques 29

2.3.1.1 X-Ray Photoelectron Spectroscopy 29

2.3.1.2 Electrical Biasing and Current Measurement Set-up .. 33

2.3.1.3 Electrical Impedance Spectroscopy and Equivalent Circuit Modeling 33

Chapter 3

3. Results and Discussion: Pt-Pt Devices 35

3.1 Current Measurements 35
3.1.1 Current-Time Measurements 35
3.1.2 Current-Voltage Measurements 37
3.2 AC Biasing and Circuit Modelling 38
3.2.1 High and Low Frequency AC Response 38
3.2.2 Incorporating Series-Resistors: Quantifying R & C 41
3.2.3 Electrical Impedance Spectroscopy 48
3.2.4 Equivalent Circuit Modelling 50
3.2.5 Comparison of Pure IL Devices and IL Mixtures 53

Chapter 4

4. Results and Discussion: MLG-MLG Devices 57
4.1 Device Containing DEME-TFSI 57
4.1.1 Time-Resolved XPS: Dynamics of Charging and Discharging 57
4.1.2 Effect of Open-Circuit Potential 60
4.1.3 Ionic Charge Retention After Shorting 61
4.1.4 Asymmetric Charge Accumulation and Capacitance Behavior 64
4.2 Impact of Rb^+ Inclusion on Electrosorption and Surface Composition 68

Chapter 5

5. Conclusions 78

Bibliography 81

List of Figures

Figure 1. Schematic representation of the basic working principle of X-ray Photoelectron Spectroscopy (XPS) 3

Figure 2. XPS Survey Spectrum of gold (Au) displaying both core-level and Auger peaks, along with high resolution spectrum of the Au4f region 4

Figure 3. The energy level diagram showing that the Fermi levels of the sample and the spectrometer are aligned so that the work function of the spectrometer can be used to compute the binding energies from the measured kinetic energies. 5

Figure 4. Energy level diagram showing that under positive bias, the measured binding energy is equal to the binding energy of the unbiased sample and the applied voltage. 9

Figure 5. The XP spectrum of Pt4f at ground level (olive), under +3V(red) and under -3 V (blue) external DC bias 10

Figure 6. Some common cations and anions that are used by IL manufacturers 16

Figure 7. (a) XPS Survey Spectrum of the IL, DEME-TFSI. (b) Structure of DEME cation. (c) Structures of TFSI and BF_4 anions. (d) XPS Survey Spectrum of IL mixture, 1:1 (v/v) DEME-TFSI: DEME- BF_4 19

Figure 8. XPS Spectrum of the F1s region of a IL coplanar device under 3 V SQW 10 kHz; the grounded spectrum splits into two and the characteristic “twin peak” structure is seen, where the separation between the peaks reflect the full bias voltage applied…….21

Figure 9. Comparison of XPS spectra of a IL coplanar device under 3 V SQW AC bias at (a) 10 kHz and (b) 0.1 Hz. The accompanying schematic highlights the time spent at each voltage level for these frequencies—while illustrating how at 10 kHz, the ions remain effectively immobile while the longer duration at 0.1 Hz allows ionic rearrangement on the surface. 22

Figure 10. Schematic representation of the Pt-Pt IL coplanar device used in this study 27

Figure 11. Schematic Representation of MLG-MLG IL coplanar device (side view) 28

Figure 12. XPS data acquisition locations on the Pt-Pt device. Points are highlighted with red dots. a and b correspond to the soldering joints, while positions 1 through 5 indicate the sites where F1s spectra were collected 30

Figure 13. (a) Two-dimensional (2D) time-resolved color map showing the evolution of O1s core-level spectra over 9000 consecutive acquisitions with temporal resolution of 0.5 seconds collected at point NE. (b) Three-dimensional (3D) plot of the same dataset showing how the intensity and the position of the peak shift over the 9000 iterations. 31

Figure 14. Schematic representation of the XPS measurement configuration, with the source and drain electrodes identified. 32

Figure 15. Schematic of coplanar Pt–Pt device under applied voltage to point 2. F 1s XPS spectra collected at the source electrode under +3 V, –3 V DC bias, and 0 V (no bias). Voltage-dependent response is highlighted. 33

Figure 16. Current-time Measurements. (a) Normalized current vs. time from 0.125 V to 2.5 V, (b) Normalized current vs. time in log-log scale at the same voltage values, (c) Accumulated Charge vs square root of time at same voltage values, (d) Same plot as in 12(c) but zoom in on 0-2 s interval 36

Figure 17. Cyclic voltammetry measured between ±0.125 V to ±3.0 V (a) Measured, (b) Normalized to 1 V. (Reprinted with permission from Karaoglu, G., Kutbay, E., Ince, S., Ulgut, B., and Suzer, S. Assessing Local Electrical Properties of Ionic Liquid/Metal Interfaces with Operando-XPS and by Incorporating Additional Circuit Elements. *Anal Chem* 2023, *95* (40), 14861–14869. Copyright 2023, American Chemical Society.) 38

Figure 18. (a) Schematic of the ionic liquid (IL) device with local points near the electrified electrode (NE) and near the grounded electrode (NG) highlighted in orange. (b) Local XPS response at NE and NG under ±2.5 V square-wave (SQW) bias at 10 kHz, with the corresponding line scan profile shown in the center. (c) Local XPS response at NE and NG under ±2.5 V SQW bias at 0.1 Hz, with the corresponding line scan profile shown in the center. (Adapted with permission from Karaoglu, G., Kutbay, E., Ince, S., Ulgut, B., and Suzer, S. Assessing Local Electrical Properties of Ionic Liquid/Metal Interfaces with Operando-XPS and by Incorporating Additional Circuit Elements. *Anal Chem* **2023**, *95* (40), 14861–14869. Copyright 2023, American Chemical Society.) 40

Figure 19. (a) Schematic of the ionic liquid (IL) device with 2 additional resistors of 150 kOhm resistance with local points near the electrified electrode (NE) and near the grounded electrode (NG) highlighted in orange. (b) Local XPS response at NE and NG under ±2.5 V square-wave (SQW) bias at 10 kHz, with the corresponding line scan profile shown in the center. (c) Local XPS response at NE and NG under ±2.5 V SQW bias at 0.1 Hz, with the corresponding line scan profile shown in the center. (Adapted with permission from Karaoglu, G., Kutbay, E., Ince, S., Ulgut, B., and Suzer, S. Assessing Local Electrical Properties of Ionic Liquid/Metal Interfaces with Operando-XPS and by Incorporating Additional Circuit Elements. Anal Chem 2023, 95 (40), 14861–14869. Copyright 2023, American Chemical Society.)..... 44

Figure 20. (a) F1s spectra of the IL device at points 1 and 2, without series resistors. (b) F1s spectra of the IL device, with two 150 kΩ series resistors integrated, in points 1 and 2. (Adapted from Kutbay, E., Ince, S. and Suzer, S. AC-Modulated XPS Enables to Externally Control the Electrical Field Distributions on Metal Electrode/Ionic Liquid Devices. Journal of Physical Chemistry B 2024, 128 (17), 4139–4147. Copyright 2024, American Chemical Society.) 45

Figure 21. (a) F1s spectra of the IL device at points **1** and **2**, with one resistor placed before and one resistor placed after the IL device. (b) F1s spectra of the IL device, with two 150 kΩ series resistors placed after the IL device, collected in points **1** and **2**. (Adapted from Kutbay, E., Ince, S. and Suzer, S. AC-Modulated XPS Enables to Externally Control the Electrical Field Distributions on Metal Electrode/Ionic Liquid

Devices. Journal of Physical Chemistry B 2024, 128 (17), 4139–4147. Copyright 2024, American Chemical Society.) 46

Figure 22. F1s region's XP Spectra. Under 2.5 V SQW Excitations and with the additional 150 kOhm Resistor: Inside and Outside the spectrometer, together with the grounded one. (a) 10 kHz, (b) 0.1 Hz. (Reprinted with permission from Karaoglu, G., Kutbay, E., Ince, S., Ulgut, B., and Suzer, S. Assessing Local Electrical Properties of Ionic Liquid/Metal Interfaces with Operando-XPS and by Incorporating Additional Circuit Elements. *Anal Chem* **2023**, *95* (40), 14861–14869. Copyright 2023, American Chemical Society.) 47

Figure 23. Electrochemical impedance spectroscopy (EIS) results for three distinct configurations of the device: (i) the IL device in its original state (black), (ii) after over 8 hours of X-ray exposure (red), and (iii) after adding external resistors (blue). (a) Nyquist plots displaying the real and imaginary parts of the impedance, with the external resistors clearly identified as 290 kΩ. (b) Impedance magnitude as a function of frequency for the three configurations, showing a significant decrease from 1.0 MΩ at 0.1 Hz to 10 kΩ at 10 kHz. (c) The equivalent circuit model used and the electrical parameters for each of the device configurations. (Reprinted with permission from Karaoglu, G., Kutbay, E., Ince, S., Ulgut, B., and Suzer, S. Assessing Local Electrical Properties of Ionic Liquid/Metal Interfaces with Operando-XPS and by Incorporating Additional Circuit Elements. *Anal Chem* **2023**, *95* (40), 14861–14869. Copyright 2023, American Chemical Society.)..... 49

Figure 24. Equivalent Circuit Model of the Pt-Pt coplanar capacitor device with two resistors (one after and one before IL device). (Adapted from Kutbay, E., Ince, S. and Suzer, S. AC-Modulated XPS Enables to Externally Control the Electrical Field Distributions on Metal Electrode/Ionic Liquid Devices. Journal of Physical Chemistry B 2024, 128 (17), 4139–4147. Copyright 2024, American Chemical Society.)..... 51

Figure 25. Synthetic spectra acquisition process starting from the acquisition of voltage response at 10 kHz and 0.1 Hz 4 V SQW voltage, the convolution process and the generation of synthetic spectra. (Adapted from Kutbay, E., Ince, S. and Suzer, S. AC-Modulated XPS Enables to Externally Control the Electrical Field Distributions

on Metal Electrode/Ionic Liquid Devices. Journal of Physical Chemistry B 2024, 128 (17), 4139–4147. Copyright 2024, American Chemical Society.) 52

Figure 26. Synthetic spectra collected at points indicated by a green star IL device with (a) 2 resistors placed in the front, (b) 2 resistors placed at the back, (c) one resistor placed in the front and one at the back at 10 kHz and 0.1 Hz 4 V SQW voltage. (Adapted from Kutbay, E., Ince, S. and Suzer, S. AC-Modulated XPS Enables to Externally Control the Electrical Field Distributions on Metal Electrode/Ionic Liquid Devices. Journal of Physical Chemistry B 2024, 128 (17), 4139–4147. Copyright 2024, American Chemical Society.) 53

Figure 27. (a) Structure of the cation, $DEME^+$. (b) Structure of the anions, $TFSI^-$ and BF_4^-. (c) F1s grounded spectrum of the 1:1.4 (v:v) DEME-TFSI:DEME-BF_4 mixture with the areas of the two peaks corresponding to TFSI (cyan) and BF_4 (orange). The average volumes of the ions were calculated from average diameter simulation results of Kim *et al*. 54

Figure 28. Schematic representation of the Pt-Pt device coated wih mixture of DEME-TFSI and DEME-BF_4: (a) without external resistors and (b) one resistor placed at the front and one at the end. Local XPS responses of F1s were recorded at points 1 and 2 under 4.0 V SQW AC modulation at 10 kHz (wine), 0.1 Hz (royal) along with the corresponding grounded spectrum (olive). (Adapted from Kutbay, E., Ince, S. and Suzer, S. AC-Modulated XPS Enables to Externally Control the Electrical Field Distributions on Metal Electrode/Ionic Liquid Devices. Journal of Physical Chemistry B 2024, 128 (17), 4139–4147. Copyright 2024, American Chemical Society.)..... 55

Figure 29. Biexponential fit of the O1s binding energy decay on the source electrode under +2 V bias. The 2 time constants, 20 seconds (slow) and 200 seconds (slower), reflect the fast electronic screening and slower ionic rearrangement at the electrical double layer respectively..... 58

Figure 30. Current response of the MLG-MLG device under cyclic (a) +2 V bias, (b) -2 V bias. The fluctuations (sudden increase/decrease) in current correlate with the O1s

binding energy shifts observed via XPS, highlighting the interplay of electronic and ionic processes during charging/discharging 59

Figure 31. Evolution of O1s binding energy: on the source electrode (a) under +2 V bias. (b) under -2 V bias; on the drain electrode (c) under +2 V bias and (d) under –2 V bias. The slow decay towards equilibrium without polarity reversal under OCP conditions confirms that ionic relaxation dominates once the external bias is removed. The abrupt change in B.E. after shorting reflects the rapid electronic neutralization...60

Figure 32. Mechanistic visualization for polarity reversal on the source electrode upon shorting, after application of +2.0 V 63

Figure 33. (a) Current measurements under -0.5 V and +0.5 V bias for a duration of 150 s each. The initial currents are shown with olive data points, which increase after application of -2.0 V bias for a duration of 30 minutes (1800 s) and becomes asymmetric (orange). Application of +2V bias for the same duration also causes an increase in currents and creates asymmetry in the opposite direction (purple). (b) Zoomed-in view of 150-300 s region from the current-time curve shown in (a). (c) The same 150-300 second current data presented on a logarithmic log(current) scale. ... 65

Figure 34. EIS Measurements before and after Cycling for 14 hours. (a) Nyquist plots before (black) and after (red) cycling. Bode plots (c) Before and (d) After cycling . 67

Figure 35. (a) Molecular structure of the DEME cation, TFSI anion and Rb cation. (b) XPS survey spectrum of the DEME-TFSI containing 10% Rb-TFSI mixture, showing peaks that are identified as C1s, N1s, F1s and Rb3d. 68

Figure 36. (a) Summary of positive voltage ramping at the electrified electrode (point NE), showing progressive binding energies of Rb3d, C1s, N1s and F1s going from left to right displayed in 2D. (b) Corresponding spectra at the grounded electrode (point NG). (c) Negative voltage ramping results at point NE. (d) Negative voltage ramping response at point NG. 70

Figure 37. (a) Binding energy shifts with respect to the grounded state (0 eV); (b) Evolution of atomic percentages for Rb3d, cationic N1s, N^+ and anionic N^- during the

positive voltage ramping at point NE; (c) Binding energy shifts with respect to the grounded state (0 eV); (d) Evolution of atomic percentages for Rb3d, cationic N1s, N^+ and anionic N^- during the positive ramping at point NG. 72

Figure 38. C1s region at point NG. Spectra acquired when the coplanar capacitor is grounded (olive) and under +2.5 V bias (red). 73

Figure 39. (a) Binding energy shifts with respect to the grounded state (0 eV); (b) Evolution of atomic percentages for Rb3d, cationic N1s, N^+ and anionic N^- during the negative voltage ramping at point NE; (c) Binding energy shifts with respect to the grounded state (0 eV); (d) Evolution of atomic percentages for Rb3d, cationic N1s, N^+ and anionic N^- during negative ramping at point NG. 75

Figure 40. Current–time response of the MLG–MLG device containing DEME-TFSI with 10% Rb-TFSI before and after voltage cycling. 76

List of Tables

Table 1. Impedance values estimated from Sn3d binding energy differences at soldering points a and b at different frequencies, 10 kHz and 0.1 Hz. 43

List of Abbreviations

AC: Alternating Current

AES: Auger Electron Spectroscopy

AP-XPS: Ambient Pressure X-Ray Photoelectron Spectroscopy

AR-XPS: Angle Resolved X-Ray Photoelectron Spectroscopy

ATR-IR: Attenuated Total Reflectance Infrared Spectroscopy

BE: Binding Energy

CV: Cyclic Voltammetry

CVD: Chemical Vapor Deposition

DC: Direct Current

DEME-BF_4: *N,N*-Diethyl-*N*-methyl-*N*-(2-methoxyethyl) ammonium tetrafluoroborate

DEME-TFSI: *N,N*-Diethyl-*N*-methyl-*N*-(2-methoxyethyl) ammonium bis (trifluoromethanesulfonyl) imide

EDL: Electrical double layer

EIS: Electrical Impedance Spectroscopy

ESCA: Electron Spectroscopy for Chemical Analysis

IL : Ionic Liquid

IR drop : Voltage drop

MLG: Multilayer Graphene

NE: Near Electrified Electrode

NG: Near Grounded Electrode

OCP: Open-Circuit Potential

PEM: Polyethylene membrane

Rb-TFSI: Rubidium bis (trifluoromethanesulfonyl) imide

SAMs: Self-Assembled Monolayer

SEI: Solid Electrolyte Interface

SIMS: Secondary Ion Mass Spectrometry

SIN: Sinusoidal wave

SQW: Square wave

UHV: Ultra-High Vacuum

XPS: X-Ray Photoelectron Spectroscopy

Chapter 1

1. Introduction

1.1 X-Ray Photoelectron Spectroscopy

1.1.1 Principles of X-Ray Photoelectron Spectroscopy

X-Ray Photoelectron Spectroscopy (XPS) is a quantitative surface analysis technique that relies on the photoelectric effect to investigate the elemental composition, chemical states, and local electronic environments of material surfaces.[1–4] XPS, also known as ESCA (Electron Spectroscopy for Chemical Analysis), was developed in Sweden at the University of Uppsala by the group of Kai Siegbahn during the 1950s. Their pioneering work between the years 1955 and 1970 laid the foundation for electron spectroscopy. For this contribution, Siegbahn was awarded the Nobel Prize in Physics in 1981.[5,6] With its high resolving power, XPS enabled scientists to analyze core-electron energies with an unprecedented level of detail. Since the 2000s, improvements have been made to X-Ray sources, detectors and fast electronics that have pushed the energy resolution under 200 meV while shortening the data acquisition time, giving platform for new time-resolved experiments.[7–10] The technique has since evolved significantly, both in terms of instrumentation and application, and has become an essential tool for understanding the chemical and electrical properties of surfaces and interfaces across a wide range of disciplines.[11,12] Modern instruments – from time-of-flight and imaging analyzers to ambient pressure cells have broadened the reach of XPS, making it available for use in materials science, catalysis, energy storage and biology.[13,14]

The foundational advantage of XPS lies in its ability to probe the chemical state and composition of a material's surface by measuring the kinetic energies of core electrons ejected upon X-ray irradiation, a process enabled by the photoelectric effect. When a sample is irradiated with a monochromatic X-ray source, such as Al Kα (1486.6 eV) or Mg Kα (1253.7 eV), photons interact with core-level electrons in the atoms throughout the top few nanometers. If the photon energy exceeds the binding energy of a core electron, the electron is ejected from the atom and its kinetic energy is measured by a hemispherical kinetic energy analyzer, yielding precise binding energy measurements.[1]

The binding energy (BE) of each ejected photoelectron is determined by the following relation:

$$BE = h\vartheta - KE - \varphi$$

where hν is the incident photon energy, KE is the measured kinetic energy of the detected electrons, and φ is the spectrometer's work function. Since each element has a characteristic set of core-level binding energies, and these energies shift slightly depending on the chemical and physical environment (e.g., oxidation state, local bonding, liquid and/or solid environment etc.), XPS can provide highly specific chemical and electrical information.[15,16]

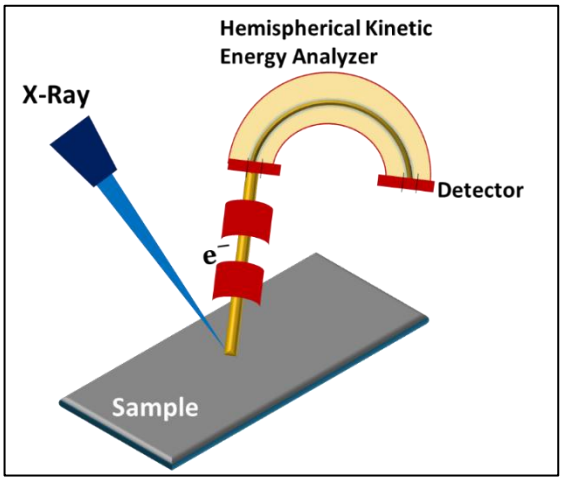

Figure 1. Schematic representation of the basic working principle of X-ray Photoelectron Spectroscopy (XPS).

XPS is particularly powerful because it can detect nearly all elements in the periodic table—excluding hydrogen, which lacks core electrons that can be accessed by typical laboratory X-ray sources. Moreover, the technique is inherently surface-sensitive. Although X-rays can penetrate into the bulk of the material (micrometer penetration depth), the emitted photoelectrons are strongly scattered by inelastic interactions as they travel through the solid, liquid or gaseous environment. As a result, inelastic scattering enforces detection (i.e. without any loss of energy) to the top 1-10 nm.[17] Therefore, only the photoelectrons in this depth can escape without energy loss and contribute to the characteristic sharp peaks observed in an XPS spectrum, allowing accurate determination of elemental identity and chemical state. Electrons that undergo inelastic scattering before escaping contribute to the spectral background rather than the well-defined peaks.

Typically, two types of spectra are recorded in XPS measurements: survey and high-resolution scans. The survey spectrum, characterized by its broad energy range of 1 to 1400 eV, is taken at lower energy resolution and provides an overview of the surface composition, showing distinct peaks for each detectable element. In contrast,

high-resolution spectra focus on a narrower binding energy range to reveal fine details (such as peak area, height etc.) to provide information about the chemical states of specific elements.

Figure 2 presents the survey spectrum of gold, acquired with a pass energy of 200 eV, and the high-resolution spectrum of Au4f, acquired with a pass energy of 50 eV. In the survey spectrum, emissions from core levels as well as X-ray induced Auger peaks at higher binding energies beyond 1200 eV are observed. The Auger electron emission occurs when an electron from a higher energy level fills a vacancy in a core level, created by the ejected photoelectrons. The energy released during this relaxation, is transferred to the "Auger" electrons which are emitted from the atom. The kinetic energy of Auger electrons is independent of the X-ray source energy, but their binding energy positions vary with the energy of the X-ray source used. [18]

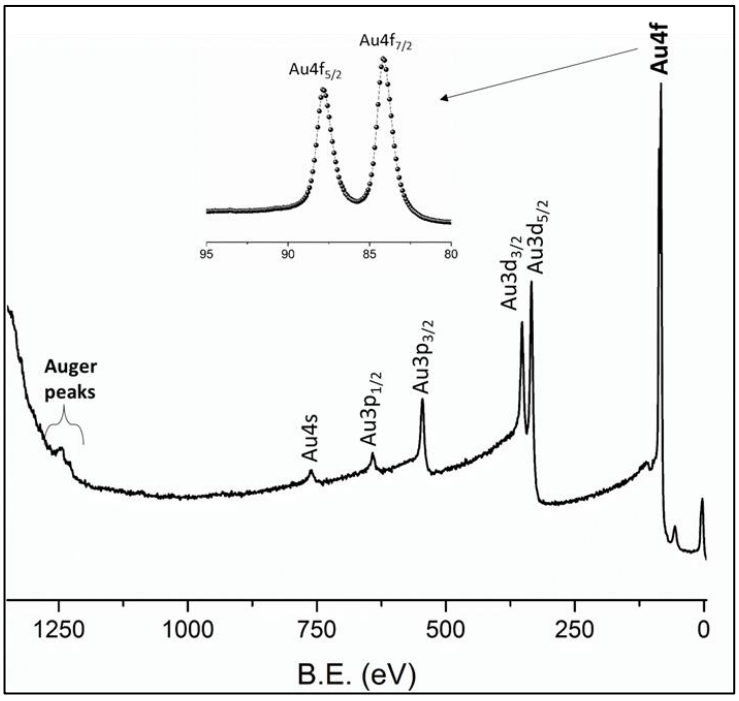

Figure 2. XPS Survey Spectrum of gold (Au) displaying both core-level and Auger peaks, along with high resolution spectrum of the Au4f region.

To understand how binding energies are referenced in XPS, Figure 3 depicts the Fermi-level alignment that occurs when a conductive sample is electrically connected to the grounded spectrometer. Before connecting the sample to the spectrometer, the two possess different work functions. Upon electrical connection under ultra-high vacuum (UHV), electrons flow until the Fermi levels equalize and a uniform electrochemical potential is established so that the spectrometer's work function is used to compute the binding energy. So, the binding energy is measured with respect to the Fermi level.[19]

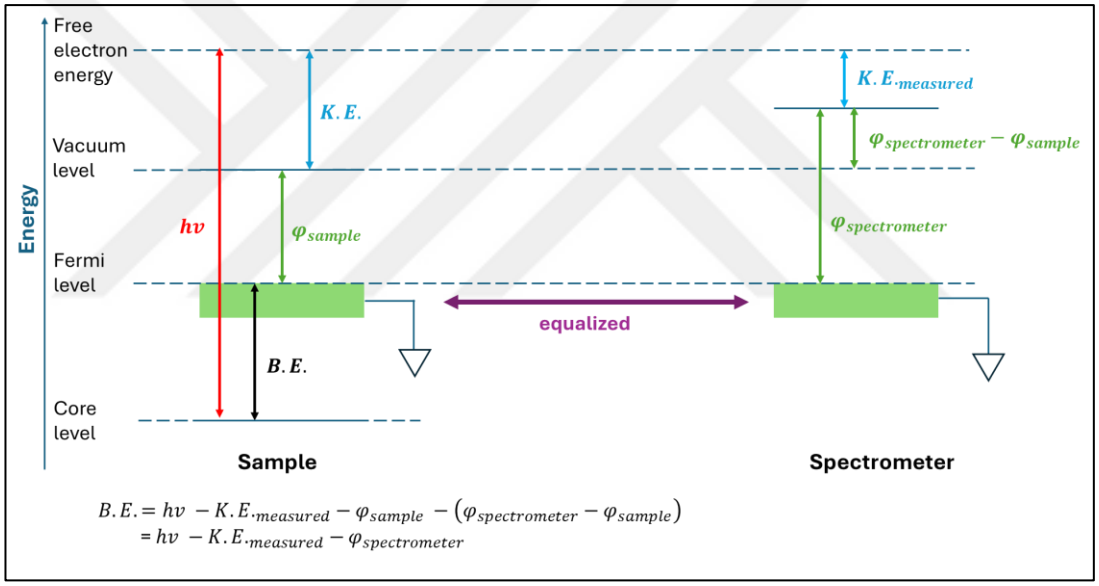

Figure 3. The energy level diagram showing that the Fermi levels of the sample and the spectrometer are aligned so that the work function of the spectrometer can be used to compute the binding energies from the measured kinetic energies.

A critical requirement for accurate XPS measurements is the UHV conditions, typically in the range of 10^{-7} to 10^{-10} mbar.[1] These low pressures are essential for ensuring that the emitted electrons from the sample can travel to the hemispherical kinetic energy analyzer without undergoing scattering by residual gas molecules. Such scattering would decrease the intensity and change the kinetic energy of the electrons,

compromising the accuracy of the binding energy calculation. Moreover, UHV conditions help preserve surface cleanliness by minimizing contamination, which is particularly important for studying sensitive or reactive surfaces.

Due to its high energy resolution, surface specificity, and chemical sensitivity, XPS has become an essential tool for analysis of surface chemistry. Compared to other techniques such as Auger Electron Spectroscopy (AES) and Secondary Ion Mass Spectrometry (SIMS), XPS offers a non-destructive, quantitative analysis of the outermost atomic layers with higher chemical state resolution.[20,21] Its surface sensitivity and elemental specificity make it very important in surface science, especially when complemented by other in-situ techniques.

1.1.2 Common Applications of XPS

Traditionally, XPS has been used to analyze elemental compositions, detect chemical shifts and map oxidation states at surfaces. It is widely used in materials science, chemistry, nanotechnology, and device engineering.

In more recent years, XPS has become valuable for applications involving nanoscale systems, thin films and advanced functional materials. In catalysis research, XPS enables investigation of oxidation state distributions across catalyst surfaces, providing insight into active site speciation, catalyst aging, and regeneration mechanisms.[22–26] For example, changes in the ratio of metal-to-metal oxide under reducing or oxidizing conditions can be monitored in situ, revealing how surface composition evolves during catalytic cycles.[27,28]

In study of polymers and soft matter, XPS is commonly used to evaluate the presence of specific functional groups and monitor degradation or crosslinking over time, often in tandem with complementary spectroscopies or microscopy methods. [29–33]

In semiconductor device fabrication, where surface cleanliness and chemical uniformity are paramount requirements, XPS is used not only to identify unwanted contaminants such as carbon or fluorine[34] but also to map dopant distributions and evaluate thin dielectric layers like Al_2O_3 or HfO_2.[35,36] Its nanometer surface sensitivity is crucial in resolving interfacial layers that influence device performance and reliability.

XPS has also proven to be a crucial instrument in the development of advanced coatings,[37] such as self-assembled monolayers (SAMs),[38] passivation layers,[39] and corrosion-resistant films.[40] It allows researchers to confirm molecular orientation, packing density, and chemical termination at the outermost surface, which are all critical parameters for tailoring adhesion, wettability, or biocompatibility.

Moreover, XPS is increasingly applied in the context of two-dimensional (2D) materials such as graphene,[41,42] MoS_2,[43] and transition metal dichalcogenides.[44] In these systems, understanding defect chemistry, doping effects, and interlayer charge transfer is essential, and XPS can offer direct chemical insight into these nanoscale processes.

Recent advances such as ambient pressure XPS (AP-XPS) and liquid-compatible XPS setups have also extended the number of fields that can employ this technique, including the investigation of biological samples and their interfaces.[13,45,46]

With the growing demand for high-resolution, spatially specific characterization, the technique is increasingly applied to heterogeneous interfaces such as those found in batteries, capacitors, and fuel cells.[47,48]

1.1.3 Local Potential Developments under DC/AC Bias

A less conventional, yet powerful, use of XPS involves tracking electrical potential variations across a device or material. With the rising number of studies on energy storage and conversion systems, *operando* and *quasi-operando* XPS techniques have gained traction as discussed in section 1.1.2. In battery and supercapacitor research, XPS is used to track the formation and evolution of the solid-electrolyte interphase (SEI),[49,50] a nanometer-thick layer that critically influences ion transport, stability, and capacity of the energy storage device.[51] In particular, battery research increasingly uses XPS depth profiling (via gentle-beam Ar^+ sputtering) to correlate SEI composition with cycling performance.[52–55] Through careful measurement under controlled bias and environmental conditions, researchers can observe charge redistribution, decomposition of electrolyte additives, and the migration of species during charge–discharge cycles.[56]

Under externally applied bias (DC or AC), the local potential landscape has an influence on the kinetic energy of photoemitted electrons, which manifests as binding energy shifts in the XPS spectrum.[57] Since XPS spectra are recorded with high energy precision (typically ~20 meV), these shifts can be used to extract information about electrical potential gradients at chemically distinct regions which can be used to infer the underlying electrostatic environment. Even mV scale deviations can be detected as asymmetric peak shape or peak broadening.

This phenomenon is illustrated in Figure 4, which shows the same energy diagram from Figure 3, now for a conductive sample under (DC) positive bias and zero bias.

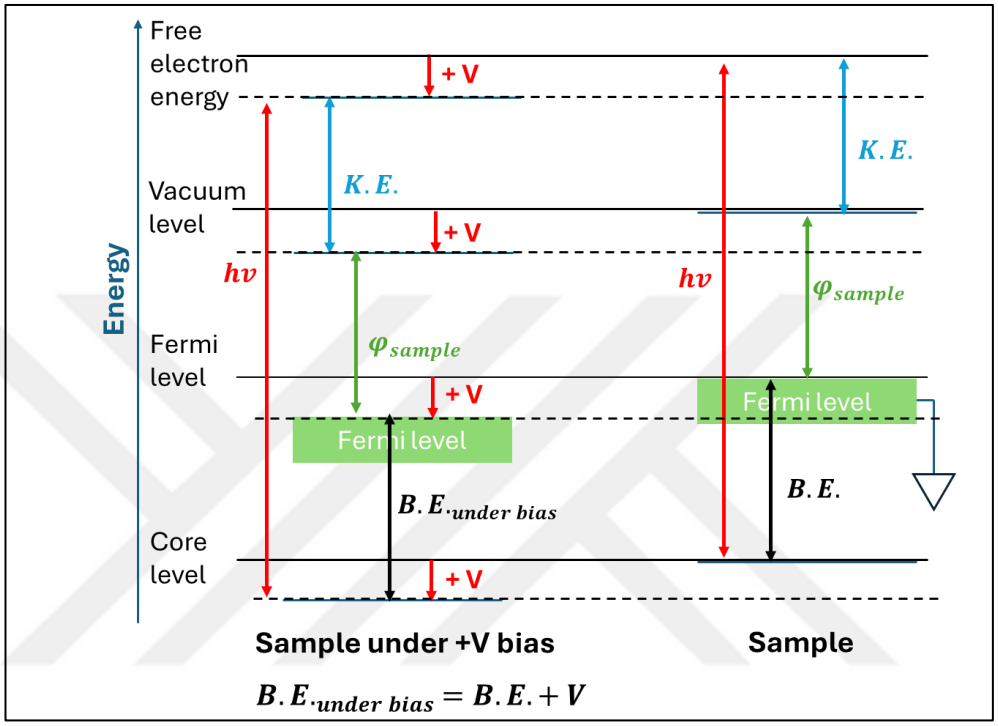

Figure 4. Energy level diagram showing that under positive bias, the measured binding energy is equal to the binding energy of the unbiased sample and the applied voltage.

When a positive bias is applied to a conductive sample such as platinum, the kinetic energies of all levels are shifted downward compared to the spectrometer which results in a corresponding upward shift in the binding energy of the emitted electrons. The opposite is true for negative bias. For a conductive sample, the shift in binding energy under DC voltage is equal to the magnitude of the applied voltage, (e.g., a +3 V bias will result in a 3.0 eV shift in binding energy) and resulting spectra for platinum (Pt4f) under ± 3 V DC bias are shown in Figure 5. Here, the magnitude of the binding energy shift is equal to the applied voltage, as described.

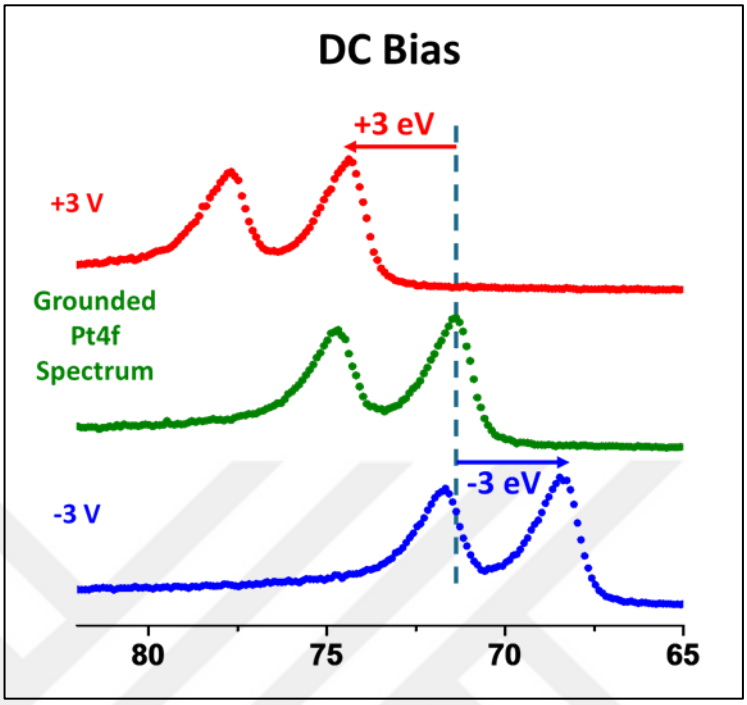

Figure 5. The XP spectrum of Pt4f at ground level (olive), under +3V(red) and under -3 V (blue) external DC bias.

However, for poorly conducting or insulating materials, the observed binding energy shifts are smaller than the magnitude of the applied voltage. This difference is primarily due to charging and limited electronic compensation, leading to additional surface charging caused by the photoemitted electrons.[58,59] Square-wave (SQW) as well as sinusoidal AC excitations can also be employed to probe time-dependent potentials; the practical implications and interpretations of SQW bias are detailed in section 1.4.

This capability allows XPS to function as a minimally invasive, chemically specific oscilloscope. Moreover, since photoelectron generation involves negligible current (on the order of nanoamperes), the IR drop due to measurement across the system is minimal and does not interfere with measurement for typically non-

conducting samples having active resistance values in MΩ range (10^{-9} nA x 10^{-6} Ω = 10^{-3} mV – which is below the detection limit) , allowing us to observe the natural behavior of the system under bias.

1.1.3.1 Operando-XPS

Operando-XPS refers to simultaneous acquisition of XPS spectra while imposing another active operation to the sample. In our case, an external electrical bias is applied to a working system while spectral data is recorded in real time and the current response is simultaneously measured. Unlike *ex-situ* XPS, *operando*-XPS can give a direct correlation between surface chemistry and device response under realistic electrochemical operating conditions. This enables direct observation of changes in chemical states (if any), ionic distributions, and electrical potential profile developments.

Recent implementations using coplanar capacitor geometries have expanded the applicability of *operando*-XPS to ionic liquids.[11,12,60,61] Such geometries provide a clear path for the XPS beam to probe the electrode and electrolyte surfaces. Key spectral features such as binding energy shifts, peak broadening, appearance or disappearance of chemical species from the spectra can be monitored with high lateral and temporal resolution, providing valuable insight into both electronic and ionic transport mechanisms. Moreover, *operando*-XPS is unique in its ability to extract chemically specific electrical potential maps across complex interfaces. By recording spectra at spatially distributed points across the device, the voltage drop and the electric field profiles can be reconstructed, giving electrostatic potential maps of the surface of the working electrochemical system.[62–65]

These developments have positioned *operando*-XPS as a unique diagnostic tool, capable of probing spatially and temporally resolved voltage maps, characterizing interfacial behavior, impacting on design of energy storage and iontronic devices and neuromorphic applications.[41,65–71] As it is a relatively non-invasive technique, it is also complementary to many traditional electrochemical methods such as cyclic voltammetry, chronoamperometry and electrochemical impedance spectroscopy, etc.[11,12]

1.1.3.2 Electrical Double Layer: Concept and Significance

The electrical double layer (EDL) is a fundamental concept in electrochemistry, and it plays a crucial role in capacitive energy storage, electrochemical sensing and ion transport at interfaces. It describes a structured charge distribution at the electrode-electrolyte interface that spontaneously forms due to the accumulation of oppositely charged ions. When external bias is applied to an electrode, ions in the electrolyte reorganize at or near the surface to screen or neutralize charge, resulting in a layered charge distribution.

The EDL is commonly modeled to be consisting of two regions, the Helmholtz layer and the diffuse double layer. Helmholtz layer is the compact inner layer containing adsorbed ions and the outer layer where ions are distributed according to electrostatic forces and thermal motion is the diffuse double layer. The structure and the dynamics of the EDL determine key electrical properties such as capacitance, ionic conductivity and kinetics. For systems containing ionic liquids, EDL is particularly important. As there is no solvent present in IL environments, highly concentrated and

structurally complex EDLs can form illustrating different behavior from that of a dilute aqueous solution.

So, understanding this complex interfacial structure is very important to optimize the performance of supercapacitors, batteries, iontronic systems as well as for probing fundamental electrochemical processes such as ion screening and charge transfer in the system. The significance of EDL is well-established; however, it is hard to directly probe it due to its dynamic and nano-scale nature of the involved processes.

XPS offers a unique advantage due to its intrinsic surface sensitivity in the nanoscale in investigating the outermost layer of EDL. By employing *operando*-XPS and applying DC or AC bias, the measured binding energy shifts can reflect the local electrostatic potential experienced by different ionic species on the surface enabling a chemically specific way to track the formation of EDL and its evolution.

1.2 Analyzing Liquid Surfaces with XPS

Despite its origins in solid-state analysis, XPS has been increasingly adapted to study liquid interfaces, particularly those involving ionic liquids (ILs) due to their negligible vapor pressure. Challenges in applying XPS to liquids include sample evaporation under high vacuum conditions and the instability of liquid films which make it hard to achieve reproducible surface positioning for analysis. Traditional solvents, e.g. aqueous or organic solvents, generally evaporate under UHV conditions, making them unstable for long-duration and/or high-resolution XPS studies.

The foundation for analyses of liquids by XPS was also pioneered by Kai Siegbahn's group. In late 1970s and the 1980s, they developed a technique which they called "liquid beam" with which they could stabilize the thin liquid layers against a

substrate.[72] They had shown that liquid samples can also be investigated as long as the evaporation was minimized. However, this technique still required specially adapted vacuum chambers, difficult to incorporate to commercial instruments.

Later, this approach evolved into what is called “liquid jet” technique in which a narrow, high-velocity stream of liquid is injected into the vacuum, allowing photoelectrons to escape before the liquid evaporates.[73] This was also highly technical and could not be adapted to all XPS systems. However, this was a significant step in the development of XPS for studying aqueous chemistry, solvated ions and liquid interfaces. While these methods were groundbreaking, they required specialized instrumentation and vacuum adaptation strategies.[72,73]

However, ionic liquids (ILs) offer a more straightforward path for liquid analysis in conventional UHV-based XPS setups. Thanks to their negligible vapor pressure and high thermal and chemical stability, -even under X-rays, they do not evaporate or degrade under typical UHV conditions. Unlike traditional solvents, they eliminate the need for continuous liquid flow, high pressure compensation etc., simplifying the experimental design. Their properties and applications are further discussed in Section 1.3.

For systems that cannot be stabilized under UHV conditions even with specialized equipment, such as water, alcohols and biological fluids with high volatility, ambient pressure XPS (AP-XPS) offers an alternative solution. An extensive differential pumping system allows the sample to stay in ambient conditions and for the photoelectrons to travel in high vacuum. This technique has proved to be useful in

catalysis, corrosion and electrochemical research in particular since it is highly important to maintain the native environment.[74,75]

While AP-XPS offers this alternative solution, the use of ILs in conventional UHV remains an advantage for long-term and high-resolution *operando* experiments. Especially in electrochemical systems involving ILs, XPS offers direct insight into the surface potential and interfacial charge distribution, especially when studied under bias. A critical advancement is the use of inclined substrates or confined geometries (e.g., porous membranes or coplanar configurations) to position ILs such that their surface can be reliably probed by the X-ray beam.[76,77] This allows for tracking EDL formation and screening behavior through the binding energy shifts of constituent ions that may be present in the IL.

With careful experimental design, XPS can also provide both chemical and electrical insight into liquid/solid interfaces, offering a valuable complement to electrochemical and spectroscopic tools. XPS stands out as one of the few techniques that can provide depth-resolved, high resolution, quantitative chemical analysis of liquids and their interfaces under operando conditions.

1.3 Ionic Liquids: Structure, Properties and Applications

Ionic liquids (ILs) are salts composed entirely of ions that remain in liquid form at or near room temperature.[78] They typically consist of large, asymmetrical cations such as imidazolium, pyridinium, pyrrolidinium paired with anions like tetrafluoroborate (BF_4^-), hexafluorophosphate (PF_6^-) or amino acid species. Due to their steric hindrance, ion pairing in these systems is weak, resulting in disordered, fluid-like behavior at ambient temperature.[79] Also, their melting points are typically

below 100°C, which grants them their "ionic liquid" identity. In Figure 6, some common cations and anions that make up ionic liquids are shown.

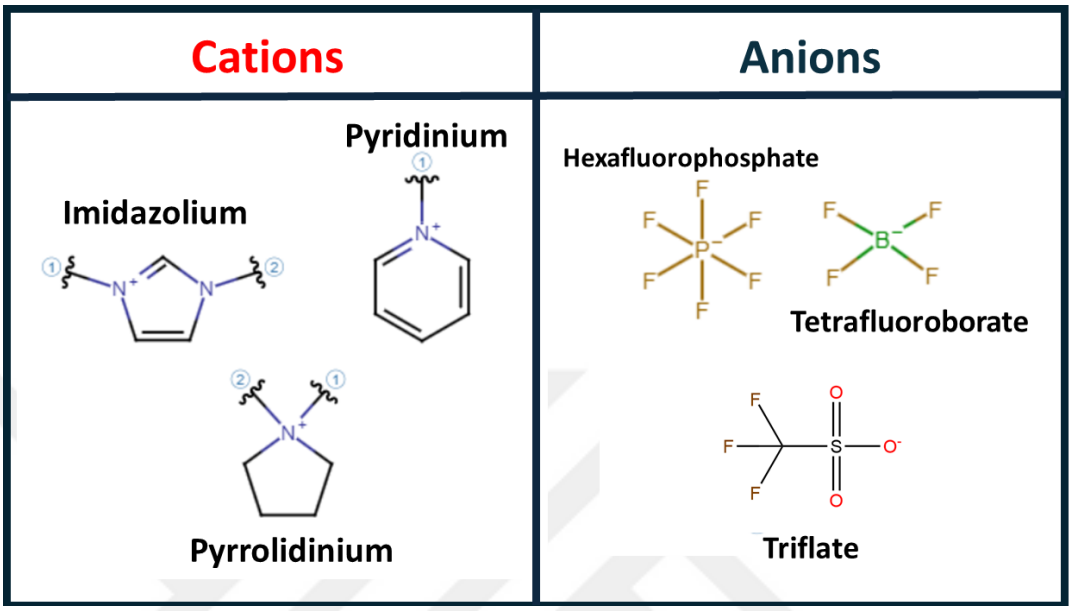

Figure 6. Some common cations and anions that are used by IL manufacturers.

Ionic liquids have exceptional physical and chemical properties compared to traditional solvents:

- A wide electrochemical stability window (often > 4 V), allowing them to operate under applied bias even under significant voltages without undergoing decomposition;[80,81]
- Negligible vapor pressure, making them non-volatile and well-suited for vacuum environments such as for use in XPS;[78,82]
- High ionic conductivity (~ 0.1 to 1 S/m);[83]
- Chemical and thermal stability, even when exposed to high energy X-rays; as a result, samples prepared with ionic liquids can remain intact and stable for extended periods of time (in the order of weeks);[79,84]

- Non-flammable and non-toxic compared to traditional solvents, supporting their use in green chemistry and biomedical applications;[85–89]
- Tunability through ion selection, allowing scientists to tailor ILs to fit their necessities ("designer solvents").[90,91]

Despite their many advantages, challenges about the ILs still remain, including high viscosity and relatively low ion mobility consequently.[92] Strategies to mitigate these include modifying the ion structures, creating mixtures with organic solvents or using IL mixtures, particularly those with differing anion/cation sizes to tailor ionic dynamics and interfacial properties.[93–96]

IL mixtures are prepared by combining two or more ILs often with different anion and cation sizes, to produce a medium that is altered to have improved transport and structural properties. Researchers can tailor physicochemical properties such as viscosity, conductivity and electrochemical windows and also manipulate interactions by tuning the size and structure of the constituent ions. These mixtures maintain the thermal and chemical stability of ILs while also benefiting from enhanced ion mobility due to lower viscosity.[95,97–100]

IL mixtures are of interest to scientists for two main reasons. The first one is obvious as they provide a workable solution to device performance constraints in electrochemical systems. Another reason is that they provide a platform for investigating ion-ion interactions, molecular packing and dynamic screening under applied bias, indispensable in electronic corrosion and/or tribological applications.[11,12,64,101–108]

Several studies have been made to demonstrate the benefits of this strategy. IL mixtures have been employed to adjust the interfacial capacitance, improve low-temperature performance, and modulate the electric double layer (EDL) structure for enhanced energy storage systems.[109,110]

Combined XPS studies have shown that mixing ILs can change the surface composition and ion orientation at different interfaces, even in the absence of external bias.[111,112] For example, it has been demonstrated that mixing pyrrolidinium and imidazolium based ILs can alter the abundance of cations, revealing preferential orientation effect at the interface, depending on the ion sizes and functional groups involved.[113] Similarly, angle-resolved XPS (AR-XPS) has been employed to probe depth-dependent segregation in IL mixtures to provide information about how specific ions enrich the surface layer.[114,115]

These findings show that IL mixtures can be valuable as model systems, for decoupling complex electrochemical phenomena. By varying the composition and structure of ions, the bulk transport properties and interfacial arrangements can be investigated and how they affect potential distribution and capacitive performance under external bias can be explored.[116,117]

In the specific concept of XPS, IL mixtures offer us a platform for probing how modified structures can affect charge accumulation, screening and voltage distribution on the surface.[118,119]

A representative XPS survey spectrum of DEME-TFSI, the pure IL used in this study is shown in Figure 7(a) and the structures of the DEME cation and TFSI anion are illustrated in Figure 7(b) and Figure 7(c). Comparative survey spectrum from the

1:1 (v/v) DEME-TFSI: DEME-BF_4 mixture is also presented in Figure 7(d) with the structure of BF_4 anion shown in Figure 7(c).

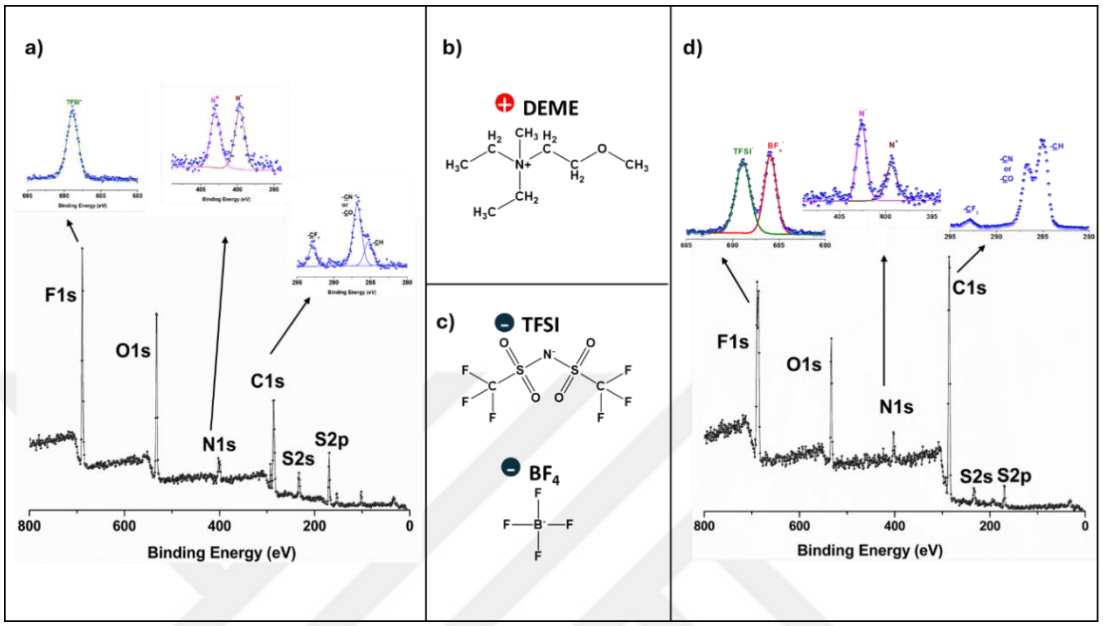

Figure 7. (a) XPS Survey Spectrum of the IL, DEME-TFSI. (b) Structure of DEME cation. (c) Structures of TFSI and BF_4 anions. (d) XPS Survey Spectrum of IL mixture, 1:1 (v/v) DEME-TFSI: DEME- BF_4.

1.4 Frequency-Modulation Techniques in Electrochemical Probing

Electrochemical processes in ionic liquids span a wide range of time scales, from sub-microsecond polarization to much slower ionic migration that occurs on the order of seconds.[108,120] Disentangling these phenomena is crucial for understanding electrochemical device performance. Frequency-modulated techniques provide us with the means to selectively probe processes according to their inherent time constants. Among these, the application of AC bias — especially square-wave (SQW) signals — enables to distinguish between fast and slow components.

1.4.1 Square-Wave and Other AC Modulations

AC excitation can also be employed in operando-XPS, and the dynamic voltage-induced responses can be recorded in temporally and spatially resolved fashions. Under AC bias, the potential alternates periodically between two voltage levels at a defined frequency. A square-wave (SQW) voltage signal, compared to sinusoidal waveform (SIN), induces sharp transitions between its maximum and minimum values, spending equal time at each level within a cycle. This kind of binary switching is well-suited for resolving the dynamic voltage response, as each state is well-defined and sustained. In other words, it imposes clear and instantaneous polarity reversals

In the context of XPS measurements, when a SQW AC bias is applied at a relatively high frequency - such as 10 kHz - each individual XP spectrum acquisition, which takes on the order of seconds, during thousands of full bias cycles, are collected and stored. The resulting spectrum is a time-averaged response of both positive and negative voltage states.

This temporal overlap is seen as two distinct peaks in the XPS spectrum which are referred as “twin peaks”, each peak corresponding to the potential-induced shifts of the photoelectron binding energy under the positive or negative bias states. The separation between these peaks is a direct measure of the full voltage applied to the system. For example, a ±3 V bias results in a 6.0 eV peak separation in the F1s peak of the IL, DEME-TFSI that is spread on a Pt-Pt coplanar capacitor device, as shown in Figure 8.

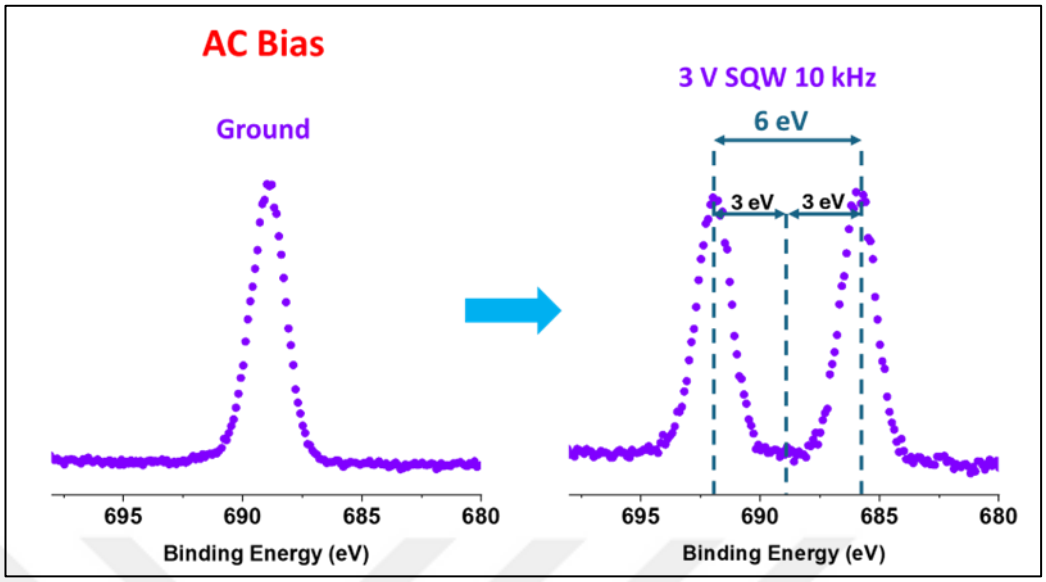

Figure 8. XPS Spectrum of the F1s region of a IL coplanar device under 3 V SQW 10 kHz; the grounded spectrum splits into two and the characteristic "twin peak" structure is seen, where the separation between the peaks reflect the full bias voltage applied.

This enables a straightforward mapping of the dynamic potential extremes across the device. Even in regions of the sample surface where the electric field has uneven distribution, due to factors such as but not limited to material conductivity, interfacial properties and/or geometry, the twinned peak separation still serves as a reliable indicator of the maximum voltage that is experienced locally.

Beyond the peak separation, the frequency of the SQW bias fundamentally determines whether ions can move and respond to the alternating field for an electrochemical device. At low frequencies such as 0.1 Hz, the system has ample time within each voltage period to reach a different state during the XPS scan, capturing the influence of ionic migration and charge screening effect. In contrast, at a higher frequency such as 10 kHz, the ions cannot respond quickly enough and remain essentially "frozen" in place, leaving only electronic polarization effects to be detected. This frequency-dependent response provides a chemically specific window

into how electrochemical systems containing ionic liquids and their mixtures behave under dynamic fields, a capability that is not accessible by traditional impedance measurements.

Figure 9 captures this frequency dependent behavior. Figure 9(a) shows the F1s XPS spectrum of the same electrochemical device, recorded at 3 V SQW bias at 10 kHz (collected at point 1 specified in Figure 12), while Figure 9(b) presents the corresponding spectrum at 0.1 Hz. Additionally, the figure includes a schematic that compares the time spent at each voltage for the two frequencies, highlighting on the ionic rearrangement at 0.1 Hz. This visual comparison offers a clear view of how frequency fundamentally alters the dynamic response of the system.

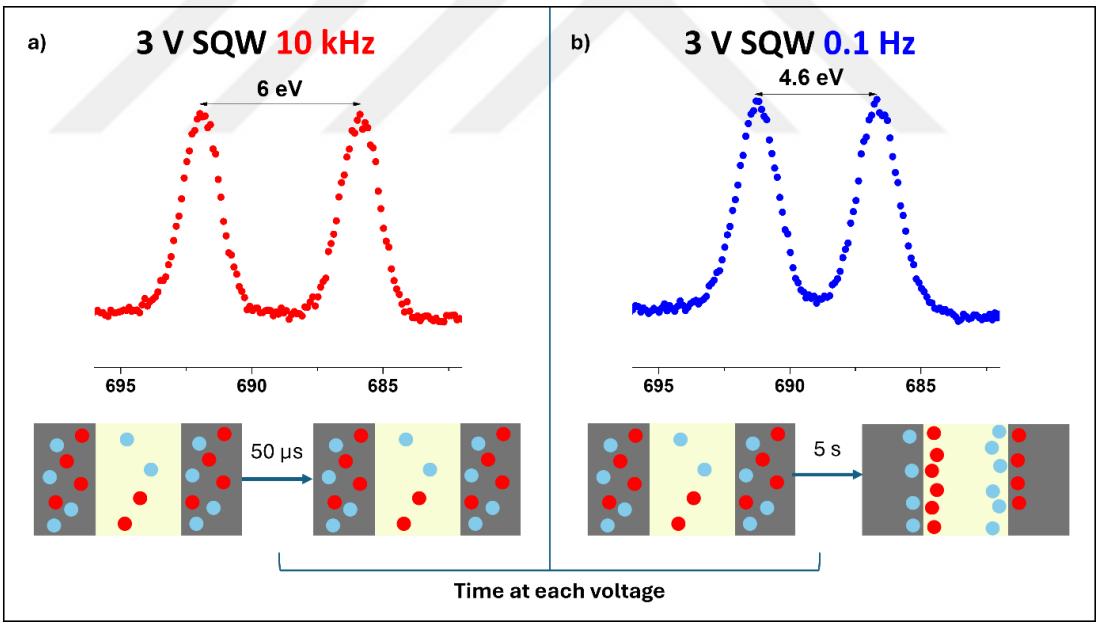

Figure 9. Comparison of XPS spectra of a IL coplanar device under 3 V SQW AC bias at (a) 10 kHz and (b) 0.1 Hz. The accompanying schematic highlights the time spent at each voltage level for these frequencies—while illustrating how at 10 kHz, the ions remain effectively immobile while the longer duration at 0.1 Hz allows ionic rearrangement on the surface.

1.5 Aim of the Study

The aim of this study is to employ X-ray Photoelectron Spectroscopy (XPS), particularly under *operando* conditions, to probe local electrical potential distributions and interfacial charge dynamics in electrochemical devices containing ionic liquids (ILs). This work focuses on advancing the utility of XPS beyond traditional chemical and electrochemical analysis by leveraging its sensitivity to binding energy shifts caused by electrostatic potential variations under externally applied DC and AC biases.

Two complementary device architectures are utilized to achieve this objective: (i) platinum–platinum (Pt–Pt) coplanar capacitors, which are well-suited for investigating frequency-dependent charge screening, potential drop across the IL layer, and circuit modeling under square-wave excitation; and (ii) multilayer graphene–multilayer graphene (MLG–MLG) devices, which are employed to explore electrosorption dynamics, open-circuit potential (OCP) effects, and residual charge behavior after shorting. The combination of these systems enables a detailed investigation of both steady-state and transient electrochemical responses.

A key component of this study is the design and testing of ionic liquid mixtures with distinct anion and cation sizes—specifically, DEME-TFSI and DEME-BF_4—selected to reveal how anion size disparity influences charge distribution, screening behavior, and overall impedance within the IL film. These insights are extracted through spatially resolved binding energy shifts, interpreted with the aid of equivalent circuit simulations using tools such as LT-Spice and Python.

Ultimately, this work aims to establish *operando*-XPS as a reliable, non-invasive method for studying the electrical behavior of complex electrochemical

systems. The findings are intended to impact on the design of more efficient ionic liquid formulations and device configurations for applications in energy storage, iontronics, and electrochemical sensing systems.

Chapter 2

2. Experimental Methodology

2.1 Materials

All chemicals and components used in this study were of analytical and/or electrochemical grade and were used after heating, in vacuum, to 80°C to get rid of the residual water as it has an influence on the measured binding energy shifts. [121]

The electrochemistry-grade ionic liquid *N,N*-Diethyl-*N*-methyl-*N*-(2-methoxyethyl) ammonium bis (trifluoromethanesulfonyl) imide (DEME-TFSI) was purchased from Sigma Aldrich (CAS Number: 464927-84-2) and used without further purification. DEME-TFSI was chosen due to its relatively large electrochemical window and strong F1s signal in XPS (6 F atoms/anion) for better data processing.

For ionic liquid mixture experiments, the ionic liquid, *N,N*-Diethyl-*N*-methyl-*N*-(2-methoxyethyl) ammonium tetrafluoroborate (DEME-BF_4) was obtained from abcr GmbH (CAS Number: 464927-72-8) and it was used in a 1:1 volume ratio with DEME-TFSI. The mixture was prepared by combining 0.5 ml of the two ionic liquids and letting them mix in an ultrasonic bath for two hours while heating to 50°C. The formation of the mixture was confirmed both by XPS and ATR-IR measurements. Pure DEME-BF_4 did not spread well on the device membrane so it could not be used by itself.

2.2 Device Design

2.2.1 Coplanar Capacitor Geometry

All devices that are used in this study were prepared in a coplanar capacitor geometry. In this configuration, two parallel electrodes are connected via a porous polyethylene membrane (PEM, from Gelon LIB), all positioned on the same plane and the ionic liquid is spread over the surface as the electrolyte. One of these electrodes is used as the source electrode and the other as the drain. This particular design allows for the application of in-plane electric fields across a 5 μL IL film that is dropped and spread over the whole surface. It is also a compatible design for studies with surface-sensitive XPS measurements due to the open planar structure.

2.2.2 Pt–Pt Devices

In the platinum-platinum (Pt–Pt) configuration, two platinum electrodes were deposited on top of a PEM substrate (from Gelon LIB), leaving a fixed 5 mm gap between them. A 5 μL droplet of the ionic liquid DEME-TFSI or ionic liquid mixture was soaked onto the membrane with a micropipette and allowed to distribute evenly on the surface to form a continuous electrolyte film bridging the electrodes. One of the Pt electrodes was used as the working electrode for external biasing (the source) and the other counter electrode was kept at ground potential (the drain). This geometry was specifically used for evaluating the frequency-dependent electrical response, local voltage drop, and charge screening behavior of the IL under externally applied AC/DC modulation. In Figure 10, a schematic representation of this Pt-Pt coplanar device is illustrated.

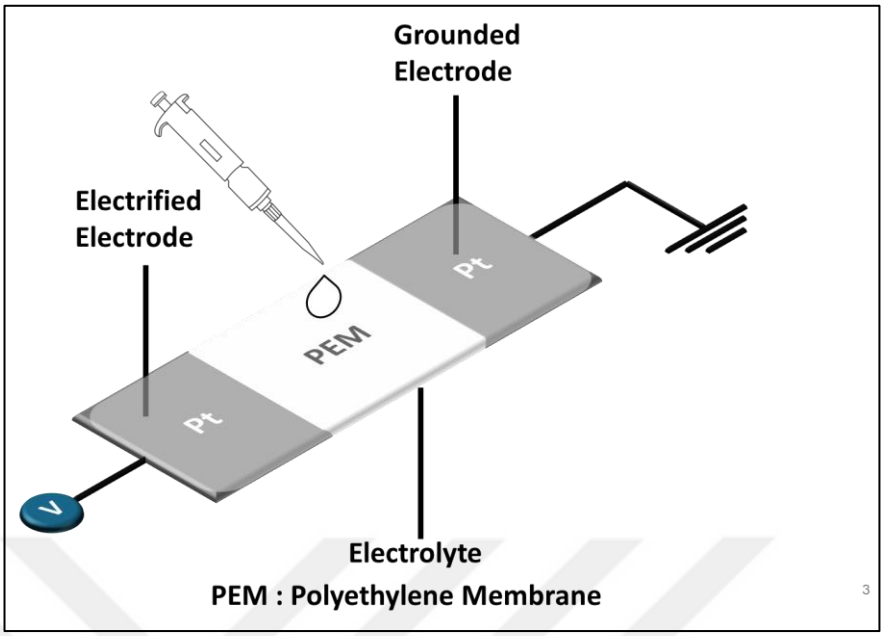

Figure 10. Schematic representation of the Pt-Pt IL coplanar device used in this study.

2.2.3 Multilayer Graphene–Multilayer Graphene Devices

2.2.3.1 Pure DEME-TFSI Device

Multilayer graphene (MLG) electrodes were prepared using chemical vapor deposition (CVD) on nickel foils (Alfa Aesar). The growth process employed a $CH_4/H_2/Ar$ gas mixture at temperatures ranging from 850–1000°C at ambient pressure, with flow rates of 300/100/100 sccm and a 5-minute growth time. The resulting MLG films consist of 300–600 graphene layers. The MLG sheets were transferred onto a PEM support. These MLG materials, along with the subsequent transfer of the sheet onto a PEM support, were prepared Kocabaş and his research group.[122]

For the coplanar structure, two pieces of MLG measuring 5 × 5 mm^2 were cut such that each piece had a 5 mm-long PEM extension from the edge of the MLG.

These pieces were placed on a glass substrate, aligned head-to-head with the PEM sections overlapping on top of each other. A droplet of the IL DEME-TFSI was introduced beneath the PEM such that the IL could permeate and uniformly wet the space between and beneath the electrodes. After placing the sample into the UHV environment, the whole system was heated up to 80°C overnight to remove any residual water. This assembly was designed for the investigation of ionic electrosorption, open-circuit potential and shorting effects. In Figure 11, a schematic representation of the MLG-MLG coplanar device.

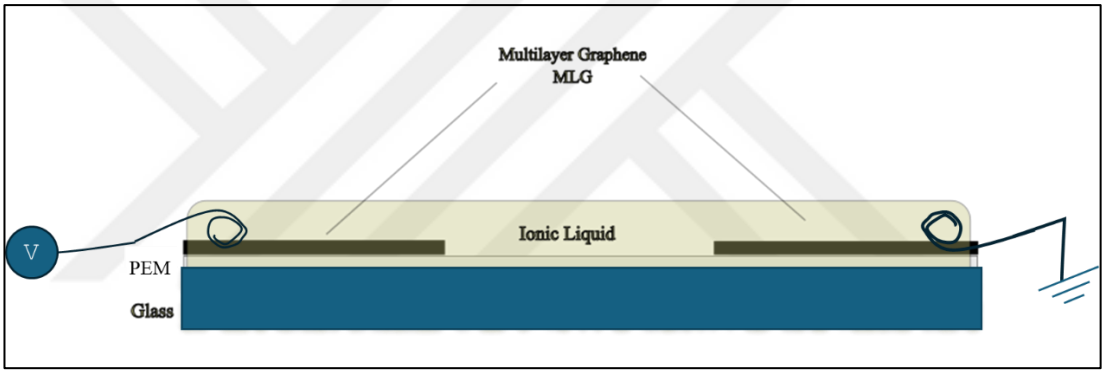

Figure 11. Schematic Representation of MLG-MLG IL coplanar device (side view).

2.2.3.2 10% Rb-TFSI – 90 % DEME-TFSI Device

To explore the effects of introducing a small alkali metal cation into the ionic liquid matrix, DEME-TFSI having ca. 10 % Rb-TFSI such that the electrolyte consists of one kind of anion and two kinds of cation were used in the same MLG-MLG coplanar capacitor configuration. The choice of rubidium as opposed to lithium as the cation was intentional as Rb has a larger photoemission cross-section compared to Li, meaning it has a more intense peak in XPS. [1]

2.3 Instrumentation

2.3.1 Characterization Techniques

2.3.1.1 X-Ray Photoelectron Spectroscopy

XPS measurements were conducted using a Thermo-Fisher K-Alpha X-ray Photoelectron Spectrometer equipped with a monochromatic Al Kα X-ray source (1486.6 eV). Survey spectra were collected at a pass energy of 200 eV, and high-resolution spectra of individual elemental regions such as F1s and $Sn3d_{5/2}$ were acquired at 50 eV pass energy.

To extract circuit parameters, two known resistors - (150 kΩ each) were soldered in series to the Pt-Pt coplanar capacitor, with the grounded electrode serving as a stable reference point. XPS measurements were acquired at designated locations, $Sn3d_{5/2}$ spectra were acquired at points a and b, corresponding to the soldering joints, while F1s spectra were collected at positions 1 through 5 along the coplanar device. Current measurements were acquired synchronously with XPS spectra. The spatial distribution of these points is illustrated in Figure 12.

For the MLG-MLG device with DEME-TFSI as the electrolyte, C1s and O1s were acquired in the same manner rather than F1s since O1s peak is inherently narrower and so, binding energy shifts are more prominent. For single point measurements, an X-ray spot size of 200 μm was used, while 100 μm was employed for line scan measurements. Snapshot mode was used in place of scanning mode for time-resolved XPS, enabling faster data collection (~0.5 s for each spectrum) and the

acquisition of ~7000 spectra in each one-hour cycle. This high temporal resolution provides detailed insight into the dynamics of charging and discharging processes at different voltages. The pass energy in this mode is set to 150 eV.

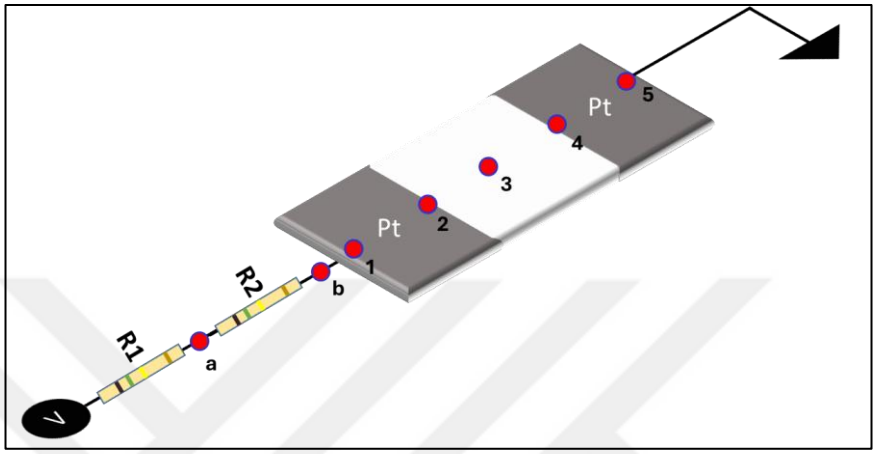

Figure 12. XPS data acquisition locations on the Pt-Pt device. Points are highlighted with red dots. **a** and **b** correspond to the soldering joints, while positions **1** through **5** indicate the sites where F1s spectra were collected.

Figure 13(a) shows the 2D map of these spectra at point 2 of the MLG-MLG device, capturing the shifts in the O1s region over 9000 iterations of data acquisition showing a compact view of the whole dataset. Figure 13(b) displays the corresponding 3D plot, highlighting the dynamic evolution of the peak intensity and position over the acquisition period based on the applied voltage.

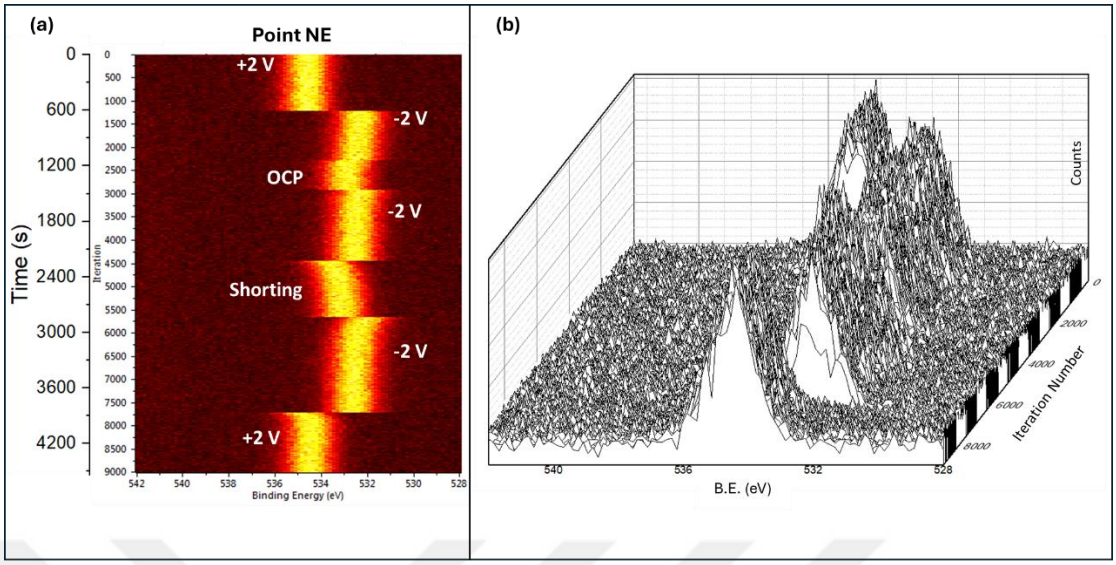

Figure 13. (a) Two-dimensional (2D) time-resolved color map showing the evolution of O1s core-level spectra over 9000 consecutive acquisitions with temporal resolution of 0.5 seconds collected at point NE. (b) Three-dimensional (3D) plot of the same dataset showing how the intensity and the position of the peak shift over the 9000 iterations.

For the MLG-MLG device with DEME-TFSI having ca. 10 % Rb-TFSI as the electrolyte, XPS measurements were performed in scan mode rather than snapshot mode to obtain more resolved and voltage-specific spectra. A pass energy of 50 eV was employed across all measurements. The following core-levels were monitored: C1s, F1s, N1s and Rb3d. Each scan has a dwell time of 50 ms. 10 scans were acquired for C1s, N1s and Rb3d whereas 4 scans were acquired for F1s due to its high signal intensity.

The voltage ramping protocol involved a stepwise increase in the applied DC voltage from 0 V to +3.0 V, at each step (0 V, +1.0 V, +2.0 V, +2.5 V, +3.0 V), 3 scans were taken. After reaching +3.0 V, the device was grounded, and 5 scans were taken at 0 V to track relaxation and rebound effects.

An identical protocol was followed for the negative cycle, applying stepwise voltages of 0 V, -1.0 V, -2.0 V, -2.5 V, -3.0 V and then returning to grounded state. All measurements were performed at point 2 and point 4 (as seen in Figure 12), also addressed as the point near electrified electrode (NE) and point near grounded electrode (NG) respectively.

The pressure in the analyzing chamber was maintained below 10^{-8} mbar during all measurements. After Shirley background extraction, spectral fitting was carried out using Thermo Avantage software that comes with the instrument, with a peak shape consisting of a 30% Gaussian and 70% Lorentzian product function.

The state of any of the three samples inside the instrument can be seen in Figure 14.

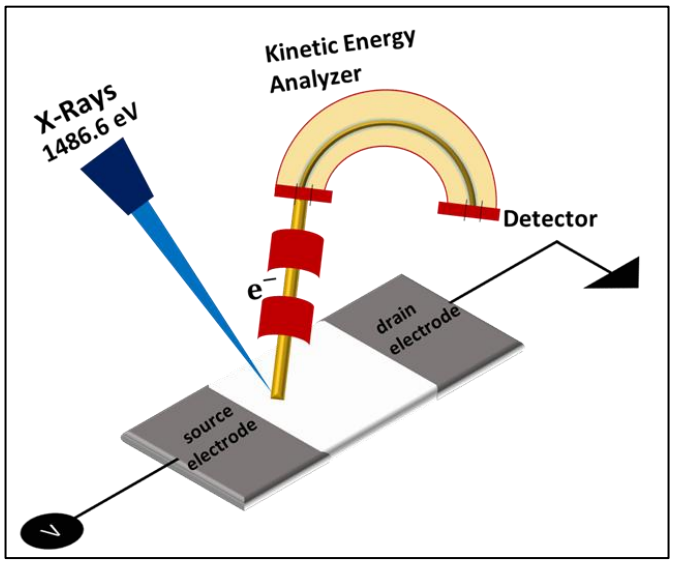

Figure 14. Schematic representation of the XPS measurement configuration, with the source and drain electrodes identified.

2.3.1.2 Electrical Biasing and Current Measurement Set-up

External DC bias was applied using a Keithley 2400 Source meter, controlled by a LabVIEW software developed in-house, for recording time-resolved current measurements. The current passing from the source electrode and the drain electrode was measured simultaneously with XPS data. For frequency dependent AC measurements, a Stanford Research Systems DS340 Function Generator was used. SQW modulation was chosen as described in section 1.4.

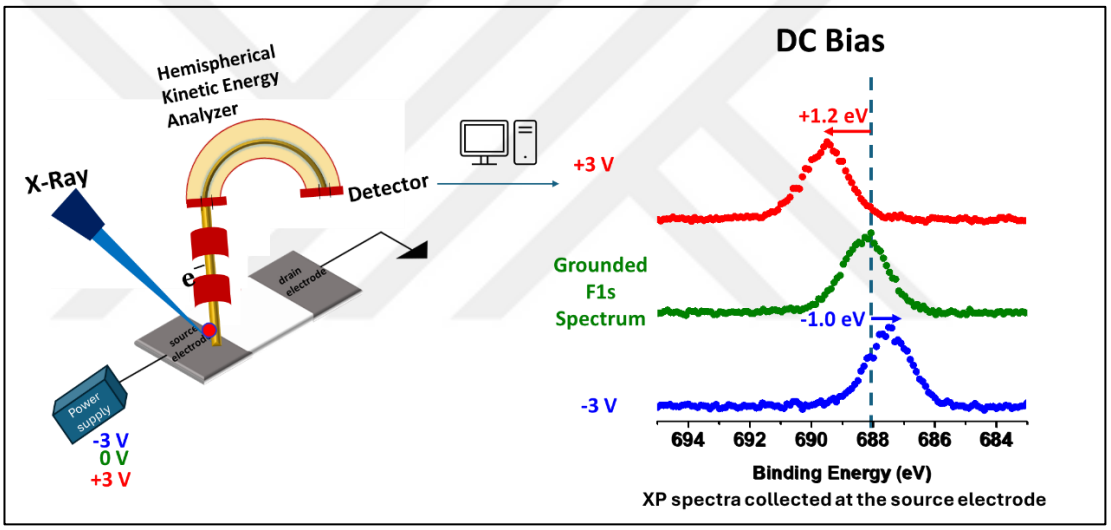

Figure 15. Schematic of coplanar Pt–Pt device under applied voltage to point 2. F 1s XPS spectra collected at the source electrode under +3 V, –3 V DC bias, and 0 V (no bias). Voltage-dependent response is highlighted.

2.3.1.3 Electrical Impedance Spectroscopy and Equivalent Circuit Modeling

Electrochemical impedance spectroscopy (EIS) data of the Pt-Pt device was obtained by using a Gamry Reference 3000 instrument in potentiostatic mode. DC voltage was set to 125 mV, and 50 mV sine-wave AC voltage was applied between 100 kHz and 0.1 Hz with 10 frequencies per decade. Cyclic voltammetry (CV)

measurements were also performed on the same device in the range of 0.125 V to 3.0 V under linear voltage ramp that is completed in 200 seconds to match the current-time measurements.

EIS data of the MLG-MLG device was collected with a Gamry Interface 1010E instrument in potentiostatic mode. DC voltage was set to 0 and 25 mV of AC voltage was applied between 10 kHz and 0.1 Hz with 10 frequencies per decade.

The impedance data was analyzed and fitted to equivalent electrical circuit models using the Gamry Echem Analyst 2 software.

LT-spice simulation program was employed to generate voltage output at different local positions along an equivalent circuit model at designated frequencies (10 kHz and 0.1 Hz). This output was then convoluted with the IL DEME-TFSI's F1s region's XP spectrum recorded under no bias to mimic the spectra obtained under AC modulations and compare them with XPS data. Initially, a preliminary model was proposed to reproduce the experimental data, which was subsequently refined to better portray the IL device.

Chapter 3

3. Results and Discussion – Pt–Pt Devices

3.1 Current Measurements

3.1.1 Current-Time Measurements

When voltage is applied to the source which we also call the electrified electrode, a potential difference between the two electrodes is created which allows for current to pass through the device to be measured. In Figure 16(a) the normalized current vs time measurements are presented. They are obtained under DC bias ranging from 0.125 V to 2.5 V. The same data is shown in Figure 16(b) in logarithmic scale for a duration of 300 seconds in the same voltage range. Analysis of these curves reveal that, at the very start, current is rapidly decreasing, a region that shows the fast, charging current decay.[123] After about 100 seconds, at all potential values, a steady state current is reached. The current increases with increasing potential values, as expected.

In an ideal capacitor, when voltage is applied and the resulting current is measured, the expectation would be that the current to decays exponentially over time, following the relation:[51]

$$I(t) = \frac{V_0}{R} e^{-t/RC}$$

where R is the resistance, C is the capacitance, V_0 is the initial voltage, t is elapsed time after voltage step and RC is τ, the time constant of the system.

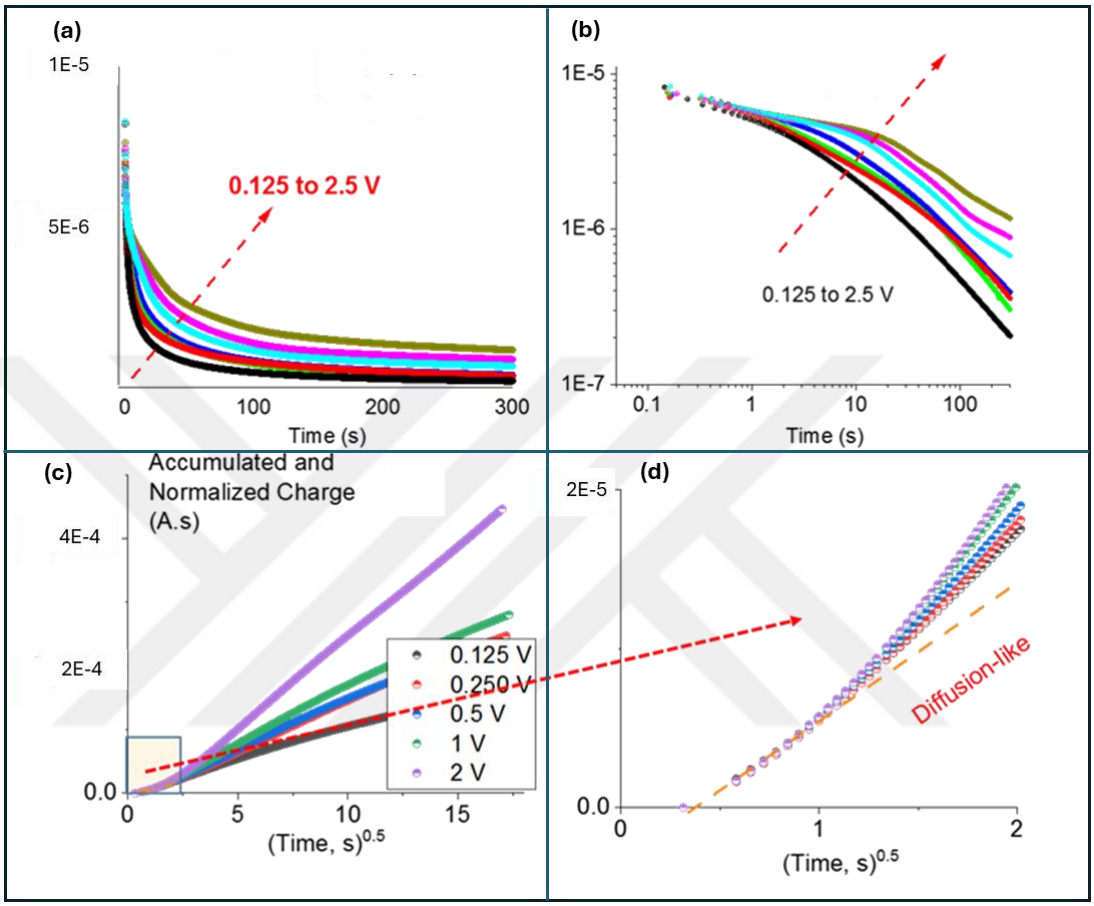

Figure 16. Current-time Measurements. (a) Normalized current vs. time from 0.125 V to 2.5 V, (b) Normalized current vs. time in log-log scale at the same voltage values, (c) Accumulated Charge vs square root of time at same voltage values, (d) Same plot as in 12(c) but zoom in on 0-2 s interval.

However, in Figure 16(b), a clean exponential decay is not observed as the slope of the log-log plot does not match an exponential shape due to the long "tail" of the decay curve. This indicates the presence of additional processes such as ionic migration, or Faradaic reaction that contribute to current response beyond purely capacitive charging.

To assess the diffusion properties of the system, in Figure 16(c), the accumulated charge was calculated from the integrals of normalized current-time curves for the various voltage values, and it was plotted with respect to the square root of time. According to the Cottrell equation, there is a $\frac{1}{\sqrt{t}}$ dependence of the transient current, which translates to a linear dependence of accumulated charge vs. $\sqrt{t}$ for diffusion-controlled processes.[51] This linear relation is evident in the 0-2 second interval, as illustrated in Figure 16(d). This confirms that in early stages (shorter time scales), the charge transport is dominated by diffusion-like behavior. However, there is a clear deviation from it in longer time scales.

3.1.2 Current-Voltage Measurements

The current-voltage behavior of the coplanar capacitor of Pt-Pt was investigated by performing cyclic-voltammetry measurements in the range of ±0.125 V to ±3.0 V. under a linear voltage ramp that is always completed in 200 seconds.

In Figure 17(a), the current-voltage behavior is summarized and Figure 17(b), the same graph is shown after normalization of measured current, obtained by dividing the current with the applied voltage, similar to those reported by Yin et al.[124] It can be gathered from this data that the electrochemical behavior of this system resembles that of a supercapacitor[125] but as confirmed by this technique as well, there are other electrochemical processes as well.

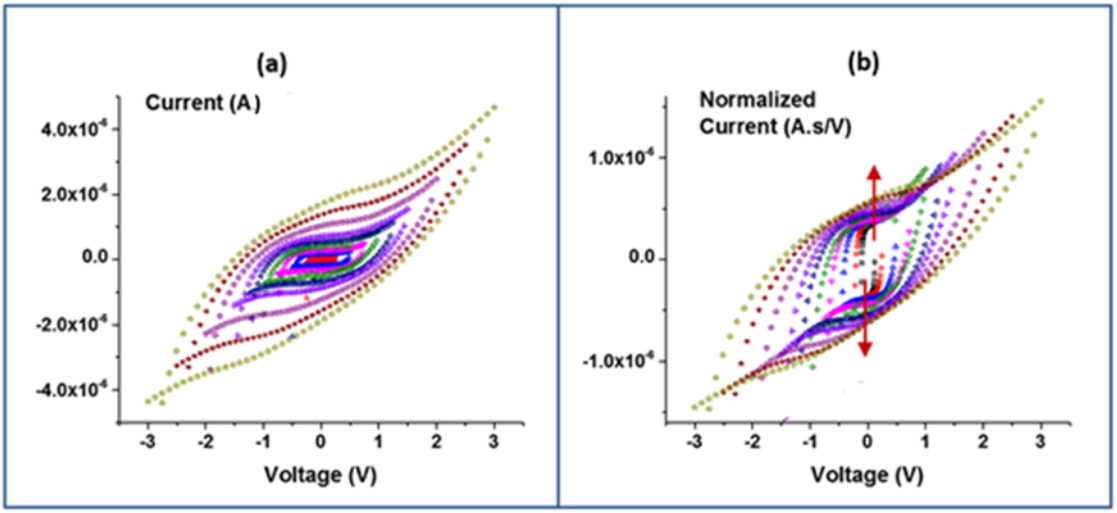

Figure 17. Cyclic voltammetry measured between ±0.125 V to ±3.0 V (a) Measured, (b) Normalized to 1 V. (Reprinted with permission from Karaoglu, G., Kutbay, E., Ince, S., Ulgut, B., and Suzer, S. Assessing Local Electrical Properties of Ionic Liquid/Metal Interfaces with Operando-XPS and by Incorporating Additional Circuit Elements. *Anal Chem* **2023**, *95* (40), 14861–14869. Copyright 2023, American Chemical Society.)

3.2 AC Biasing and Circuit Modelling

This section discusses the electrical potential developments, circuit behavior, and electrochemical dynamics of Pt–Pt coplanar capacitor devices under square-wave (AC) modulation. The electrical properties were probed locally by tracking binding energy shifts of the F1s and Sn3d (from the soldering points on the external resistance joints that are incorporated) signal using *operando*-XPS, complemented with electrochemical impedance spectroscopy (EIS) and circuit simulations.

3.2.1 High and Low Frequency AC Response

To differentiate between fast polarization and slow ionic migration in the IL, two square-wave frequencies were selected: 10 kHz and 0.1 Hz. The 10 kHz

modulation samples rapid dielectric responses in the system, such as the electronic polarization of the IL bulk, while the 0.1 Hz modulation captures slower processes involving ion migration and screening behavior at the interface as discussed in section 1.4.1.

XPS measurements of the F1s region in point 1 (as determined in Figure 12), in Figure 18(b), under 2.5 V SQW AC bias at 10 kHz reveal peak splitting, corresponding to ±2.5 eV shifts, faithfully representing the full bias window (5.0 eV total separation) that disappears completely at the grounded electrode. This behavior reflects the absence of effective screening at this timescale i.e. ionic motion is effectively frozen.

Line-scan XPS measurements across the device were also carried out, capturing the local potential variations at typically 70-100 discrete points along a single line across the coplanar capacitor device. Due to large number of data points, the spectrometer's snapshot data acquisition mode was employed. In Figure 18(b) and Figure 18(c), a set of these measurements is shown for a freshly prepared IL device that was subjected to outgassing and heating in vacuum to minimize contamination, at 10 kHz and 0.1 Hz 2.5 SQW AC is respectively.

In the 2D image of the line scan collected at 10 kHz, a V-shaped binding energy trend across the membrane to the grounded electrode is observed. This shows the steepest potential drop in the IL region between electrodes.

In contrast, at 0.1 Hz, a Y-shape is observed. At this frequency, ions have sufficient time to redistribute, leading to partial or complete screening of the applied

field not only in the bulk of the IL film but also within the regions near both electrodes. The separation between the twinned F1s peaks at the same point 1, is smaller than 5.0 eV, exactly 4.2 eV, indicating that the potential difference is reduced due to ionic relaxation. At point 4 (as determined in Figure 12), the binding energy difference between the twin peaks drop down to 1.3 eV which indicates that screening is observed not only between the two electrodes, but all over the coplanar device.

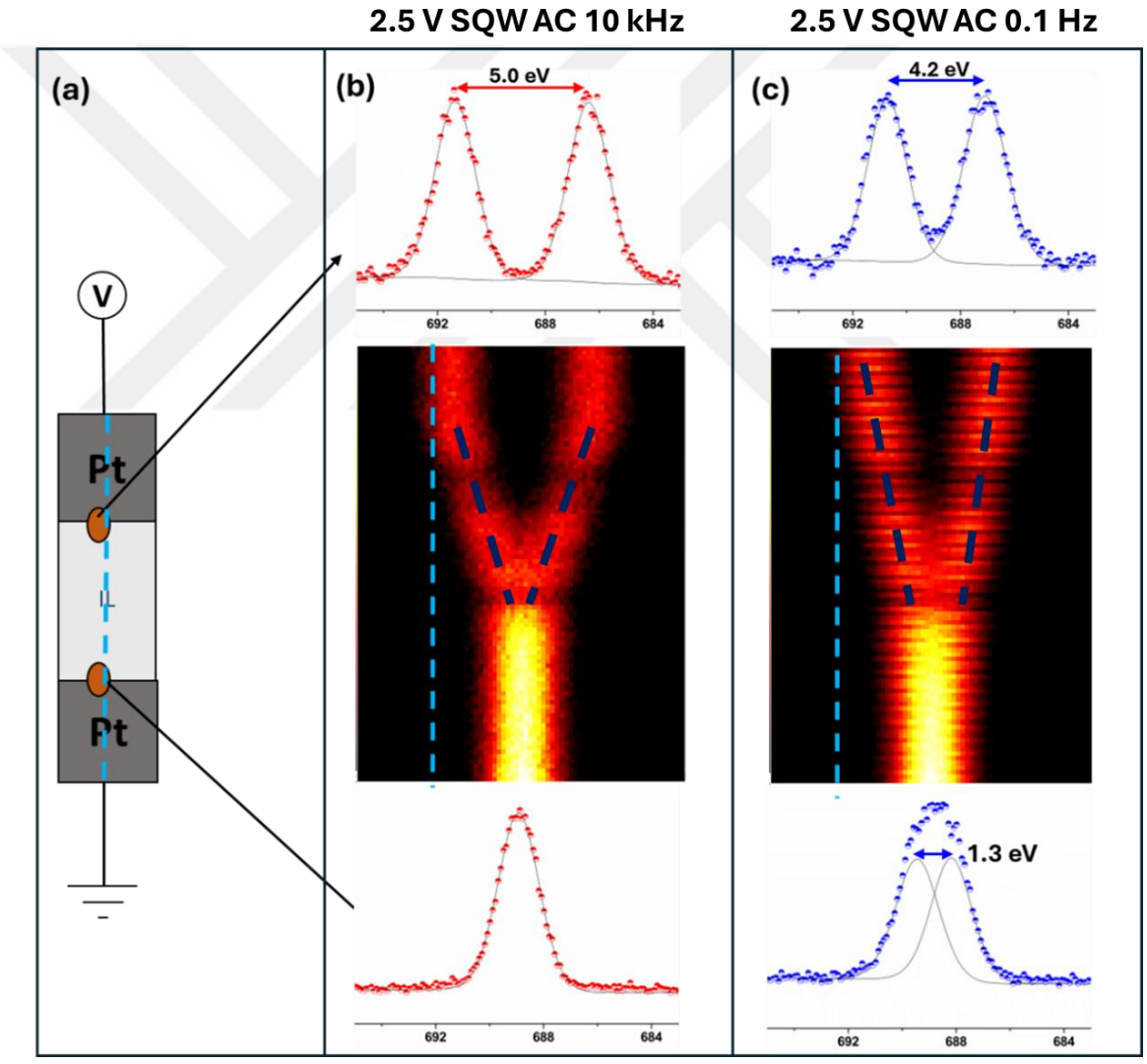

Figure 18. (a) Schematic of the ionic liquid (IL) device with local points near the electrified electrode (NE) and near the grounded electrode (NG) highlighted in orange. (b) Local XPS response at NE and NG under ±2.5 V square-wave (SQW) bias at 10 kHz, with the corresponding line scan profile shown in the center. (c) Local XPS response at NE and NG under ±2.5 V SQW bias at 0.1 Hz, with the corresponding line scan profile shown in the center. (Adapted with permission from Karaoglu, G., Kutbay,

E., Ince, S., Ulgut, B., and Suzer, S. Assessing Local Electrical Properties of Ionic Liquid/Metal Interfaces with Operando-XPS and by Incorporating Additional Circuit Elements. *Anal Chem* **2023**, *95* (40), 14861–14869. Copyright 2023, American Chemical Society.)

These spectral profiles help spatially map potential distributions and reveal that potential variation is strongest in the interelectrode IL region and less pronounced on the metal electrodes themselves, particularly at high frequency.

3.2.2 Incorporating Series-Resistors: Quantifying R & C

To gain quantitative insight into the impedance of the device, two 150 kΩ resistors were introduced in series with the Pt–Pt device and placed into the UHV chamber to perform similar line-scan and spectral mapping measurements. This modification enabled measurement of voltage drops across known resistances and provided an in-situ verification of the impedance behavior under operando conditions, bridging the gap between purely electrical measurements and chemically specific surface sensitive-characterization.

It is important to highlight that these series resistors were not merely passive components but actively improved the precision and reliability of the electrical potential quantification in the XPS measurements. Their introduction allowed for direct comparisons between the known voltage drops across the resistors and the local potential variations measured via the binding energy shifts in XPS, effectively transforming the experimental setup into a localized Wheatstone bridge configuration. As stated in the literature, this comparative measurement approach is invaluable because it enables more accurate identification of impedance and voltage developments that cannot be captured by conventional measurements alone.

To understand how these resistors influence the electrical response of the system, Sn3d peaks at the soldering joints were investigated. Under AC modulation, the observed binding energy differences between the twinned peaks directly reflect the local voltage drops. Specifically, as shown in Figure 19(b), under 2.5 V SQW 10 kHz modulation, the measured $Sn3d_{5/2}$ binding energy difference in position **a** decreased from 3.8 eV after the first resistor (R1) to 2.5 eV after the second resistor (R2) as measured in point **b**. This indicates two separate voltage drops for two resistors, 1.2 V across R1 and 1.3 V across R2, consistent with the resistor value of 150 kΩ. The remaining 2.5 V drop occurs across the IL device itself, allowing for a straightforward calculation of the AC current:

$$I_{Dev} = \frac{2.5\ V}{300\ k\Omega} \approx 8.3\ \mu A$$

This consequently suggests an AC impedance of roughly 300 kΩ (2 x 150 kΩ) for the IL device at 10 kHz SQW modulation, a value that is notably different from EIS measurements. However, it is important to note that as opposed to EIS measurements which employ sine-wave excitation, we employ 2.5 V SQW modulation in XPS, that may be where the difference in the values comes from.

A similar evaluation was done for 2.5 V SQW 0.1 Hz modulation at the same soldering points a and b in Figure 19(c). Now the binding energy difference decreased from 4.7 eV after the first resistor (R1) to 3.3 eV after the second resistor (R2). The voltage drop across the resistors at 0.1 Hz is smaller than the voltage drop at 10 kHz under the same voltage, indicating that the effective AC impedance had increased to:

$$\frac{3.3}{1.7} \times 300\ k\Omega \approx 580\ k\Omega$$

This again differs from the EIS measurements, and it can be associated with the large amplitude of 2.5 V SQW and different modes of excitation between the two techniques. The impedance values calculated in this manner for a device with 2 resistors at the front, for a device sandwiched between the two resistors and lastly for a device with two resistors placed at the end are tabulated in Table 1.

	10 kHz	**0.1 Hz**
2R + IL Device	300 kΩ	580 kΩ
R + IL Device + R	284 kΩ	572 kΩ
IL Device + 2R	315 kΩ	620 kΩ

Table 1. Impedance values estimated from Sn3d binding energy differences at soldering points a and b at different frequencies, 10 kHz and 0.1 Hz.

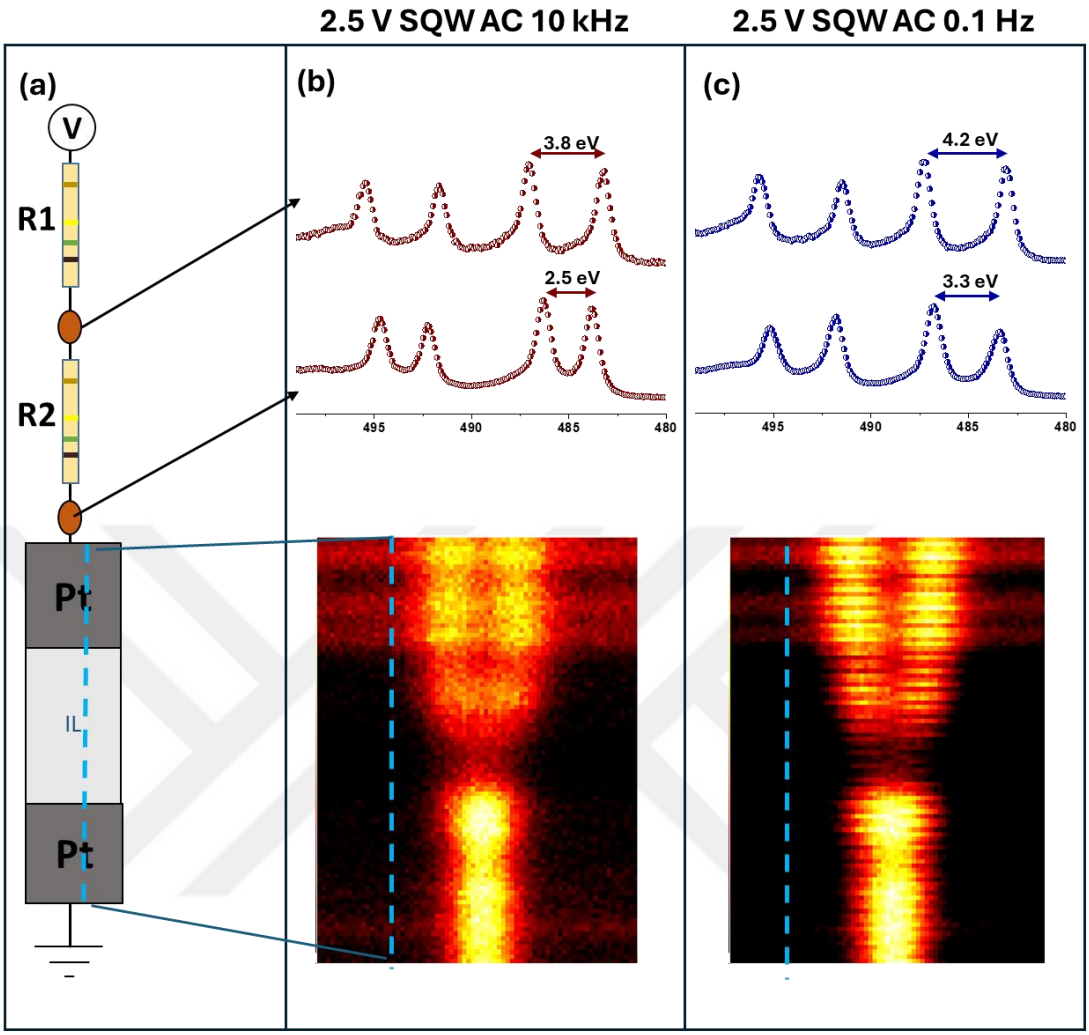

Figure 19. (a) Schematic of the ionic liquid (IL) device with 2 additional resistors of 150 kOhm resistance with local points near the electrified electrode (NE) and near the grounded electrode (NG) highlighted in orange. (b) Local XPS response at NE and NG under ±2.5 V square-wave (SQW) bias at 10 kHz, with the corresponding line scan profile shown in the center. (c) Local XPS response at NE and NG under ±2.5 V SQW bias at 0.1 Hz, with the corresponding line scan profile shown in the center. (Adapted with permission from Karaoglu, G., Kutbay, E., Ince, S., Ulgut, B., and Suzer, S. Assessing Local Electrical Properties of Ionic Liquid/Metal Interfaces with Operando-XPS and by Incorporating Additional Circuit Elements. *Anal Chem* **2023**, *95* (40), 14861–14869. Copyright 2023, American Chemical Society.)

Beyond providing quantitative information on AC resistance, these XPS measurements also reveal that the introduction of series resistors fundamentally alters the direction of the local AC electric field within the device. To see the effect of the

voltage on the position of the twin peaks more clearly, the voltage was increased to 3.0 V. Figure 20 illustrates this effect: in the pristine IL device in Figure 20(a), the F1s spectra taken at position 1 and position 2 of the electrified electrode under 3.0 V SQW bias display consistent shifts, with the binding energy difference between the twin peaks at 0.1 Hz consistently being less than that at 10 kHz. However, after adding the series resistors and applying 4 V SQW bias, shown in Figure 20(b), the direction of the binding energy shifts at position 1 reverses, illustrating a reversal in the local AC field direction. At 10 kHz, this reversal results from the resistors reducing the effective potential at the IL interface, while at low frequencies, 0.1 Hz, the ionic migration instead amplifies the imposed bias, causing ions to move in the opposite direction. The voltage was increased to 4.0 V to compensate for the voltage drop across the resistors.

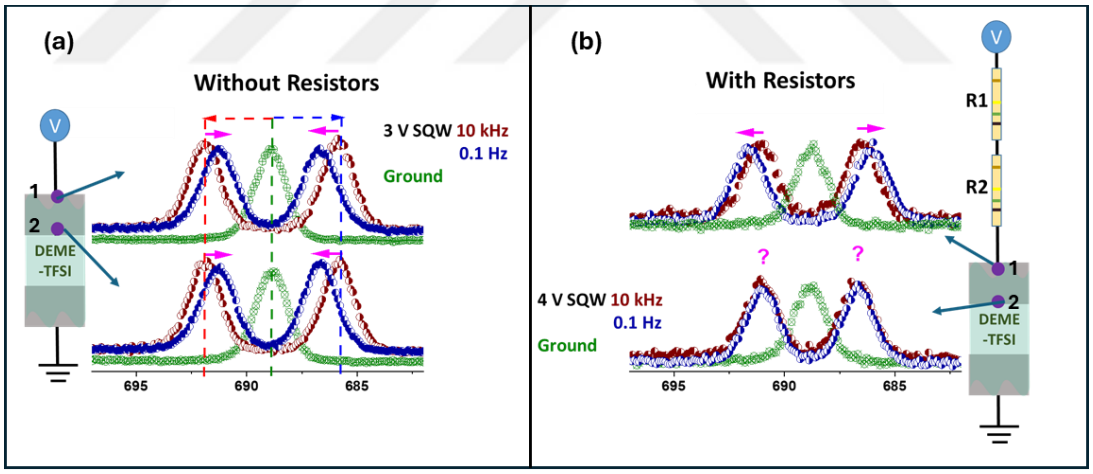

Figure 20. (a) F1s spectra of the IL device at points **1** and **2**, without series resistors. (b) F1s spectra of the IL device, with two 150 kΩ series resistors integrated, in points **1** and **2**. (Adapted from Kutbay, E., Ince, S. and Suzer, S. AC-Modulated XPS Enables to Externally Control the Electrical Field Distributions on Metal Electrode/Ionic Liquid Devices. Journal of Physical Chemistry B 2024, 128 (17), 4139–4147. Copyright 2024, American Chemical Society.)

When one of the resistors was soldered in series to the end of the IL device and one was left soldered before the device, as shown in Figure 21(a), it was confirmed that different resistor configurations can create nuanced and spatially distinct electric field distributions, including regions of neutral electric field in Figure 21(b).

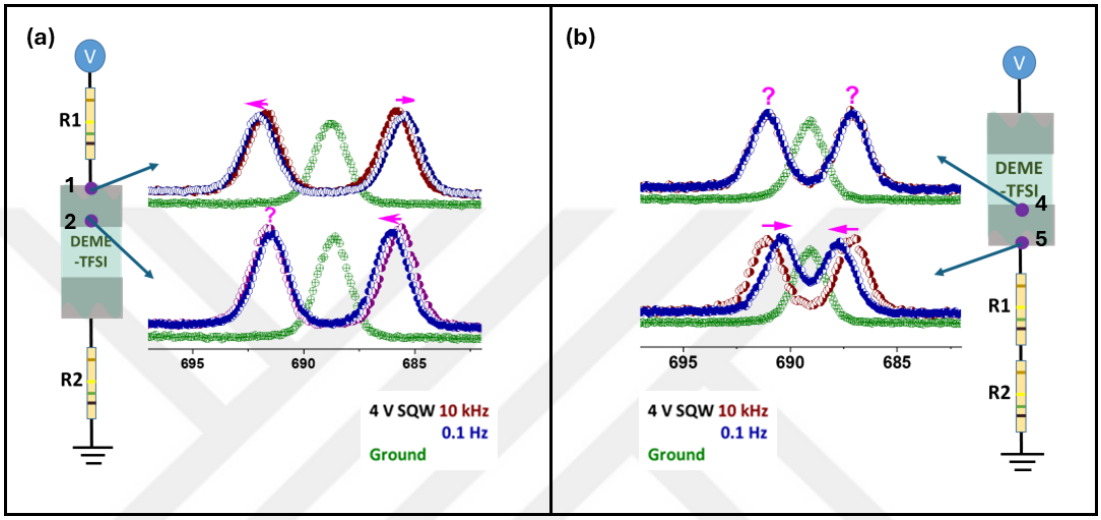

Figure 21. (a) F1s spectra of the IL device at points **1** and **2**, with one resistor placed before and one resistor placed after the IL device. (b) F1s spectra of the IL device, with two 150 kΩ series resistors placed after the IL device, collected in points **1** and **2**. (Adapted from Kutbay, E., Ince, S. and Suzer, S. AC-Modulated XPS Enables to Externally Control the Electrical Field Distributions on Metal Electrode/Ionic Liquid Devices. Journal of Physical Chemistry B 2024, 128 (17), 4139–4147. Copyright 2024, American Chemical Society.)

These findings collectively highlight that the placement of external resistors is not a passive addition for impedance quantification but also a powerful tool to actively tune and manipulate the local AC electric field distribution across the device, offering a unique experimental handle for probing and understanding dynamic processes in IL devices under operando conditions.

Given these results, a natural question arises: can a simple equivalent model capture the variable nature of the device impedance in a manner that reproduces the

XPS spectral features observed in the experiment? This question forms the foundation of the modelling efforts that aim to connect the measured binding energy shifts directly to the dynamic voltage distribution across the device.

It is also important to point out that when the resistors were introduced through the power supply's BNC connector instead of soldered and placed in the vacuum chamber, reliable XPS data under AC modulation could not be obtained as illustrated in Figure 22.

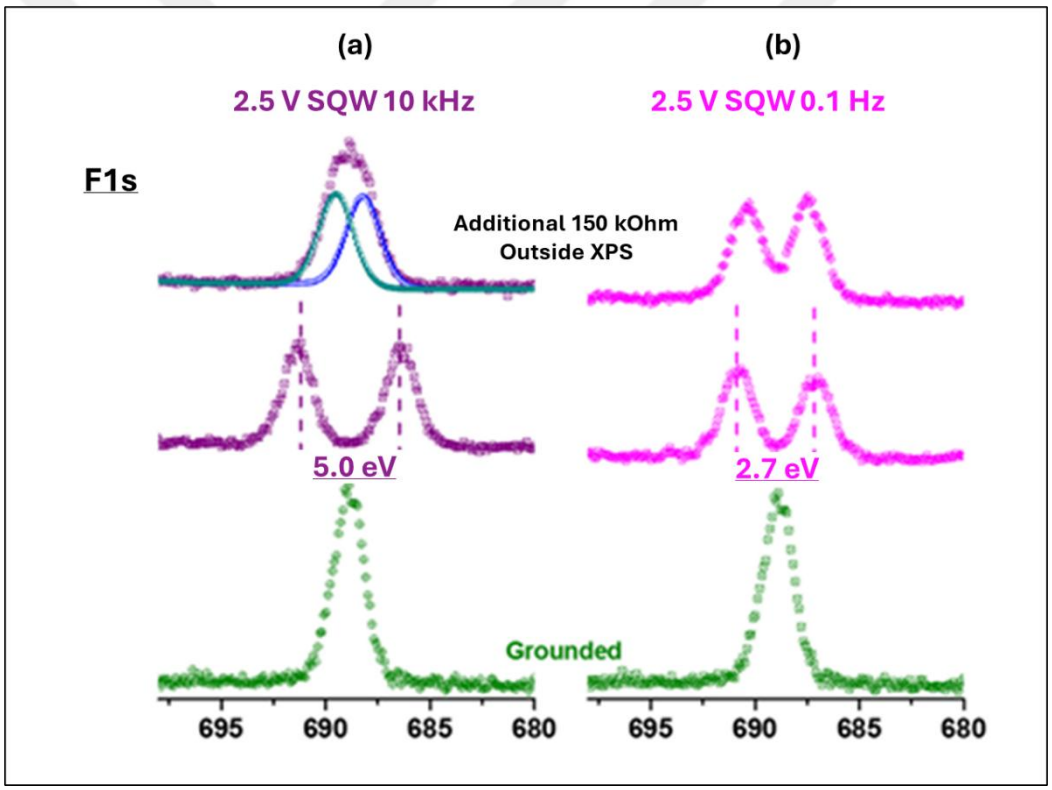

Figure 22. F1s region's XP Spectra. Under 2.5 V SQW Excitations and with the additional 150 kOhm Resistor: Inside and Outside the spectrometer, together with the grounded one. (a) 10 kHz, (b) 0.1 Hz. (Reprinted with permission from Karaoglu, G., Kutbay, E., Ince, S., Ulgut, B., and Suzer, S. Assessing Local Electrical Properties of Ionic Liquid/Metal Interfaces with Operando-XPS and by Incorporating Additional Circuit Elements. *Anal Chem* **2023**, *95* (40), 14861–14869. Copyright 2023, American Chemical Society.)

3.2.3 Electrical Impedance Spectroscopy

Electrochemical impedance spectroscopy (EIS) was performed on the IL device to quantitatively characterize its frequency-dependent impedance response. In Figure 23, the results for the pure IL device before XPS measurements, after 8 hours of X-ray exposure and after the addition of 2 150 kΩ resistors. EIS experiments showed that the device impedance varies significantly with frequency, ranging from ~1.0 MΩ at 0.1 Hz to ~10 kΩ at 10 kHz, shown in Figure 23(b).

The model used to fit the impedance spectra consists of a parallel resistor representing the Faradaic charge transfer resistance, R_{CT} and the parallel capacitor C_{IL} represents the double-layer capacitance of the ionic liquid as illustrated in Figure 23(c). The external resistor, R_{ADD} accounts for the resistors that are introduced in series in the experimental set-up in addition to any inherent resistances within the system. Finally, a small capacitance, C_{cable}, reflects the parasitic capacitance of the measurement set-up, including contributions from connectors and BNC cables linking the device to the measuring instrument.

Based on the fitting results presented in Figure 23(c), the additional series resistance was determined as 290 kΩ from the Nyquist plot in Figure 23(a) which is in close agreement with the expected 300 kΩ, the sum of the two external resistors. C_{IL} was found to be ~1.7 μF that matched well with known resistor values and literature expectations.[126,127] A much smaller capacitance, 300 pF was found for C_{cable} and this can be attributed to parasitic capacitance rather than geometric capacitance as this small capacitance appears in parallel with the external resistor, R_{ADD}, and contributes to the high-frequency semi-circle in Figure 23(a).[128]

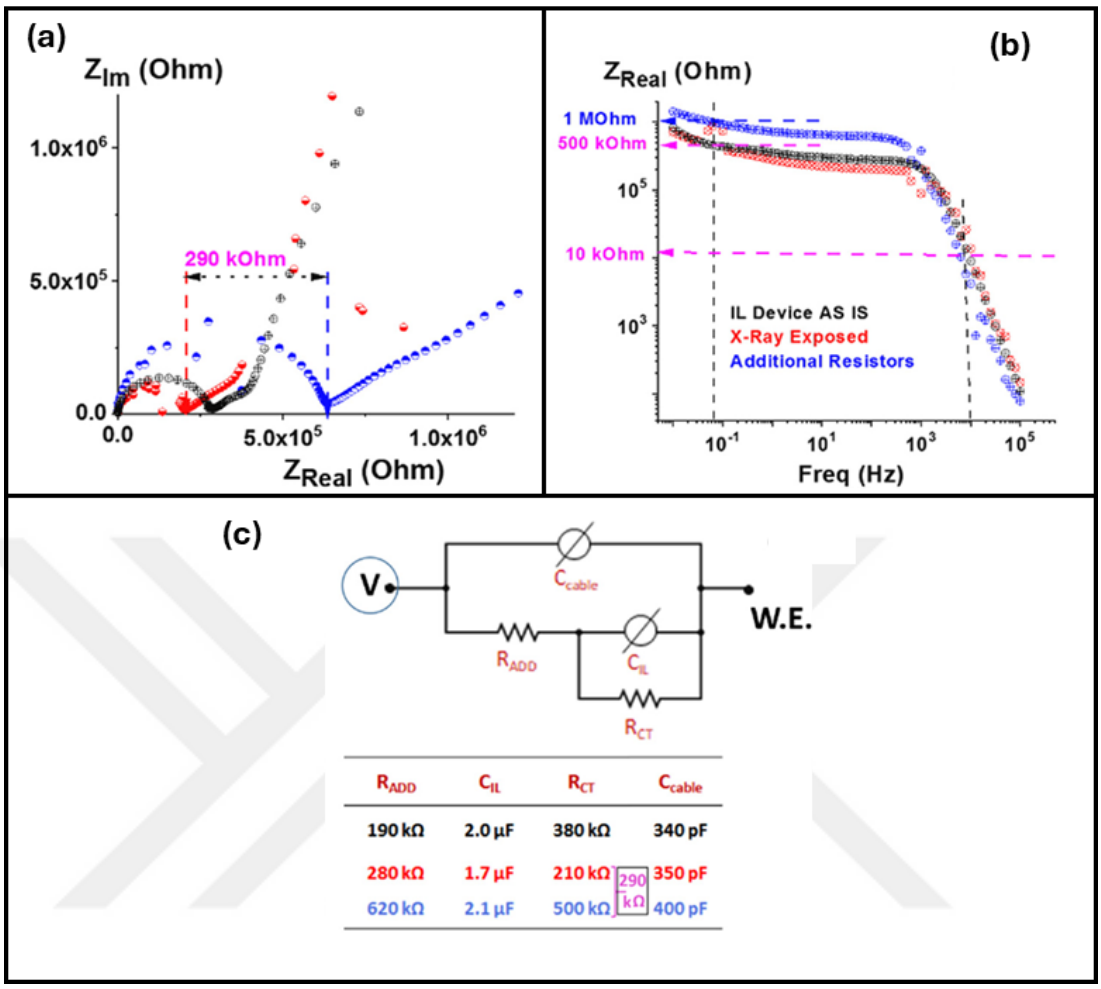

Figure 23. Electrochemical impedance spectroscopy (EIS) results for three distinct configurations of the device: (i) the IL device in its original state (black), (ii) after over 8 hours of X-ray exposure (red), and (iii) after adding external resistors (blue). (a) Nyquist plots displaying the real and imaginary parts of the impedance, with the external resistors clearly identified as 290 kΩ. (b) Impedance magnitude as a function of frequency for the three configurations, showing a significant decrease from 1.0 MΩ at 0.1 Hz to 10 kΩ at 10 kHz. (c) The equivalent circuit model used and the electrical parameters for each of the device configurations. (Reprinted with permission from Karaoglu, G., Kutbay, E., Ince, S., Ulgut, B., and Suzer, S. Assessing Local Electrical Properties of Ionic Liquid/Metal Interfaces with Operando-XPS and by Incorporating Additional Circuit Elements. *Anal Chem* **2023**, *95* (40), 14861–14869. Copyright 2023, American Chemical Society.)

3.2.4 Equivalent Circuit Modelling

LT-Spice simulations and python were previously used hand in hand to complement XPS measurements and gain deeper insight into the system's dynamic electrical response in Suzer Research Group previously on studies on electrowetting and electrochemical behavior.[129,130] The approach taken in this thesis involves first constructing an approximate equivalent circuit model, guided by measured current values and known device parameters such as capacitance and resistance. The output voltage profiles generated by the simulation, corresponding to different local positions along the device and at designated modulation frequencies, are then convoluted with the F1s region XPS spectrum recorded under no bias to generate synthetic spectra that can be directly compared to the experimental data.

To align the simulated output with the XPS measurements, an additional parallel resistor of approximately 1 MΩ was included in the model. This adjustment aligns with the long-time limiting behavior (over 300 s) observed experimentally under 2.5 V pulsed excitation, as well as the measured impedance values obtained in the presence of an external 300 kΩ resistor. Additionally, the serial resistance of the IL device itself was set to 450 kΩ to better replicate the real device impedance captured in the XPS experiments.

For the more complex geometries investigated in this work—particularly configurations with series resistors introduced in different positions—results from our earlier electrochemical impedance spectroscopy (EIS) measurements were used to inform the model, using overall capacitance and resistance values of 1.7 μF and 450 kΩ, respectively. Recognizing that the device capacitance is primarily dominated by

the two metal/IL interfaces, the circuit model was refined by splitting the RC element into two sections, effectively halving the resistances and doubling the capacitances to preserve the same overall time constant. The finalized equivalent circuit with 2 150 kΩ (one before and one after the IL device) resistors is illustrated in Figure 24.

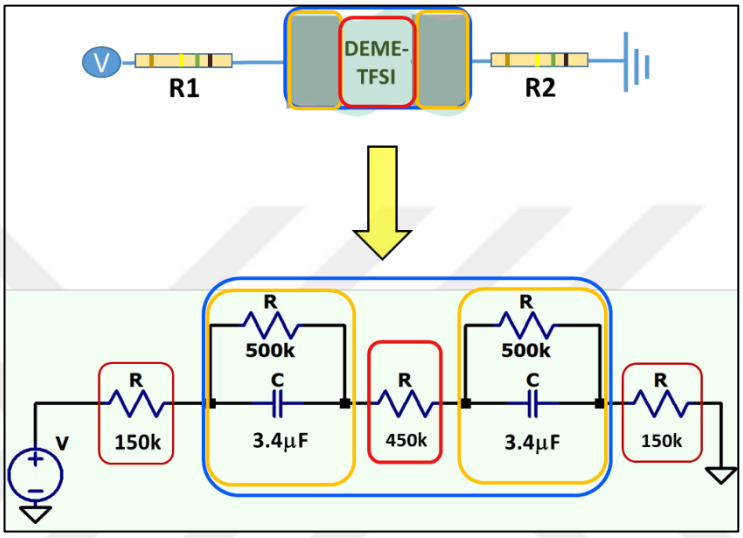

Figure 24. Equivalent Circuit Model of the Pt-Pt coplanar capacitor device with two resistors (one after and one before IL device). (Adapted from Kutbay, E., Ince, S. and Suzer, S. AC-Modulated XPS Enables to Externally Control the Electrical Field Distributions on Metal Electrode/Ionic Liquid Devices. Journal of Physical Chemistry B 2024, 128 (17), 4139–4147. Copyright 2024, American Chemical Society.)

In LTSpice, the voltage probe was placed on the point indicated by a green star in the equivalent circuit illustrated in Figure 25 and the corresponding voltage responses were recorded at 4 V 10 kHz and 0.1 Hz SQW AC bias. Using these data and convoluting with the grounded F1s spectrum, the synthetic XPS spectra are collected.

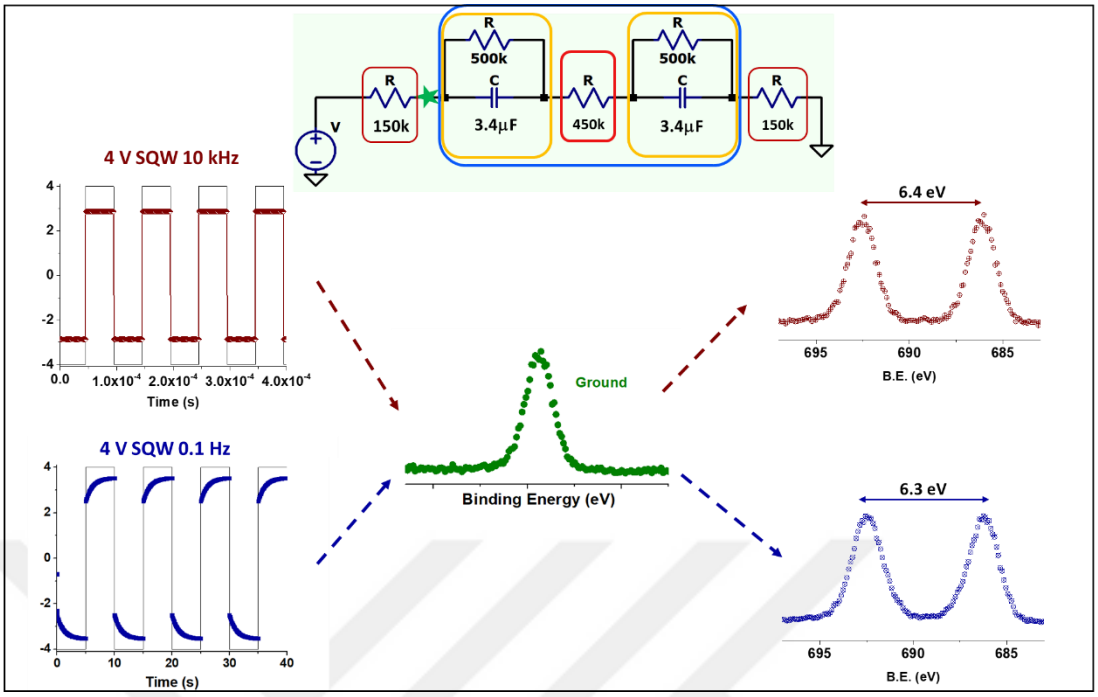

Figure 25. Synthetic spectra acquisition process starting from the acquisition of voltage response at 10 kHz and 0.1 Hz 4 V SQW voltage, the convolution process and the generation of synthetic spectra. (Adapted from Kutbay, E., Ince, S. and Suzer, S. AC-Modulated XPS Enables to Externally Control the Electrical Field Distributions on Metal Electrode/Ionic Liquid Devices. Journal of Physical Chemistry B 2024, 128 (17), 4139–4147. Copyright 2024, American Chemical Society.)

The resulting synthetic XPS spectra at corresponding local positions for the three device configurations are reproduced in Figure 26(a), Figure 26(b) and Figure 26(c), generally showing excellent agreement with the experimental data, apart from minor deviations.

In most instances, the simulated results closely match the XPS data as seen in Figure 26, with the pink arrows going from one peak of 10 kHz to 0.1 Hz, supporting the reliability of this simulation-based interpretation. It's worth noting that the observed differences in some specific configurations highlight the complexity of the system and underscore the need for further refinement—both in terms of experimental

precision (e.g., device fabrication uniformity, minimization of impurities) and in improved circuit modeling approaches.

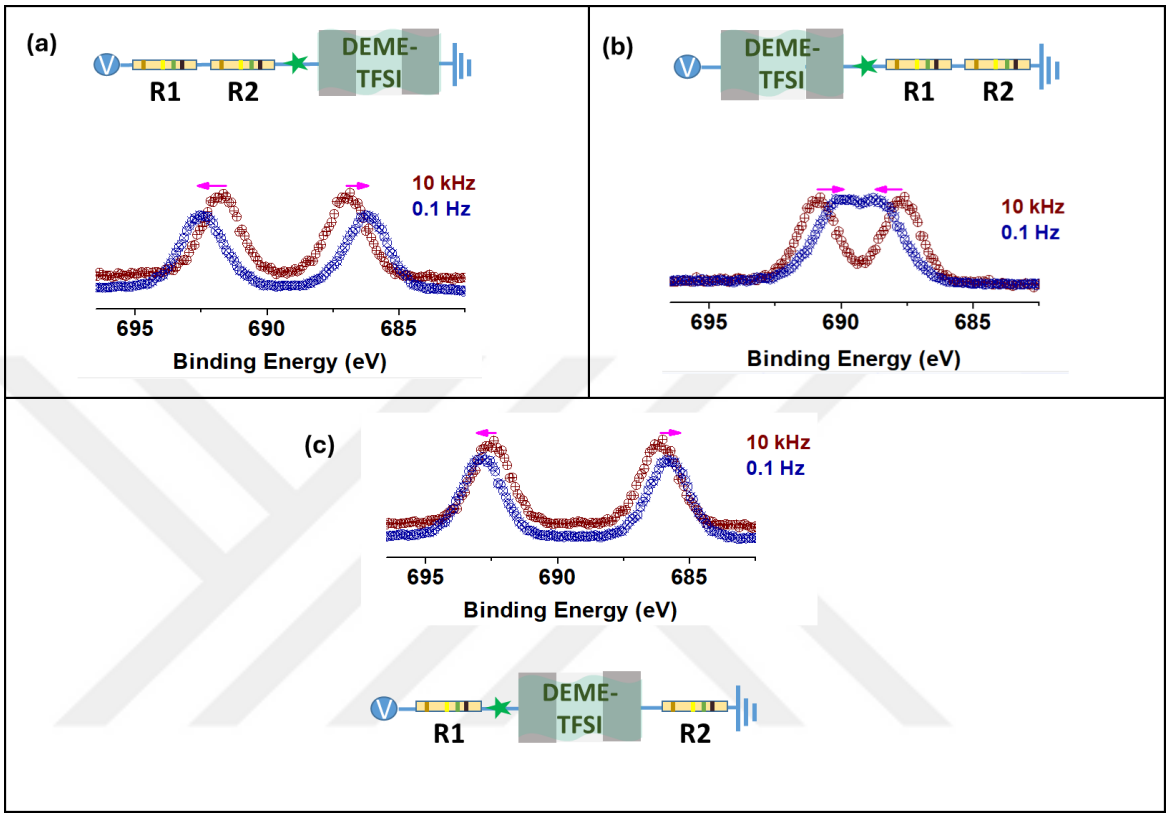

Figure 26. Synthetic spectra collected at points indicated by a green star IL device with (a) 2 resistors placed in the front, (b) 2 resistors placed at the back, (c) one resistor placed in the front and one at the back at 10 kHz and 0.1 Hz 4 V SQW voltage. (Adapted from Kutbay, E., Ince, S. and Suzer, S. AC-Modulated XPS Enables to Externally Control the Electrical Field Distributions on Metal Electrode/Ionic Liquid Devices. Journal of Physical Chemistry B 2024, 128 (17), 4139–4147. Copyright 2024, American Chemical Society.)

3.2.5 Comparison of Pure IL Devices and IL Mixtures

To assess the effect of ionic composition on device behavior, a system containing an ionic liquid mixture was prepared. The mixture prepared had a 1:1.4 (v/v) composition of DEME-TFSI and DEME-BF_4 on the surface, as calculated from

the peak areas of TFSI and BF_4 of F1s spectrum. In this way, XPS was used as a quantitative tool to determine the composition of the IL mixture. The two ILs making up the mixture differ notably in anion size and mobility, with TFSI being significantly bulkier than BF_4 as seen in Figure 27. This difference in anion size and its effect on the device's response to voltage was what was being investigated.

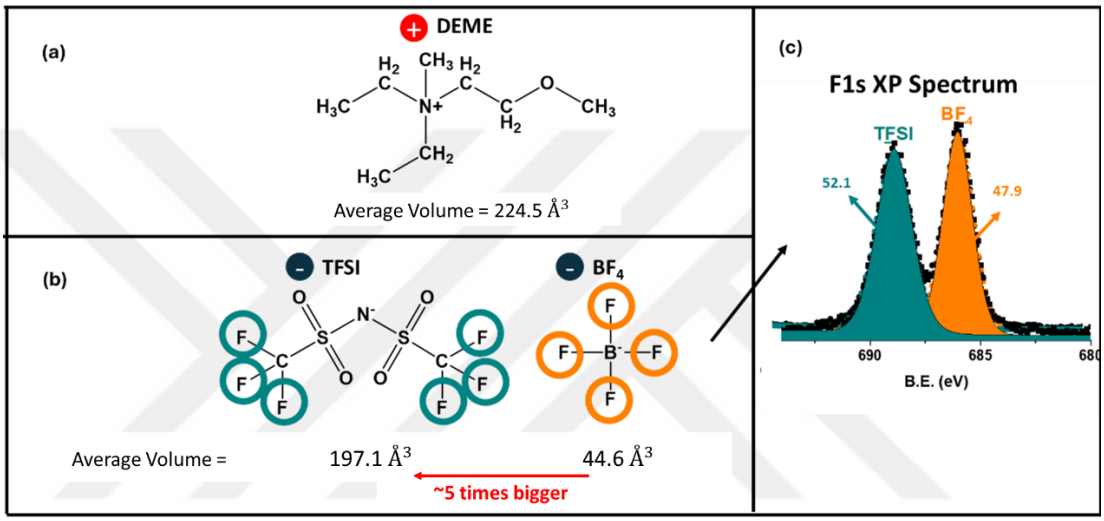

Figure 27. (a) Structure of the cation, $DEME^+$. (b) Structure of the anions, $TFSI^-$ and BF_4^-. (c) F1s grounded spectrum of the 1:1.4 (v:v) DEME-TFSI:DEME-BF_4 mixture with the areas of the two peaks corresponding to TFSI (cyan) and BF_4 (orange). The average volumes of the ions were calculated from average diameter simulation results of Kim *et al.*[131]

As introduced earlier, IL mixtures are straightforward to prepare but they exhibit complex and often unexpected physicochemical properties due to their non-ideal behavior, particularly thermal behavior. For this reason, they have long been classified as deep eutectic solvents.[132] Their electrochemical properties are also highly tunable. [91,109]

In Figure 28, a summary of XPS results obtained in the absence and presence of external resistors for IL devices containing IL mixtures are illustrated. Under 4 V SQW AC bias, since there are 2 peaks in the F1s region, there are two twinned peaks

making up four peaks in total. The binding energy shifts corresponding to these four peaks were used to compare local potential distributions of the two systems.

Upon detailed examination of the data from pure IL devices, it is clear that the binding energy shifts at 10 kHz and 0.1 Hz can be reversed by incorporating resistors at specific locations, indicating control over local potential development, the direction of these shifts remains consistent across the positive and negative cycles under SQW AC bias. However, as seen in Figure 28(b), with devices containing IL mixtures, a novel behavior emerges in which B.E. shifts differ between positive and negative cycles.

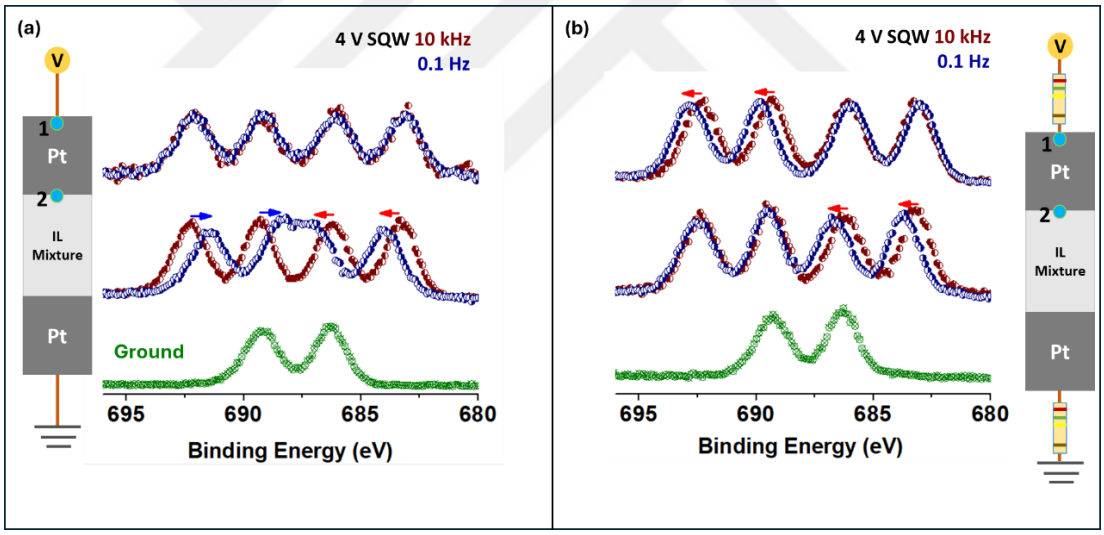

Figure 28. Schematic representation of the Pt-Pt device coated wih mixture of DEME-TFSI and DEME-BF_4: (a) without external resistors and (b) one resistor placed at the front and one at the end. Local XPS responses of F1s were recorded at points 1 and 2 under 4.0 V SQW AC modulation at 10 kHz (wine), 0.1 Hz (royal) along with the corresponding grounded spectrum (olive). (Adapted from Kutbay, E., Ince, S. and Suzer, S. AC-Modulated XPS Enables to Externally Control the Electrical Field Distributions on Metal Electrode/Ionic Liquid Devices. Journal of Physical Chemistry B 2024, 128 (17), 4139–4147. Copyright 2024, American Chemical Society.)

Moreover, differences in the degree of field reversal observed after series resistor insertion suggest that the IL mixture possesses a distinct impedance profile.

These results imply that ionic size asymmetry and composition significantly affect both the rate and spatial profile of electrochemical screening. Chemically BF_4^- is a compact anion while $TFSI^-$ is significantly larger – approximately a factor of 5 as shown in Figure 27. $TFSI^-$ is also conformationally flexible and possesses a delocalized, polarizable charge distribution.

These findings demonstrate the value of this experimental approach in isolating and analyzing the individual roles of anions and cations in dynamic charge screening within electrochemical systems. However, this behavior is yet to have been reproduced by the electrical model LTSpice simulations.

Chapter 4:

4. Results and Discussion: MLG-MLG Devices

4.1 Device Containing DEME-TFSI

4.1.1 Time-Resolved XPS: Dynamics of Charging and Discharging

The time-dependent XPS data provides direct insight into the dynamic behavior of the EDL in the MLG-MLG device under cyclic -2.0 V and +2.0 V biasing. Each measurement sequence was performed using rapid snapshot acquisition of the O1s region (~0.5 s per spectrum), repeated continuously for one hour per cycle. This approach yielded ~8000 spectra per cycle, allowing extraction of the temporal evolution of the local electrical potential in the ionic liquid (DEME-TFSI) medium.

During these measurements, the circuit was deliberately interrupted twice per cycle: first by opening the circuit (open-circuit potential condition) and later by shorting the biased electrode to ground.

At the start of the positive bias cycle, the O1s B.E. on the source electrode jumps sharply from its equilibrium position of 532.6 eV (unbiased state) to values exceeding 536 eV. This abrupt shift occurs within seconds, reflecting the immediate electronic response of the electrode surface to the applied potential. However, this high-potential state does not persist, instead, the B.E. decays exponentially towards ~534.6 eV over several hundred seconds. The decay is well-described by a

biexponential fit, revealing two dominant time constants of approximately 20 s and 200 s as shown in Figure 29. These time constants correspond to two different and slow ionic rearrangements within the EDL.

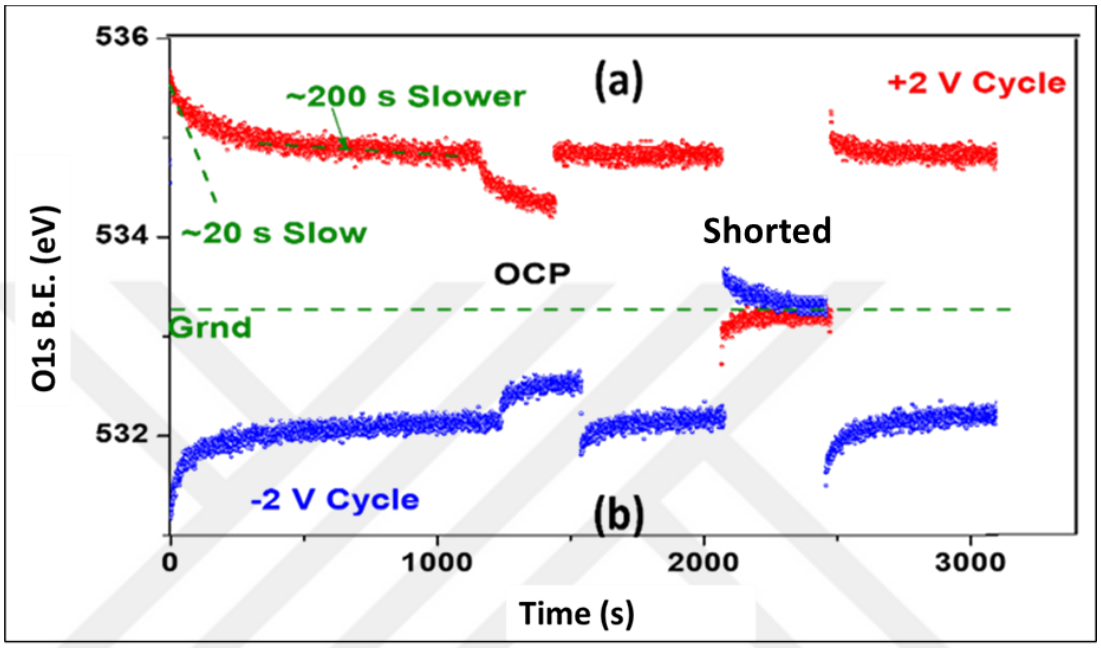

Figure 29. Biexponential fit of the O1s binding energy decay on the source electrode under +2 V bias. (a) The 2-time constants, 20 seconds (slow) and 200 seconds (slower), reflect the fast electronic screening and slower ionic rearrangement at the electrical double layer respectively. (b) The mirroring -2 V data are also shown.

During the negative bias cycle, a behavior that mirrors the positive one is observed. At the start of the negative cycle, O1s B.E. on the source electrode drops below the grounded binding energy value, quickly shifting downwards and then decaying back towards a quasi-equilibrium negative potential.

Simultaneously, the drain electrode displays complementary variations, as illustrated in Figure 31(c) and Figure 31(d) - while it does not undergo polarity reversals when grounded, its O1s B.E. oscillate in the opposite direction, driven by the induced field across the co-planar geometry.

The mirrored nature of these shifts demonstrates the near equivalency of the two electrodes. Simultaneous current measurements plotted in Figure 30, confirm that these O1s B.E. variations directly reflect the device's transient charging behavior.

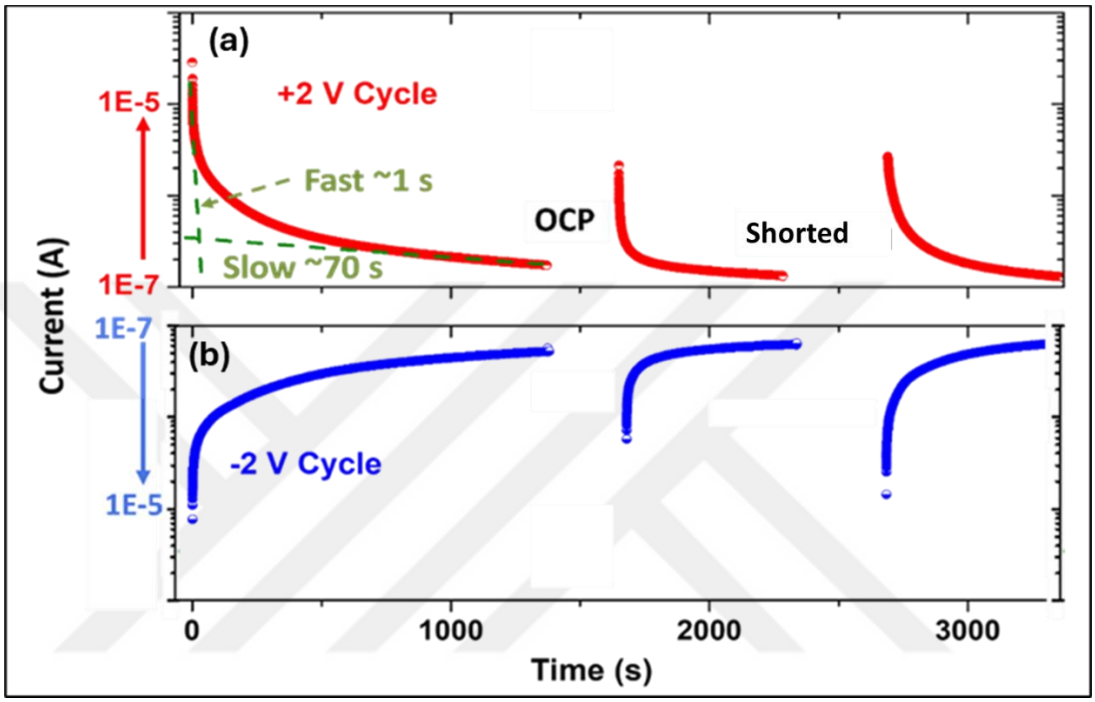

Figure 30. Current response of the MLG-MLG device under cyclic (a) +2 V bias, (b) -2 V bias. The fluctuations (sudden increase/decrease) in current correlate with the O1s binding energy shifts observed via XPS, highlighting the interplay of electronic and ionic processes during charging/discharging.

These data reflect various dynamic EDL formation components, upon biasing, open-circuit and shorting processes and set the stage for analyzing specific device behaviors also under open-circuit and grounded conditions, which are discussed in the following sections.

4.1.2 Effect of Open-Circuit Potential

To isolate the intrinsic relaxation behavior of the ionic environment, measurements were conducted under open-circuit potential (OCP) conditions—where the external bias is removed but the electrodes remain electrically floating. These periods of OCP were introduced during each bias cycle, typically lasting for about 10 minutes each, as shown in the experimental timeline as shown in Figure 31.

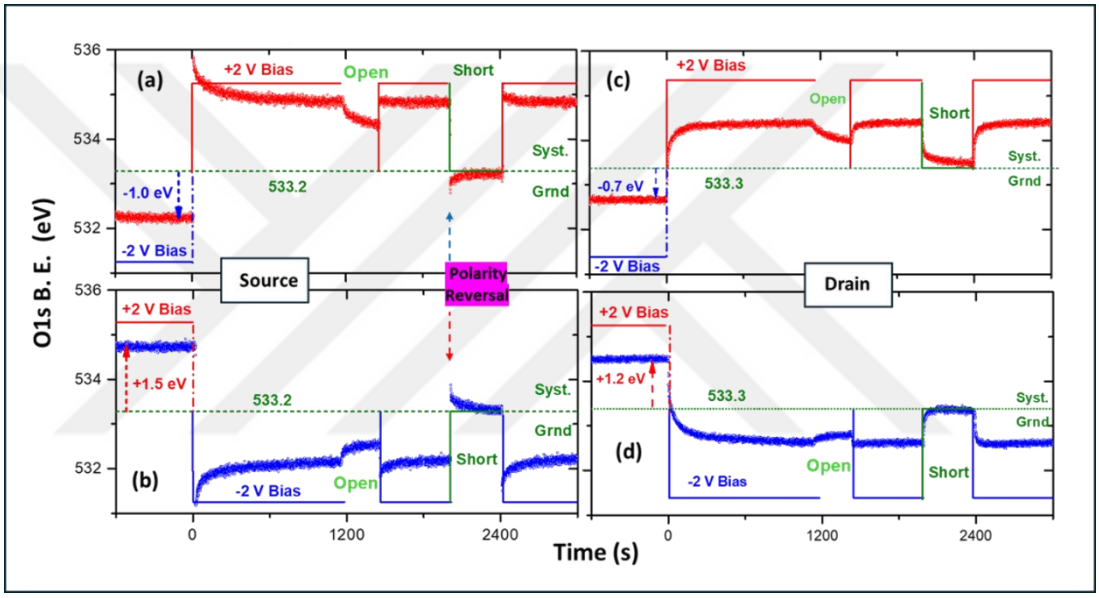

Figure 31. Evolution of O1s binding energy: on the source electrode (a) under +2 V bias. (b) under -2 V bias; on the drain electrode (c) under +2 V bias and (d) under –2 V bias. The slow decay towards equilibrium without polarity reversal under OCP conditions confirms that ionic relaxation dominates once the external bias is removed. However, the abrupt polarity reversal in B.E. after shorting reflects the fast electronic neutralization.

When the circuit is opened, the slower and gradual shifts driven, most probably by the various leakage pathways as well as by the relaxation of ionic charges are observed. Specifically, the O1s B.E. on the source electrode, which had reached above 536 eV under +2 V bias, begins to decay slowly towards a quasi-equilibrium value near the unbiased baseline of 532.6 eV as seen in Figure 31(a) and Figure 31(b).

Notably, during the entire OCP period, the B.E. remains above the baseline under +2 V bias, and below baseline under -2 V bias.

The drain electrode mirrors this behavior, the O1s B.E., previously driven to lower values with respect to the baseline during the negative bias cycle, steadily rises back toward baseline during OCP, again without crossing the zero line illustrated in Figure 31(d) and vice versa in Figure 31(c).

4.1.3 Ionic Charge Retention after Shorting

The shorting scenario presents a contrasting condition by actively resetting the electronic potential of the source electrode to zero. Unlike OCP, where the electrodes are left electrically floating, shorting forcibly resets the electronic potential of the source electrode to zero by directly connecting it to the ground. This abrupt removal of the electronic charge enables a direct examination of the residual ionic environment and its response, i.e., providing the possibility of separating electronic and ionic contributions to the EDL potential.

As shown in Figure 31(a), upon shorting during application of +2 V, the O1s B.E. on the source electrode undergoes a sudden and striking polarity reversal. Instead of continuing its slow decay from the high potential (>536 eV) achieved under bias, the B.E. abruptly drops below the unbiased baseline, reaching negative electrical potential values. This immediate polarity reversal is the biggest attribute of the shorting process: the external electronic charge is rapidly neutralized, while the ionic charges in the EDL that accumulate to screen the previous electronic bias, remain

momentarily unbalanced. Complementary behavior along with a reversal in polarity is observed when shorting after the application of -2 V bias.

The subsequent slow recovery of the O1s B.E. back toward baseline reflects the re-equilibration of the ionic environment as these residual ions redistribute and neutralize the local potential. This relaxation again occurs on timescales of hundreds of seconds, curiously matching the slower ionic motion observed during OCP.

Notably, this polarity reversal phenomenon is absent in OCP and has not been previously reported in similar graphene-based capacitor systems. It underlines the significant disparity between electronic and ionic response timescales: while electronic charges adjust almost instantaneously to the new zero-potential condition upon shorting, the ionic component responds much more slowly, initially preserving the polarity of the prior bias before eventually neutralizing it.

The drain electrode after shorting following the application of +2.0 V, as shown in Figure 31(c) exhibits complementary behavior: while its O1s B.E. does not undergo polarity reversal, it follows a similar slow relaxation back to baseline, mirroring the redistribution of ionic charges at the grounded interface. A compatible behavior is observed in Figure 31(d) for shorting after the application of -2 V.

These observations are consistent with theoretical models of EDL behavior, such as the transmission line model,[133,134] which predicts a hierarchy of time constants for electronic and ionic processes in porous carbon systems. The time-resolved XPS data provide direct experimental evidence for this separation, revealing how the

interplay of these two charge components governs the transient electrochemical behavior of the system.

To illustrate this mechanism, a schematic representation is provided in Figure 32, which overlays a part of the O1s B.E. variations that is recorded on the source electrode with cartoons of the charge distributions before and after shorting. Under +2 V bias, the electrode accumulates positive electronic charge that is screened by nearby IL anions (as well as cations). When the circuit is shorted, the electronic charge is neutralized nearly instantaneously, so the ionic charges remain momentarily unbalanced. This mismatch leads to a temporary polarity reversal in the local electric potential, observed as a sharp drop in the O1s B.E. below the unbiased baseline, also illustrated in Figure 31(a).

Over time, the residual ions redistribute, and the system returns to equilibrium, completing the relaxation process. The cartoons in Figure 32 help in visualizing the temporal decoupling of the ionic and electronic contributions and emphasize a reversal that is unique to the shorting condition.

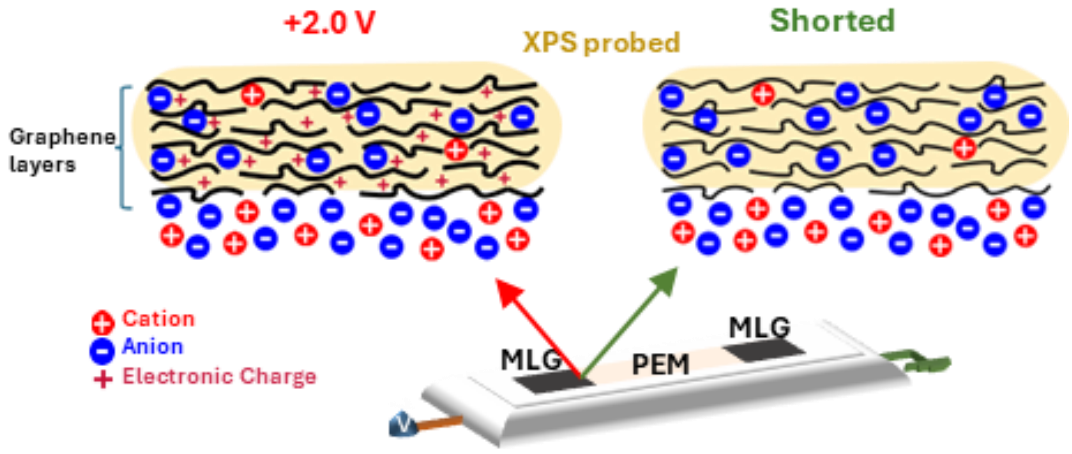

Figure 32. Mechanistic visualization for polarity reversal on the source electrode upon shorting, after application of +2.0 V.

The opposite is true for negative potentials. Now, the cations remain on the probed region when the negative charge is neutralized upon shorting. Therefore, a temporary reversal to values above the unbiased baseline is observed. sThe ability to observe and quantify this polarity reversal at the very same electrode upon shorting is particularly significant. It highlights a previously underexplored aspect of the EDL's dynamic nature and suggests that similar shorting-induced reversals could be an important factor to guide the design and operation of next-generation capacitive energy storage devices, especially those using high-surface-area carbon-based electrodes.

4.1.4 Asymmetric Charge Accumulation and Capacitance Behavior

Complementing the time-resolved XPS data, current measurements in Figure 33 reveal notable asymmetries in the charge accumulation behavior of the MLG-MLG device under alternating positive and negative biasing. These asymmetries manifest as differences in the magnitude and persistence of the induced currents, which also correlate directly with the evolution of the O1s B.E. observed in XPS.

Specifically, after prolonged application of -2 V bias for 30 minutes, the recorded current increases significantly—by more than an order of magnitude—compared to the initial current under the same bias magnitude (Figure 33, data in orange). Furthermore, this enhanced current response exhibits strong polarity dependence: the current increase is even more pronounced upon switching to +2 V bias. In other words, the observed current asymmetry and the related O1s B.E. shifts (Figure 31) reveal that the ionic liquid's ability to screen electrode potentials is strongly influenced by the previous biasing history.

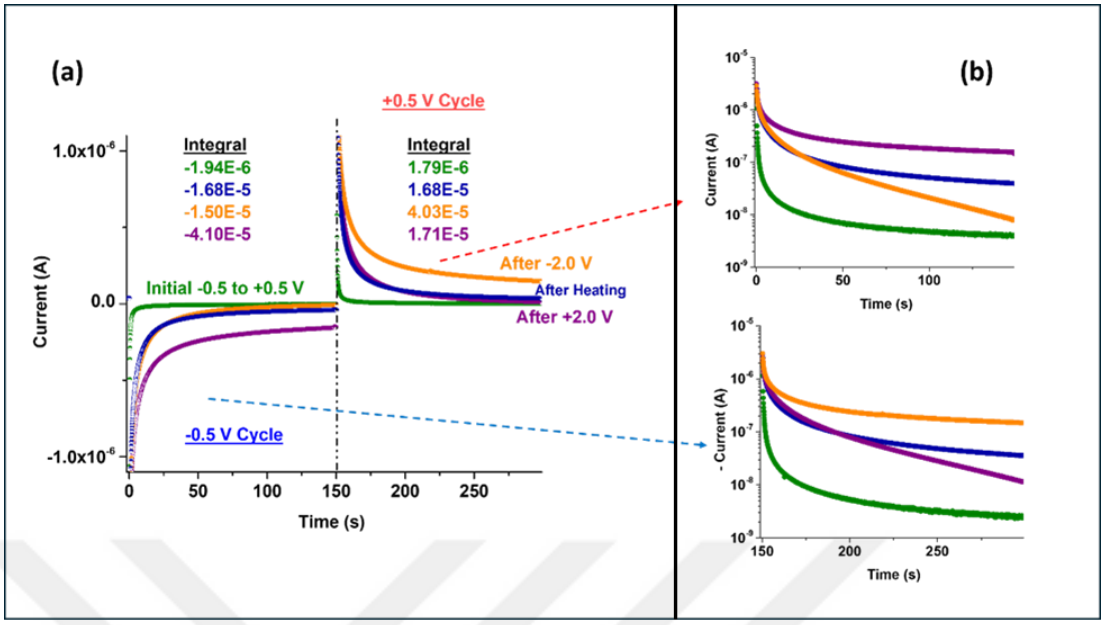

Figure 33. (a) Current measurements under -0.5 V and +0.5 V bias for a duration of 150 s each. The initial currents are shown with olive data points, which increase after application of -2.0 V bias for a duration of 30 minutes (1800 s) and becomes asymmetric (orange). Application of +2V bias for the same duration also causes an increase in currents and creates asymmetry in the opposite direction (purple). (b) Zoomed-in view of 150-300 s region from the current-time curve shown in (a). (c) The same 150-300 second current data presented on a logarithmic log(current) scale.

This behavior points to a history-dependent charge accumulation within the device, likely driven by electrosorption processes that expand the electroactive area over time. The presence of long-lived trapped charges within the ionic environment enhances electrosorption effects, leading to cumulative expansion of the effective EDL and the associated capacitance.

Combined current and electrochemical impedance spectroscopy (EIS) measurements reveal key insights into the evolving electrochemical behavior of the MLG–MLG device. Following long-term ±2 V cycling, the total charge passed during a ±0.5 V voltage step was estimated by integrating the current over time:

$$Q = \int_0^{300} I(t)dt$$

This integration yielded a total charge of approximately 250 μC. Taking the voltage step as 1 V (from -0.5 to +0.5 V), the total capacitance was calculated as:

$$C = \frac{Q}{V} = \frac{250\ \mu C}{1\ V} = 250\ \mu F$$

The corresponding gravimetric capacitance is determined using the total mass of the two MLG electrodes (~80 µg):

$$C_{gravimetric} = \frac{C_{total\ capacitance}}{mass\ of\ active\ material} = \frac{250\ \mu F}{80\ \mu g} \cong 3\ F/g$$

While this capacitance value is modest compared to that of advanced porous carbon-based supercapacitors (>100 F/g)[135], it is still notable given the device's simple planar geometry and limited electroactive surface area.

Notably, a comparison of EIS data before and after prolonged cycling shows an increase in leakage resistance plotted in Figure 34(a), while time constants remain relatively unchanged. Additionally, the emergence of a clear Warburg element suggests enhanced ionic diffusion contributions at later stages. These features—particularly the increased resistance and visible diffusive component—are consistent with the accumulation of long-lived charges, which also manifest as persistent current responses in the time domain.

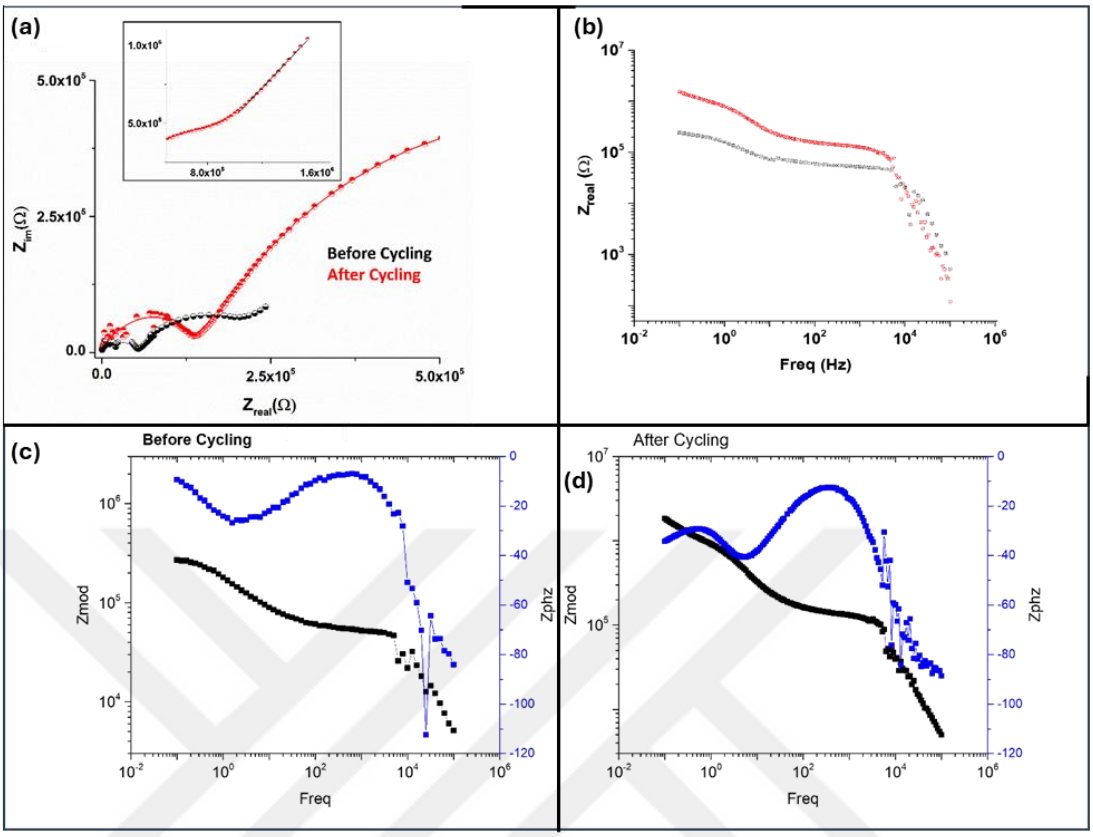

Figure 34. EIS Measurements before and after Cycling for 14 hours. (a) Nyquist plots before (black) and after (red) cycling. Bode plots (c) Before and (d) After cycling.

This asymmetric charging behavior has significant implications for practical device applications. In real-world energy storage systems, where repeated cycling is the norm, such history-dependent capacitance changes can impact performance metrics like energy density and charge-discharge efficiency. Moreover, the ability to track these changes using time-resolved XPS provides a powerful diagnostic tool for understanding and eventually optimizing these electrochemical processes.

Overall, the combined current and XPS data underline the complex interplay between ionic motion, electronic screening, and device history in determining the dynamic capacitance of the MLG-MLG device. These findings highlight the potential

of XPS-based methods to reveal subtle yet critical aspects of charge storage behavior that might otherwise be obscured in purely electrochemical measurements.

4.2 Impact of Rb^+ Inclusion on Electrosorption and Surface Composition

To explore the effects of incorporating a small-sized alkali metal cation into the electrolyte, a DEME-TFSI electrolyte containing approximately 10% Rb-TFSI was used. The goal was to evaluate how the presence of Rb^+, a significantly smaller cation compared to $DEME^+$, influences the interfacial charge distribution and electrosorption dynamics.

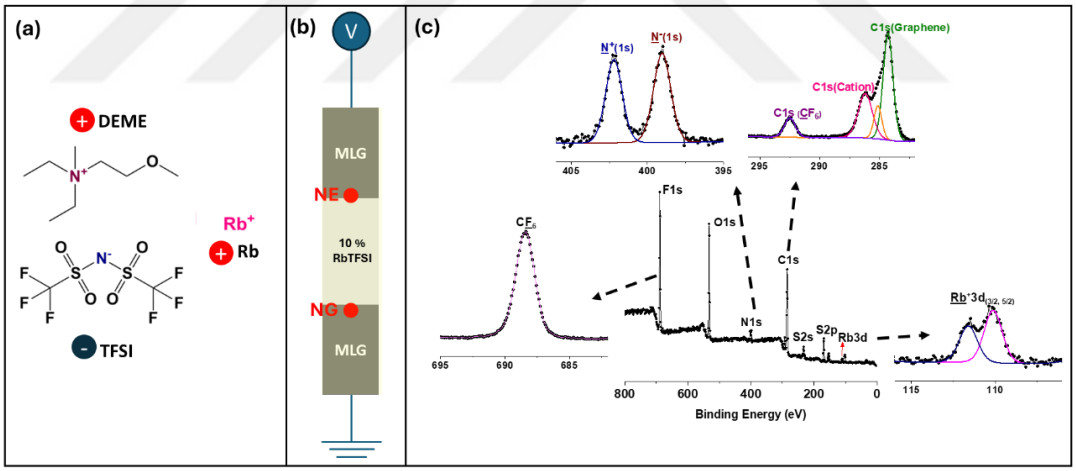

Figure 35. (a) Molecular structure of the DEME cation, TFSI anion and Rb cation. (b) The structure of the coplanar capacitor device with the near electrified electrode (NE) and near grounded electrode (NG) points marked. (c) XPS survey spectrum of the DEME-TFSI containing 10% Rb-TFSI mixture, showing peaks that are identified as C1s, N1s, F1s and Rb3d.

Figure 35(a) shows the molecular structures of DEME cation, $TFSI^-$ anion and Rb^+ cation. Based on its ionic radius of 1.5 Å, the volume of the cation is calculated to be approximately 14 $Å^3$.[136] This is a notably smaller volume compared to that of

DEME (~225 $Å^3$) and TFSI (~ 200 $Å^3$) that were calculated in section 3.2.5. Figure 35(c) the XPS survey spectrum of the Rb-TFSI IL mixture, confirming the presence of all expected elements and demonstrating sufficient signal quality across the spectral window for high-resolution tracking especially using scanning mode. Before application of any voltage, the atomic percentages of N^+, N^- and Rb^+ were 3.7 %, 3.3 % and 0.7 % respectively.

As detailed in the experimental section, the data was recorded using scan mode XPS measurements. The voltage ramp protocol involved incremental DC steps from 0 V to ±3.0 V, with three scans acquired at each voltage step and additional scans at 0 V after returning to ground to track relaxation behavior. Measurements were conducted at two characteristic points, point near the electrified electrode (NE) and point near grounded electrode (NG) as illustrated in Figure 35(b). It was observed that there is a notable change in the binding energy and also the atomic ratios during voltage ramping. By monitoring the Rb3d, N1s, C1s and F1s core-levels, it was possible to trace both cationic and anionic species under operando conditions.

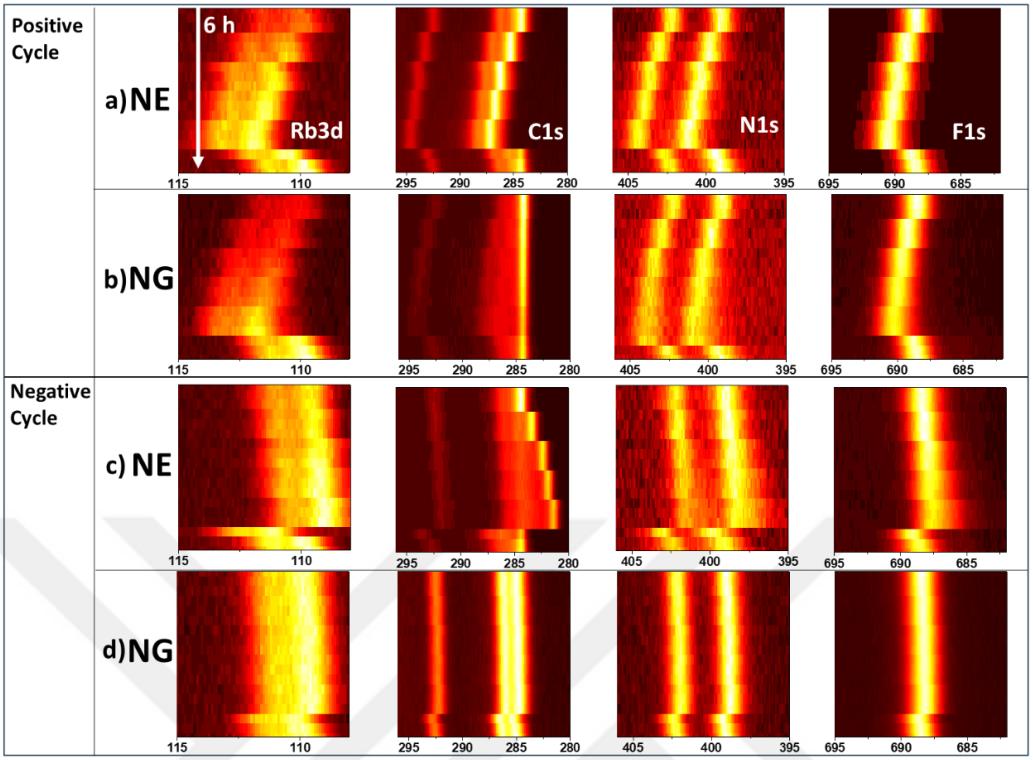

Figure 36. (a) Summary of positive voltage ramping at the electrified electrode (point NE), showing progressive binding energies of Rb3d, C1s, N1s and F1s going from left to right displayed in 2D. (b) Corresponding spectra at the grounded electrode (point NG). (c) Negative voltage ramping results at point NE. (d) Negative voltage ramping response at point NG.

During the positive voltage cycle, a progressive increase in binding energy was observed across all spectra, reflecting the increasing electrostatic potential near the electrified electrode (point NE marked in Figure 35(b)), as shown in Figure 37(a). Upon returning to 0 V, a partial rebound toward lower B.E. values relative to the grounded state was recorded. This is consistent with the transient polarity reversal behavior previously discussed in section 4.1.3 for the device containing only DEME-TFSI. The delayed return to grounded state upon shorting a relaxation process that is likely governed by ionic rearrangements in the electric double layer. A summary of all the results during positive voltage ramping at point NE and point NG are presented

in Figure 36(a) and Figure 36(b) respectively. The negative voltage ramping results are summarized in Figure 36(c) for point NE and in Figure 36(d) for point NG.

Using peak areas of only Rb3d and N1s, atomic percentages of these species were calculated. In Figure 37(b), the changes in atomic percent of Rb3d and N1s (both cationic and anionic component) are given across the 20 spectra acquired under positive voltage ramp at point NE. It was observed that the atomic percent of Rb^+ increased with increasing voltage, while the cationic N1s signal that is associated with $DEME^+$ decreased. In contrast, the anionic N1s component and therefore, F1s signal remained largely unchanged. Notably, the combined atomic percent of the two cations (Rb^+ and N^+) closely approached that of the N^- that is associated with $TFSI^-$. This observation suggests a cointercalation-like surface neutralization process where the surface charge is compensated by the coordinated arrangement of both large and small cations alongside anions. This behavior may stem from the ability of Rb^+ to approach the electrode surface more readily than a bulkier species like $DEME^+$, due to its smaller ionic radius and consequently, its higher mobility.

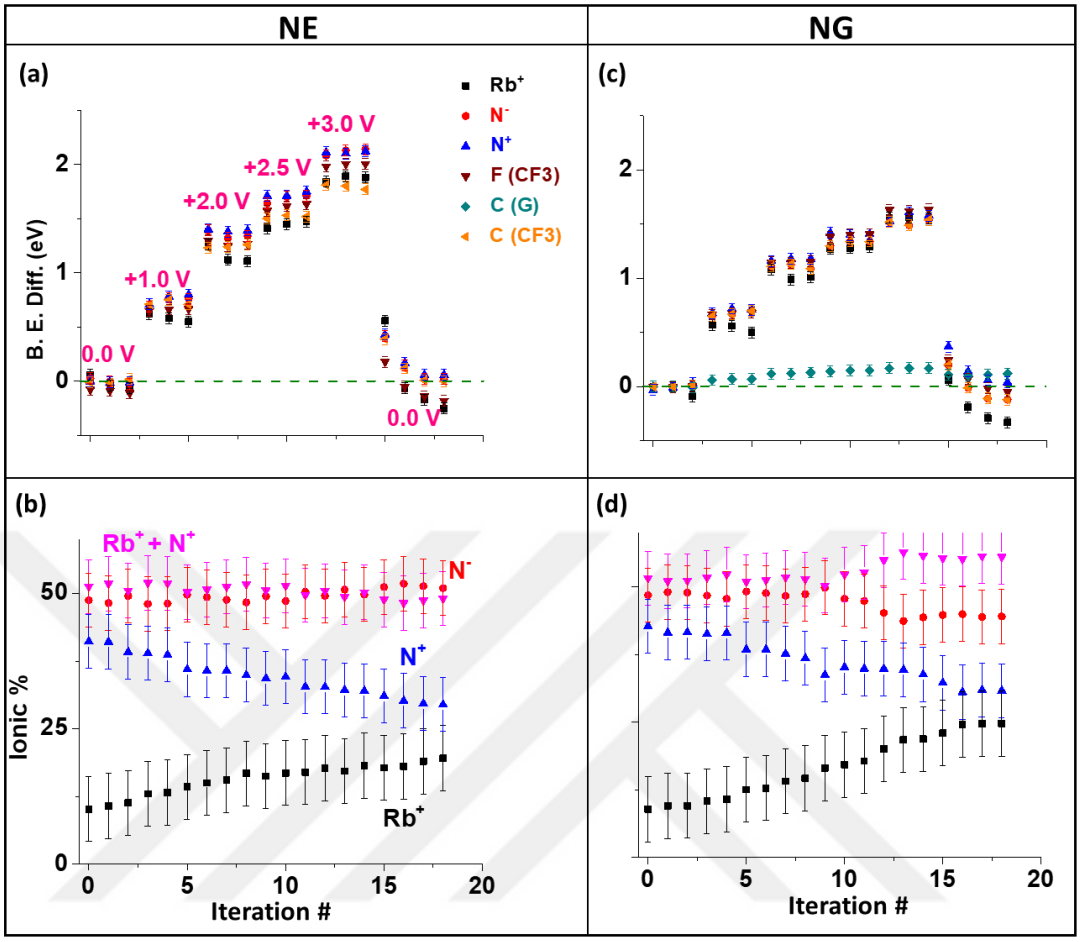

Figure 37. (a) Binding energy shifts with respect to the grounded state (0 eV); (b) Evolution of atomic percentages for Rb3d, cationic N1s, N^+ and anionic N^- during the positive voltage ramping at point NE; (c) Binding energy shifts with respect to the grounded state (0 eV); (d) Evolution of atomic percentages for Rb3d, cationic N1s, N^+ and anionic N^- during the positive ramping at point NG.

When analyzing the C1s spectrum at the grounded electrode under positive voltage ramp (Figure 37(c)), little to no shift (around 0.10 eV maximum at voltage maximum of +3.0 V, as presented in Figure 38) was observed in the peak corresponding to graphene with grounded state binding energy of 284.3 eV, which is expected, as the grounded side serves as the reference potential and its environment should remain electrostatically stable.

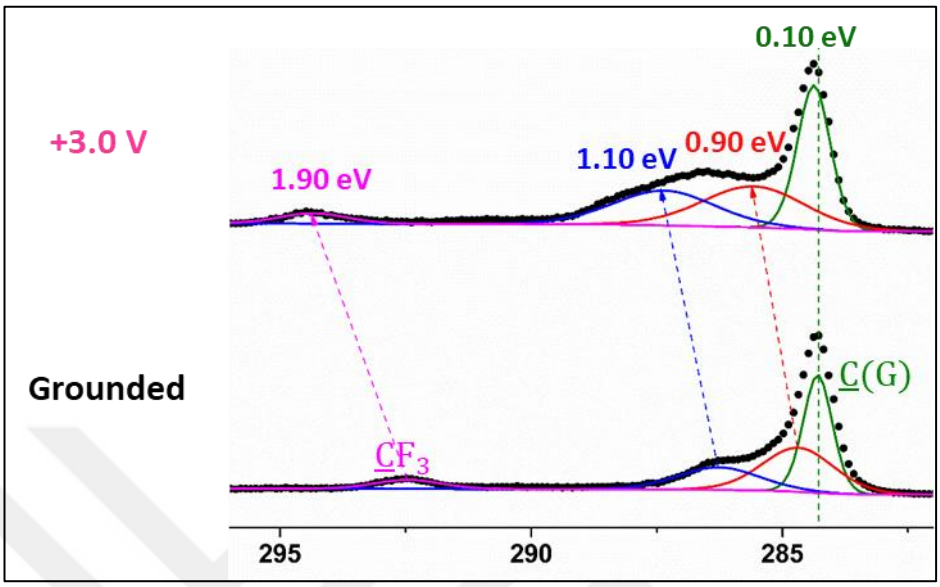

Figure 38. C1s region at point NG. Spectra acquired when the coplanar capacitor is grounded and under +3.0 V bias.

However, C1s peak that is associated with CF_3 groups of TFSI, and other cationic carbon environments did show responses to the applied voltage, (although smaller compared to the response at point NE due to intrinsic voltage drop), reflecting the behavior of mobile ionic species that are not electrically grounded. At the point NG, similar to that of point NE, a decrease in the atomic percentage of N^+ and a corresponding increase in Rb^+ was observed. However, in this case, the sum of Rb^+ and N^+ atomic percentages did not consistently match the atomic percent of the anionic N1s component, especially at higher voltages as seen in Figure 37(d).

This difference may arise from several factors that include local field gradients that cause spatial redistribution at this local point. It may also be that the cation

exchange process is not synchronized with the dynamics of the anion at these voltages under the specific conditions.

In contrast, during the negative voltage cycle, which was conducted using the same stepwise protocol, much smaller changes were observed in both binding energies and surface atomic compositions. This noticeable asymmetry between the positive and negative cycles suggests a cation-dominated mechanism, which is not reciprocated under negative voltage likely due to the limited mobility of the anions or their exclusion from the surface. This directional response is very similar to the behavior of a diode, where charge accumulation and interfacial restructuring occur preferentially under one polarity which suggests the formation of an asymmetric electrochemical interface.

Additionally, this asymmetry is particularly evident at the point NG as seen in Figure 39(c) and Figure 39(d). Unlike the behavior observed under positive voltage or at the electrified electrode, no significant change in surface composition was detected with respect to voltage at this point. Another important observation is that the atomic percent of N^+ increases with Rb^+ while the anionic N^- component decreases at point NE as shown in Figure 39(b).

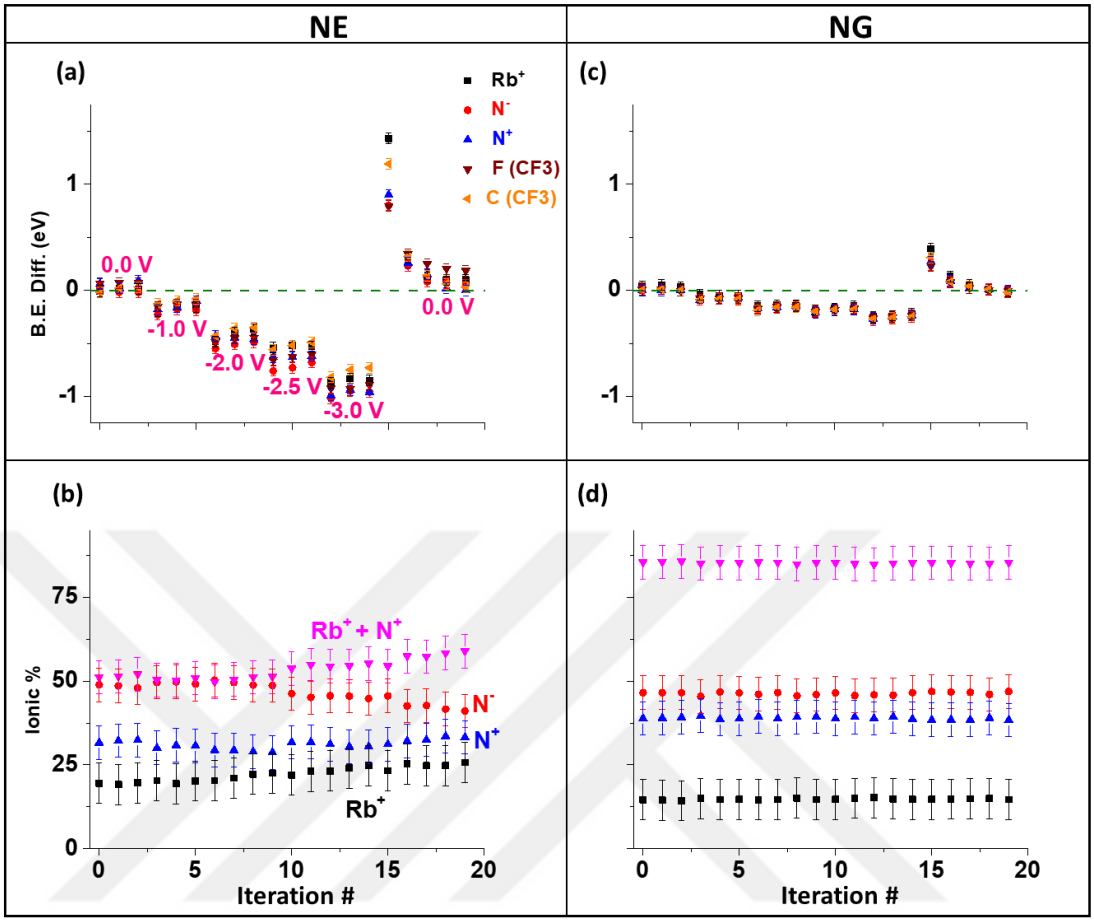

Figure 39. (a) Binding energy shifts with respect to the grounded state (0 eV); (b) Evolution of atomic percentages for Rb3d, cationic N1s, N^+ and anionic N^- during the negative voltage ramping at point NE; (c) Binding energy shifts with respect to the grounded state (0 eV); (d) Evolution of atomic percentages for Rb3d, cationic N1s, N^+ and anionic N^- during negative ramping at point NG.

It is also important to note that upon returning to 0 V after the negative voltage ramp shown in Figure 39(a), a polarity reversal in binding energy is again observed at point NE, mirroring the behavior of the pure DEME-TFSI device and also the observations from the positive ramping cycle. Relaxation to a lower/higher binding energy state at positive/negative voltages is a general feature of the system no matter the content of the IL electrolyte.

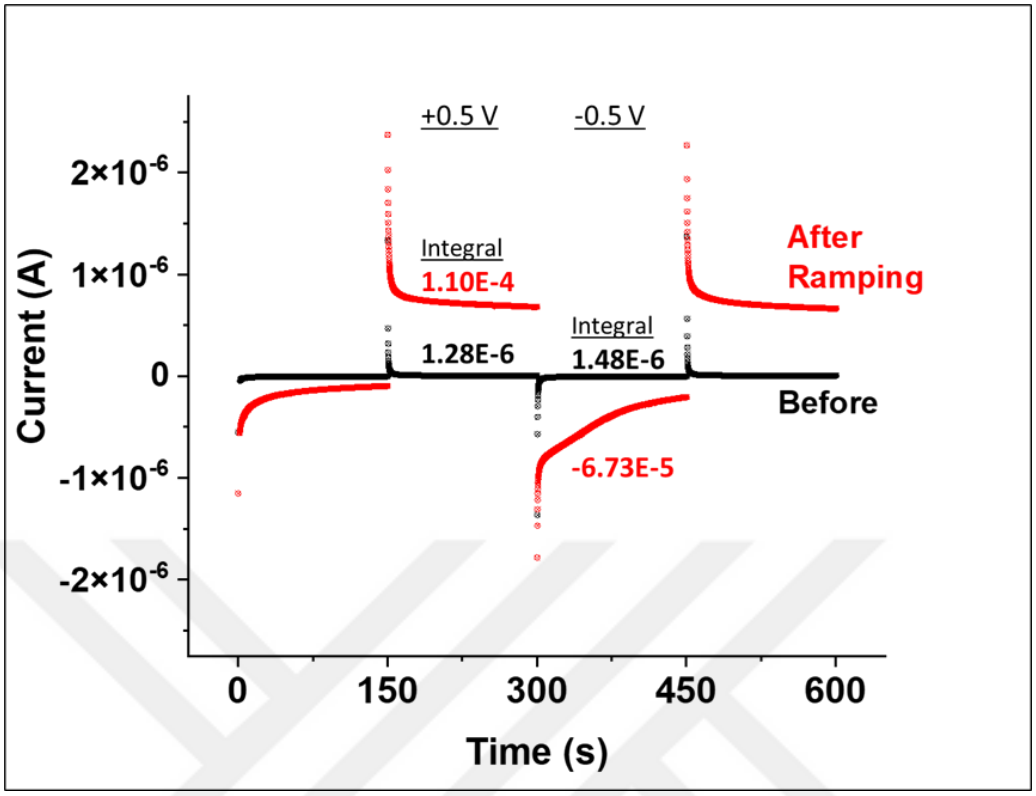

Figure 40. Current–time response of the MLG–MLG device containing DEME-TFSI with 10% Rb-TFSI before and after voltage cycling.

The system also exhibited a dramatic increase in current on the order of nearly two magnitudes as presented in Figure 40. This was first interpreted as evidence of electrosorption, particularly due to the surface accumulation of Rb^+ that was observed. An increase in current suggests an enhancement of ionic activity. The rise of the current may be due to interfacial processes such as surface electrosorption and EDL restructuring, rather than any bulk insertion or modification of the graphene layers.

Coming back to the XPS results' analysis, this conclusion is also backed up here. Under positive voltage response, the surface composition of Rb^+ increases and the cationic N1s signal from DEME decreases, suggesting a competitive or cooperative electrosorption process that includes both cations. Their sum is also approaching that of N1s signal of the anionic specie which indicates a surface-level charge balancing

mechanism rather than bulk intercalation. All these observations reinforce the idea that enhanced current, and the response probed by XPS stem from field-driven electrosorption rather than structural change.

Chapter 5

5. Conclusions

This study employed operando X-ray Photoelectron Spectroscopy (XPS) under electrical bias to probe dynamics of ion behavior and interfacial potential profiles in ionic liquid (IL)-based electrochemical devices. Two complementary device configurations, Pt–Pt and multilayer graphene–multilayer graphene (MLG–MLG) sssscoplanar capacitors, were investigated under square-wave (SQW) DC and AC excitations, allowing both steady-state and time-resolved measurements.

By comparing responses at high (10 kHz) and low frequency (0.1 Hz), it was possible to distinguish between fast electronic polarization and slow ionic relaxation processes. Binding energy shifts in the F1s region for the Pt-Pt coplanar device with DEME-TFSI device served as chemically specific voltmeters to monitor local potential variations. With the addition of the external series resistors, it was possible to quantify impedance and manipulate local electric field distributions, while also confirming the directionality field reversal and screening across the IL layer. Moreover, based on these measurements, an equivalent circuit model was developed that successfully reproduced synthetic spectra closely resembling the experimental data, further validating the interpretation of responses at different frequencies and local voltage developments.

One key finding was the highlight of frequency and composition dependent charge dynamics in IL mixtures. A device containing 1:1 (v/v) mixture of DEME-TFSI: DEME-BF_4 exhibited asymmetric screening behavior, meaning the local response varied not just with voltage polarity but also with position across the device. A spatially resolved potential distribution was observed. This underlined the non-ideal and composition-sensitive behavior of IL mixture and their strong impact on interfacial electrostatics.

Time-resolved XPS measurements on MLG–MLG devices revealed a distinct polarity reversal in the O1s binding energy upon shorting, a phenomenon attributed to the mismatch in response timescales of electronic and ionic charges. This behavior reflects dynamic asymmetries in the EDL and provides experimental support for electronic and ionic contributions that evolve on different timescales, leading to transient potential reversals under specific biasing protocols.

Furthermore, incorporating ~10% Rb-TFSI into the DEME-TFSI liquid matrix introduced a small, mobile alkali cation with reasonable photoemission sensitivity. *Operando*-XPS measurements revealed preferential Rb^+ accumulation under applied bias, competitive displacement of the bulkier $DEME^+$ cation, and co-electrosorption alongside $TFSI^-$. These observations are consistent with the requirement of local electroneutrality, as the accumulation of positive ions is accompanied by the co-sorption of $TFSI^-$.

Overall, this work establishes *operando*-XPS as a chemically specific, non-invasive method to interrogate complex ion dynamics and local potential distributions in IL-based electrochemical devices. The insights gained from frequency modulation,

IL mixtures, and alkali metal inclusion may contribute to more effective design strategies for energy storage, neuromorphic devices, and iontronic platforms.

Bibliography

(1) Briggs, D.; Seah, M. P. *Practical Surface Analysis, Auger and X-Ray Photoelectron Spectroscopy*, 2nd ed.; Briggs, D., Seah, M. P., Eds.; Wiley: Chichester, **1996**; Vol. 1.

(2) Watts, J. F. X-Ray Photoelectron Spectroscopy. *Vacuum* **1994**, *45*, 653–671.

(3) Gupta, V.; Ganegoda, H.; Engelhard, M. H.; Terry, J.; Linford, M. R. Assigning Oxidation States to Organic Compounds via Predictions from X-Ray Photoelectron Spectroscopy: A Discussion of Approaches and Recommended Improvements. *J Chem Educ* **2014**, *91* (2), 232–238. https://doi.org/10.1021/ed400401c.

(4) Swartz, W. E. X-Ray Photoelectron Spectroscopy. *Anal Chem* **1973**, *45* (9), 788–800. https://doi.org/10.1021/ac60331a001.

(5) Hargittai, M. Kai M. Siegbahn (1918–2007): A Pioneer in High-Resolution Electron Spectroscopy. *Struct Chem* **2022**, *33* (1), 307–310. https://doi.org/10.1007/s11224-021-01865-0.

(6) Fahlman, A.; Hamrin, K.; Hedman, J.; Nordberg, R.; Nordling, C.; Siegbahn, K. Electron Spectroscopy and Chemical Binding. *Nature* **1966**, *210* (5031), 4–8. https://doi.org/10.1038/210004a0.

(7) Kobayashi, K.; Yabashi, M.; Takata, Y.; Tokushima, T.; Shin, S.; Tamasaku, K.; Miwa, D.; Ishikawa, T.; Nohira, H.; Hattori, T.; Sugita, Y.; Nakatsuka, O.; Sakai, A.; Zaima, S. High Resolution-High Energy x-Ray Photoelectron Spectroscopy Using Third-Generation Synchrotron Radiation Source, and Its Application to Si-High k Insulator Systems. *Appl Phys Lett* **2003**, *83* (5), 1005–1007. https://doi.org/10.1063/1.1595714.

(8) Puntel, D.; Kutnyakhov, D.; Wenthaus, L.; Scholz, M.; Wind, N. O.; Heber, M.; Brenner, G.; Gu, G.; Cava, R. J.; Bronsch, W.; Cilento, F.; Parmigiani, F.; Pressacco, F. Out-of-Equilibrium Charge Redistribution in a Copper-Oxide Based Superconductor by Time-Resolved X-Ray Photoelectron Spectroscopy. *Sci Rep* **2024**, *14* (1). https://doi.org/10.1038/s41598-024-56440-4.

(9) Watts, J. F.; Castle, J. E. The Development of Laboratory-Based High Energy Sources for XPS. *Surface and Interface Analysis* **2024**, *56* (7), 408–424. https://doi.org/10.1002/sia.7300.

(10) Yavaś, H.; Sutter, J. P.; Gog, T.; Wille, H. C.; Baron, A. Q. R. New Materials for High-Energy-Resolution X-Ray Optics. *MRS Bull* **2017**, *42* (6), 424–429. https://doi.org/10.1557/mrs.2017.94.

(11) Kutbay, E.; Ince, S.; Suzer, S. AC-Modulated XPS Enables to Externally Control the Electrical Field Distributions on Metal Electrode/Ionic Liquid Devices. *Journal of Physical Chemistry B* **2024**, *128* (17), 4139–4147. https://doi.org/10.1021/acs.jpcb.4c00152.

(12) Karaoglu, G.; Kutbay, E.; Ince, S.; Ulgut, B.; Suzer, S. Assessing Local Electrical Properties of Ionic Liquid/Metal Interfaces with Operando-XPS and by Incorporating Additional Circuit Elements. *Anal Chem* **2023**, *95* (40), 14861–14869. https://doi.org/10.1021/acs.analchem.3c01614.

(13) Patel, D. I.; Roychowdhury, T.; Jain, V.; Shah, D.; Avval, T. G.; Chatterjee, S.; Bahr, S.; Dietrich, P.; Meyer, M.; Thißen, A.; Linford, M. R. Introduction to Near-Ambient Pressure x-Ray Photoelectron Spectroscopy Characterization of Various Materials. *Surface Science Spectra* **2019**, *26* (1). https://doi.org/10.1116/1.5109118.

(14) Shavorskiy, A.; Schnadt, J.; Knudsen, J. Time Resolved Ambient Pressure X-Ray Photoelectron Spectroscopy; **2021**; pp 219–248. https://doi.org/10.1021/bk-2021-1396.ch009.

(15) Padley, C. S. *Theoretical Aspects of X-Ray Photoelectron Spectroscopy*; **1973**.

(16) Fahlman, A.; Nordling, C.; Siegbahn, K. *ESCA; Atomic, Molecular and Solid State Structure Studied by Means of Electron Spectroscopy*; Almqvist & Wiksells: Uppsala, **1967**; Vol. 20.

(17) Powell, C. J.; Jablonski, A. Surface Sensitivity of X-Ray Photoelectron Spectroscopy. *Nucl Instrum Methods Phys Res A* **2009**, *601* (1–2), 54–65. https://doi.org/10.1016/j.nima.2008.12.103.

(18) Wagner, C. D. Auger Lines in X-Ray Photoelectron Spectrometry. *Anal Chem* **1972**, *44* (6), 967–973. https://doi.org/10.1021/ac60314a015.

(19) Moulder, J. F. *Handbook of X-Ray Photoelectron Spectroscopy : A Reference Book of Standard Spectra and Interpretation of XPS Data*; Chastain, J., Ed.; Physical Electronics Division, Perkin-Elmer Corporation, **1992**.

(20) Escobar Galindo, R.; Gago, R.; Duday, D.; Palacio, C. Towards Nanometric Resolution in Multilayer Depth Profiling: A Comparative Study of RBS, SIMS, XPS and GDOES. *Anal Bioanal Chem* **2010**, *396* (8), 2725–2740. https://doi.org/10.1007/s00216-009-3339-y.

(21) Radvanyi, E.; De Vito, E.; Porcher, W.; Jouanneau Si Larbi, S. An XPS/AES Comparative Study of the Surface Behaviour of Nano-Silicon Anodes for Li-Ion Batteries. *J. Anal. At. Spectrom.* **2014**, *29* (6), 1120–1131. https://doi.org/10.1039/C3JA50362C.

(22) Miura-Stempel, E.; Oregon, A. G.; Harvey, S. M.; De Yoreo, J. J.; Chen, C. L.; Cossairt, B. M. CeO2 Nanoparticle Doping as a Probe of Active Site Speciation in the Catalytic Hydrolysis of Organophosphates. *ACS Appl Nano Mater* **2024**, *7* (13), 15498–15507. https://doi.org/10.1021/acsanm.4c02410.

(23) Smirnov, M. Y.; Kalinkin, A. V.; Vovk, E. I.; Bukhtiyarov, V. I. Analysis of the Oxidation State of Platinum Particles in Supported Catalysts by Double Differentiation of XPS Lines. *Journal of Structural Chemistry* **2016**, *57* (6), 1127–1133. https://doi.org/10.1134/S002247661606010X.

(24) Zhang, G.; Fan, G.; Yang, L.; Li, F. Tuning Surface-Interface Structures of ZrO2 Supported Copper Catalysts by in Situ Introduction of Indium to Promote CO2 Hydrogenation to Methanol. *Appl Catal A Gen* **2020**, *605*, 117805. https://doi.org/10.1016/j.apcata.2020.117805.

(25) Huang, Q.; Xia, G.-J.; Huang, B.; Xie, D.; Wang, J.; Wen, D.; Lin, D.; Xu, C.; Gao, L.; Wu, Z.; Wu, J.; Xie, F.; Guo, W.; Zou, R. Activating Lattice Oxygen by a Defect-Engineered Fe 2 O 3 – CeO 2 Nano-Heterojunction for Efficient Electrochemical Water Oxidation. *Energy Environ Sci* **2024**, *17* (14), 5260–5272. https://doi.org/10.1039/D4EE01588F.

(26) Cornaglia, L. M.; Lombardo, E. A. XPS Studies of the Surface Oxidation States on Vanadium-Phosphorus-Oxygen (VPO) Equilibrated Catalysts. *Appl Catal A Gen* **1995**, *127* (1–2), 125–138. https://doi.org/10.1016/0926-860X(95)00067-4.

(27) Armelao, L.; Barreca, D.; Bottaro, G.; Gross, S.; Gasparotto, A.; Maragno, C.; Tondello, E.; Zattin, A. Introduction to XPS Studies of Metal and Metal-Oxide Nanosystems. *Surface Science Spectra* **2003**, *10* (1), 137–142. https://doi.org/10.1116/11.20050199.

(28) Laïk, B.; Richet, M.; Emery, N.; Bach, S.; Perrière, L.; Cotrebil, Y.; Russier, V.; Guillot, I.; Dubot, P. XPS Investigation of Co–Ni Oxidized Compounds Surface Using Peak-On-Satellite Ratio. Application to Co 20 Ni 80 Passive Layer Structure and Composition. *ACS Omega* **2024**, *9* (39), 40707–40722. https://doi.org/10.1021/acsomega.4c05082.

(29) Esbah Tabaei, P. S.; Ghobeira, R.; Cools, P.; Rezaei, F.; Nikiforov, A.; Morent, R.; De Geyter, N. Comparative Study between In-Plasma and Post-Plasma Chemical Processes Occurring at the Surface of UHMWPE Subjected to Medium Pressure Ar and N2 Plasma Activation. *Polymer (Guildf)* **2020**, *193*, 122383. https://doi.org/10.1016/j.polymer.2020.122383.

(30) Wiącek, A. E.; Jurak, M.; Gozdecka, A.; Worzakowska, M. Interfacial Properties of PET and PET/Starch Polymers Developed by Air Plasma Processing. *Colloids Surf A Physicochem Eng Asp* **2017**, *532*, 323–331. https://doi.org/10.1016/j.colsurfa.2017.04.074.

(31) Bertin, M.; Leitao, E. M.; Bickerton, S.; Verbeek, C. J. R. A Review of Polymer Surface Modification by Cold Plasmas toward Bulk Functionalization. *Plasma Processes and Polymers* **2024**, *21* (5). https://doi.org/10.1002/ppap.202300208.

(32) Ueki, T. Stimuli-Responsive Polymers in Ionic Liquids. *Polymer Journal*. Nature Publishing Group January 1, **2014**, pp 646–655. https://doi.org/10.1038/pj.2014.37.

(33) Gawek, M.; Madkour, S.; Szymoniak, P.; Radnik, J.; Schönhals, A. Energy Dependent XPS Measurements on Thin Films of a Poly(Vinyl Methyl Ether)/Polystyrene Blend Concentration Profile on a Nanometer Resolution to Understand the Behavior

of Nanofilms. *Soft Matter* **2021**, *17* (29), 6985–6994. https://doi.org/10.1039/D1SM00656H.

(34) Cabuil, N.; Le Gouil, A.; Dickson, B.; Lagha, A.; Aminpur, M.; Chaton, C.; Royer, J.-C.; Doclot, O.; Seiler, D. G.; Diebold, A. C.; McDonald, R.; Garner, C. M.; Herr, D.; Khosla, R. P.; Secula, E. M. Process Monitoring And Surface Characterization By XPS In A Semiconductor Fabrication Line. In *AIP Conference Proceedings*; AIP, **2007**; pp 191–195. https://doi.org/10.1063/1.2799368.

(35) Jia, Y.; Fu, Y.; Liu, X.; Wang, Z.; Jiang, P.; Lu, Q.; Wang, S.; Guan, Y.; Li, L.; Chen, H.; Hao, Y. Different Temperatures Leakage Mechanisms of (Al2O3)x(HfO2)1−x Gate Dielectrics Deposited by Atomic Layer Deposition. *Sci Rep* **2025**, *15* (1), 1154. https://doi.org/10.1038/s41598-025-85686-9.

(36) Kaichev, V. V.; Dubinin, Yu. V.; Smirnova, T. P.; Lebedev, M. S. A Study of the Structure of (HfO2) x (Al2O3)1−x /Si Films by X-Ray Photoelectron Spectroscopy. *Journal of Structural Chemistry* **2011**, *52* (3), 480–487. https://doi.org/10.1134/S002247661103005X.

(37) Taner, M.; Sayar, N.; Yulug, I. G.; Suzer, S. Synthesis, Characterization and Antibacterial Investigation of Silver–Copper Nanoalloys. *J Mater Chem* **2011**, *21* (35), 13150. https://doi.org/10.1039/c1jm11718a.

(38) Hehn, I.; Schuster, S.; Wächter, T.; Abu-Husein, T.; Terfort, A.; Zharnikov, M.; Zojer, E. Employing X-Ray Photoelectron Spectroscopy for Determining Layer Homogeneity in Mixed Polar Self-Assembled Monolayers. *J Phys Chem Lett* **2016**, *7* (15), 2994–3000. https://doi.org/10.1021/acs.jpclett.6b01096.

(39) Otto, S.-K.; Moryson, Y.; Krauskopf, T.; Peppler, K.; Sann, J.; Janek, J.; Henss, A. In-Depth Characterization of Lithium-Metal Surfaces with XPS and ToF-SIMS: Toward Better Understanding of the Passivation Layer. *Chemistry of Materials* **2021**, *33* (3), 859–867. https://doi.org/10.1021/acs.chemmater.0c03518.

(40) Rizzato, A. P.; Santilli, C. V.; Pulcinelli, S. H.; Messaddeq, Y.; Hammer, P. XPS Study of the Corrosion Protection of Fluorozirconate Glasses Dip-Coated with SnO2 Transparent Thin Films. *J Solgel Sci Technol* **2004**, *32* (1–3), 155–160. https://doi.org/10.1007/s10971-004-5781-9.

(41) Kocabas, C.; Suzer, S. Probing Voltage Drop Variations in Graphene with Photoelectron Spectroscopy. *Anal Chem* **2013**, *85* (8), 4172–4177. https://doi.org/10.1021/ac400489e.

(42) Camci, M. T.; Ulgut, B.; Kocabas, C.; Suzer, S. In Situ XPS Reveals Voltage Driven Asymmetric Ion Movement of an Ionic Liquid through the Pores of a Multilayer Graphene Electrode. *Journal of Physical Chemistry C* **2018**, *122* (22), 11883–11889. https://doi.org/10.1021/acs.jpcc.8b02759.

(43) Syari'ati, A.; Kumar, S.; Zahid, A.; Ali El Yumin, A.; Ye, J.; Rudolf, P. Photoemission Spectroscopy Study of Structural Defects in Molybdenum Disulfide (MoS 2) Grown by Chemical Vapor Deposition (CVD). *Chemical Communications* **2019**, *55* (70), 10384–10387. https://doi.org/10.1039/C9CC01577A.

(44) Saeloo, B.; Saisopa, T.; Chavalekvirat, P.; Iamprasertkun, P.; Jitapunkul, K.; Sirisaksoontorn, W.; Lee, T. R.; Hirunpinyopas, W. Role of Transition Metal Dichalcogenides as a Catalyst Support for Decorating Gold Nanoparticles for Enhanced Hydrogen Evolution Reaction. *Inorg Chem* **2024**, *63* (40), 18750–18762. https://doi.org/10.1021/acs.inorgchem.4c02668.

(45) Roychowdhury, T.; Bahr, S.; Dietrich, P.; Meyer, M.; Thißen, A.; Linford, M. R. Kidney Stone, by near-Ambient Pressure XPS. *Surface Science Spectra* **2019**, *26* (1). https://doi.org/10.1116/1.5052007.

(46) Jain, V.; Kjærvik, M.; Bahr, S.; Dietrich, P.; Meyer, M.; Thißen, A.; Linford, M. R. Bovine Serum Albumin, Aqueous Solution, by near-Ambient Pressure XPS. *Surface Science Spectra* **2019**, *26* (1). https://doi.org/10.1116/1.5055229.

(47) Lu, Q.; Vardar, G.; Jansen, M.; Bishop, S. R.; Waluyo, I.; Tuller, H. L.; Yildiz, B. Surface Defect Chemistry and Electronic Structure of Pr 0.1 Ce 0.9 O 2−δ Revealed *in Operando*. *Chemistry of Materials* **2018**, *30* (8), 2600–2606. https://doi.org/10.1021/acs.chemmater.7b05129.

(48) Källquist, I.; Le Ruyet, R.; Liu, H.; Mogensen, R.; Lee, M.-T.; Edström, K.; Naylor, A. J. Advances in Studying Interfacial Reactions in Rechargeable Batteries by Photoelectron Spectroscopy. *J Mater Chem A Mater* **2022**, *10* (37), 19466–19505. https://doi.org/10.1039/D2TA03242B.

(49) Wood, K. N.; Teeter, G. XPS on Li-Battery-Related Compounds: Analysis of Inorganic SEI Phases and a Methodology for Charge Correction. *ACS Appl Energy Mater* **2018**, *1* (9), 4493–4504. https://doi.org/10.1021/acsaem.8b00406.

(50) Freiberg, A. T. S.; Qian, S.; Wandt, J.; Gasteiger, H. A.; Crumlin, E. J. Surface Oxygen Depletion of Layered Transition Metal Oxides in Li-Ion Batteries Studied by *Operando* Ambient Pressure X-Ray Photoelectron Spectroscopy. *ACS Appl Mater Interfaces* **2023**, *15* (3), 4743–4754. https://doi.org/10.1021/acsami.2c19008.

(51) Faulkner, L. R.; Bard, A. J. *Electrochemical Methods: Fundamentals and Applications*, 2nd ed.; Wiley, **2000**.

(52) Wenzel, S.; Weber, D. A.; Leichtweiss, T.; Busche, M. R.; Sann, J.; Janek, J. Interphase Formation and Degradation of Charge Transfer Kinetics between a Lithium Metal Anode and Highly Crystalline Li7P3S11 Solid Electrolyte. *Solid State Ion* **2016**, *286*, 24–33. https://doi.org/10.1016/j.ssi.2015.11.034.

(53) Wenzel, S.; Leichtweiss, T.; Krüger, D.; Sann, J.; Janek, J. Interphase Formation on Lithium Solid Electrolytes—An in Situ Approach to Study Interfacial Reactions by Photoelectron Spectroscopy. *Solid State Ion* **2015**, *278*, 98–105. https://doi.org/10.1016/j.ssi.2015.06.001.

(54) Somerville, L.; Bareño, J.; Jennings, P.; McGordon, A.; Lyness, C.; Bloom, I. The Effect of Pre-Analysis Washing on the Surface Film of Graphite Electrodes. *Electrochim Acta* **2016**, *206*, 70–76. https://doi.org/10.1016/j.electacta.2016.04.133.

(55) Li, K.; Zhang, J.; Lin, D.; Wang, D.-W.; Li, B.; Lv, W.; Sun, S.; He, Y.-B.; Kang, F.; Yang, Q.-H.; Zhou, L.; Zhang, T.-Y. Evolution of the Electrochemical Interface in Sodium Ion Batteries with Ether Electrolytes. *Nat Commun* **2019**, *10* (1), 725. https://doi.org/10.1038/s41467-019-08506-5.

(56) Groher, C.; Cupid, D. M.; Mautner, A.; Rosenberg, E.; Kahr, J. Operando GC/MS for the Investigation of Different Decomposition Pathways during Solid Electrolyte Interphase (SEI) Formation with SEI Forming Additives. *J Power Sources* **2024**, *605*, 234481. https://doi.org/10.1016/j.jpowsour.2024.234481.

(57) Camci, M. T.; Aydogan, P.; Ulgut, B.; Kocabas, C.; Suzer, S. XPS Enables Visualization of Electrode Potential Screening in an Ionic Liquid Medium with Temporal- and Lateral-Resolution. *Physical Chemistry Chemical Physics* **2016**, *18* (41), 28434–28440. https://doi.org/10.1039/c6cp04933h.

(58) Suzer, S. Differential Charging in X-Ray Photoelectron Spectroscopy: A Nuisance or a Useful Tool? *Anal Chem* **2003**, *75* (24), 7026–7029. https://doi.org/10.1021/ac034823t.

(59) Doron-Mor, I.; Hatzor, A.; Vaskevich, A.; van der Boom-Moav, T.; Shanzer, A.; Rubinstein, I.; Cohen, H. Controlled Surface Charging as a Depth-Profiling Probe for Mesoscopic Layers. *Nature* **2000**, *406* (6794), 382–385. https://doi.org/10.1038/35019025.

(60) Suzer, S.; Strelcov, E.; Kolmakov, A. Comparative *Operando* XPS and SEM Spatiotemporal Potential Mapping of Ionic Liquid Polarization in a Coplanar Electrochemical Device. *Anal Chem* **2021**, *93* (39), 13268–13273. https://doi.org/10.1021/acs.analchem.1c02779.

(61) Camci, M. T.; Ulgut, B.; Kocabas, C.; Suzer, S. In-Situ XPS Monitoring and Characterization of Electrochemically Prepared Au Nanoparticles in an Ionic Liquid. *ACS Omega* **2017**, *2* (2), 478–486. https://doi.org/10.1021/acsomega.6b00456.

(62) Aydogan Gokturk, P.; Ulgut, B.; Suzer, S. AC Electrowetting Modulation of Low-Volatile Liquids Probed by XPS: Dipolar vs Ionic Screening. *Langmuir* **2019**, *35* (9), 3319–3326. https://doi.org/10.1021/acs.langmuir.8b04099.

(63) Başaran, M.; Oz, E.; Ergoktas, S.; Kocabas, C.; Ulgut, B.; Kocabas, A.; Suzer, S. Localized X-Ray Photoelectron Impedance Spectroscopy (LoXPIS) for Capturing Charge Dynamics of an Ionic Liquid Electrolyte within an Energy Storage Device. *Faraday Discuss* **2022**, *236*, 86–102. https://doi.org/10.1039/D1FD00102G.

(64) Aydogan Gokturk, P.; Taner Camci, M.; Suzer, S. Lab-Based Operando x-Ray Photoelectron Spectroscopy for Probing Low-Volatile Liquids and Their Interfaces across a Variety of Electrosystems. *Journal of Vacuum Science & Technology A: Vacuum, Surfaces, and Films* **2020**, *38* (4). https://doi.org/10.1116/6.0000273.

(65) Aydogan Gokturk, P.; Ulgut, B.; Suzer, S. DC Electrowetting of Nonaqueous Liquid Revisited by XPS. *Langmuir* **2018**, *34* (25), 7301–7308. https://doi.org/10.1021/acs.langmuir.8b01314.

(66) Chen, S.; Zheng, Y.; Lu, Y.; Su, Y.; Bao, L.; Li, N.; Li, Y.; Wang, J.; Chen, R.; Wu, F. Enhanced Electrochemical Performance of Layered Lithium-Rich Cathode Materials by Constructing Spinel-Structure Skin and Ferric Oxide Islands. *ACS Appl Mater Interfaces* **2017**, *9* (10), 8669–8678. https://doi.org/10.1021/acsami.6b14862.

(67) Wood, K. N.; Steirer, K. X.; Hafner, S. E.; Ban, C.; Santhanagopalan, S.; Lee, S.-H.; Teeter, G. Operando X-Ray Photoelectron Spectroscopy of Solid Electrolyte Interphase Formation and Evolution in Li2S-P2S5 Solid-State Electrolytes. *Nat Commun* **2018**, *9* (1), 2490. https://doi.org/10.1038/s41467-018-04762-z.

(68) Benayad, A.; Morales-Ugarte, J. E.; Santini, C. C.; Bouchet, R. Operando XPS: A Novel Approach for Probing the Lithium/Electrolyte Interphase Dynamic Evolution. *J Phys Chem A* **2021**, *125* (4), 1069–1081. https://doi.org/10.1021/acs.jpca.0c09047.

(69) Schmidt, E.; Shi, S.; Ruden, P. P.; Frisbie, C. D. Characterization of the Electric Double Layer Formation Dynamics of a Metal/Ionic Liquid/Metal Structure. *ACS Appl Mater Interfaces* **2016**, *8* (23), 14879–14884. https://doi.org/10.1021/acsami.6b04065.

(70) Yilmaz, E.; Sezen, H.; Suzer, S. Probing the Charge Build-Up and Dissipation on Thin PMMA Film Surfaces at the Molecular Level by XPS. *Angewandte Chemie International Edition* **2012**, *51* (22), 5488–5492. https://doi.org/10.1002/anie.201201351.

(71) Uzundal, C. B.; Sahin, O.; Gokturk, P. A.; Wu, H.; Mugele, F.; Ulgut, B.; Suzer, S. X-Ray Photoelectron Spectroscopy with Electrical Modulation Can Be Used to Probe Electrical Properties of Liquids and Their Interfaces at Different Stages. *Langmuir* **2019**, *35* (52), 16989–16999. https://doi.org/10.1021/acs.langmuir.9b03134.

(72) Siegbahn, H.; Siegbahn, K. ESCA Applied to Liquids. *J Electron Spectros Relat Phenomena* **1973**, *2* (3), 319–325. https://doi.org/10.1016/0368-2048(73)80023-4.

(73) Winter, B. Liquid Microjet for Photoelectron Spectroscopy. *Nucl Instrum Methods Phys Res A* **2009**, *601* (1–2), 139–150. https://doi.org/10.1016/j.nima.2008.12.108.

(74) Bluhm, H. Photoelectron Spectroscopy of Surfaces under Humid Conditions. *J Electron Spectros Relat Phenomena* **2010**, *177* (2–3), 71–84. https://doi.org/10.1016/j.elspec.2009.08.006.

(75) Bluhm, H.; Siegmann, H. C. Surface Science with Aerosols. *Surf Sci* **2009**, *603* (10–12), 1969–1978. https://doi.org/10.1016/j.susc.2008.08.041.

(76) Fortunato, R.; Afonso, C.; Benavente, J.; Rodriguezcastellon, E.; Crespo, J. Stability of Supported Ionic Liquid Membranes as Studied by X-Ray Photoelectron Spectroscopy. *J Memb Sci* **2005**. https://doi.org/10.1016/j.memsci.2005.02.023.

(77) Xue, Y.; Liu, C.; Yang, H.; Liang, H.; Zhang, C.; Xu, Z. Supported Ionic Liquid Membrane with Highly-permeable Polyamide Armor by In Situ Interfacial Polymerization for Durable CO 2 Separation. *Small* **2024**, *20* (29). https://doi.org/10.1002/smll.202310092.

(78) Lei, Z.; Chen, B.; Koo, Y. M.; Macfarlane, D. R. Introduction: Ionic Liquids. *Chemical Reviews*. American Chemical Society May 24, **2017**, pp 6633–6635. https://doi.org/10.1021/acs.chemrev.7b00246.

(79) Ge, R.; Hardacre, C.; Jacquemin, J.; Rooney, D. W. Thermophysical Properties of Ionic Liquids; **2010**; pp 43–60. https://doi.org/10.1021/bk-2009-1030.ch003.

(80) Hayyan, M.; Mjalli, F. S.; Hashim, M. A.; AlNashef, I. M.; Mei, T. X. Investigating the Electrochemical Windows of Ionic Liquids. *Journal of Industrial and Engineering Chemistry* **2013**, *19* (1), 106–112. https://doi.org/10.1016/j.jiec.2012.07.011.

(81) Kazemiabnavi, S.; Zhang, Z.; Thornton, K.; Banerjee, S. Electrochemical Stability Window of Imidazolium-Based Ionic Liquids as Electrolytes for Lithium Batteries. *J Phys Chem B* **2016**, *120* (25), 5691–5702. https://doi.org/10.1021/acs.jpcb.6b03433.

(82) Ge, R.; Hardacre, C.; Jacquemin, J.; Rooney, D. W. *Ionic Liquids: From Knowledge to Application*; UTC, **2023**; Vol. 13. https://pubs.acs.org/sharingguidelines.

(83) Nancarrow, P.; Al-Othman, A.; Mital, D. K.; Döpking, S. Comprehensive Analysis and Correlation of Ionic Liquid Conductivity Data for Energy Applications. *Energy* **2021**, *220*, 119761. https://doi.org/10.1016/j.energy.2021.119761.

(84) Yebra, F.; Troncoso, J.; Romaní, L. Thermal Conductivity of Ionic Liquids under Pressure. *Fluid Phase Equilib* **2020**, *515*. https://doi.org/10.1016/j.fluid.2020.112573.

(85) Nelson, W. M. *Chapter 3 Are Ionic Liquids Green Solvents?*; **2002**. https://pubs.acs.org/sharingguidelines.

(86) Hu, Y.; Xing, Y.; Yue, H.; Chen, T.; Diao, Y.; Wei, W.; Zhang, S. Ionic Liquids Revolutionizing Biomedicine: Recent Advances and Emerging Opportunities. *Chemical Society Reviews*. Royal Society of Chemistry September 26, **2023**, pp 7262–7293. https://doi.org/10.1039/d3cs00510k.

(87) El Abedin, S. Z.; Pölleth, M.; Meiss, S. A.; Janek, J.; Endres, F. Ionic Liquids as Green Electrolytes for the Electrodeposition of Nanomaterials. *Green Chemistry* **2007**, *9* (6), 549–555. https://doi.org/10.1039/b614520e.

(88) Egorova, K. S.; Gordeev, E. G.; Ananikov, V. P. Biological Activity of Ionic Liquids and Their Application in Pharmaceutics and Medicine. *Chemical Reviews*. American Chemical Society May 24, **2017**, pp 7132–7189. https://doi.org/10.1021/acs.chemrev.6b00562.

(89) Markiewicz, M.; Maszkowska, J.; Nardello-Rataj, V.; Stolte, S. Readily Biodegradable and Low-Toxic Biocompatible Ionic Liquids for Cellulose Processing. *RSC Adv* **2016**, *6* (90), 87325–87331. https://doi.org/10.1039/c6ra14435g.

(90) Ghazipour, H.; Gutiérrez, A.; Alavianmehr, M. M.; Hosseini, S. M.; Aparicio, S. Tuning the Properties of Ionic Liquids by Mixing with Organic Solvents: The Case of 1-Butyl-3-Methylimidazolium Glutamate with Alkanols. *J Mol Liq* **2022**, *347*, 117953. https://doi.org/10.1016/J.MOLLIQ.2021.117953.

(91) Costa, R.; Voroshylova, I. V.; Cordeiro, M. N. D. S.; Pereira, C. M.; Silva, A. F. Enhancement of Differential Double Layer Capacitance and Charge Accumulation by Tuning the Composition of Ionic Liquids Mixtures. *Electrochim Acta* **2018**, *261*, 214–220. https://doi.org/10.1016/j.electacta.2017.12.134.

(92) Philippi, F.; Rauber, D.; Eliasen, K. L.; Bouscharain, N.; Niss, K.; Kay, C. W. M.; Welton, T. Pressing Matter: Why Are Ionic Liquids so Viscous? *Chem Sci* **2022**, *13* (9), 2735–2743. https://doi.org/10.1039/D1SC06857A.

(93) Fillion, J. J.; Brennecke, J. F. Viscosity of Ionic Liquid-Ionic Liquid Mixtures. *J Chem Eng Data* **2017**, *62* (6), 1884–1901. https://doi.org/10.1021/acs.jced.7b00221.

(94) Vraneš, M.; Zec, N.; Tot, A.; Papović, S.; Dožić, S.; Gadžurić, S. Density, Electrical Conductivity, Viscosity and Excess Properties of 1-Butyl-3-Methylimidazolium Bis(Trifluoromethylsulfonyl)Imide + Propylene Carbonate Binary Mixtures. *Journal of Chemical Thermodynamics* **2014**, *68*, 98–108. https://doi.org/10.1016/j.jct.2013.08.034.

(95) Canongia Lopes, J. N.; Costa Gomes, M. F.; Husson, P.; Pádua, A. A. H.; Rebelo, L. P. N.; Sarraute, S.; Tariq, M. Polarity, Viscosity, and Ionic Conductivity of Liquid Mixtures Containing [C4C1im][Ntf2] and a Molecular Component. *Journal of Physical Chemistry B* **2011**, *115* (19), 6088–6099. https://doi.org/10.1021/jp2012254.

(96) Elstone, N. S.; Shimizu, K.; Shaw, E. V.; Lane, P. D.; D'Andrea, L.; Demé, B.; Mahmoudi, N.; Rogers, S. E.; Youngs, S.; Costen, M. L.; McKendrick, K. G.; Canongia Lopes, J. N.; Bruce, D. W.; Slattery, J. M. Understanding the Liquid Structure in Mixtures of Ionic Liquids with Semiperfluoroalkyl or Alkyl Chains. *Journal of Physical Chemistry B* **2023**, *127* (33), 7394–7407. https://doi.org/10.1021/acs.jpcb.3c02647.

(97) Clough, M. T.; Crick, C. R.; Gräsvik, J.; Hunt, P. A.; Niedermeyer, H.; Welton, T.; Whitaker, O. P. A Physicochemical Investigation of Ionic Liquid Mixtures. *Chem Sci* **2015**, *6* (2), 1101–1114. https://doi.org/10.1039/c4sc02931c.

(98) Annat, G.; Forsyth, M.; MacFarlane, D. R. Ionic Liquid Mixtures-Variations in Physical Properties and Their Origins in Molecular Structure. *Journal of Physical Chemistry B* **2012**, *116* (28), 8251–8258. https://doi.org/10.1021/jp3012602.

(99) Omar, S.; Lemus, J.; Ruiz, E.; Ferro, V. R.; Ortega, J.; Palomar, J. Ionic Liquid Mixtures - An Analysis of Their Mutual Miscibility. *Journal of Physical Chemistry B* **2014**, *118* (9), 2442–2450. https://doi.org/10.1021/jp411527b.

(100) Villar-Garcia, I. J.; Lovelock, K. R. J.; Men, S.; Licence, P. Tuning the Electronic Environment of Cations and Anions Using Ionic Liquid Mixtures. *Chem Sci* **2014**, *5* (6), 2573–2579. https://doi.org/10.1039/c4sc00106k.

(101) Plechkova, N. V.; Seddon, K. R. Applications of Ionic Liquids in the Chemical Industry. *Chemical Society Reviews*. **2008**, pp 123–150. https://doi.org/10.1039/b006677j.

(102) Ray, A.; Saruhan, B. Application of Ionic Liquids for Batteries and Supercapacitors. *Materials*. MDPI AG June 1, **2021**. https://doi.org/10.3390/ma14112942.

(103) Xiong, W.; Yin, Z.; Zhang, X.; Tu, Z.; Hu, X.; Wu, Y. Ionic Liquids Endowed with Novel Hybrid Anions for Supercapacitors. *ACS Omega* **2022**, *7* (30), 26368–26374. https://doi.org/10.1021/acsomega.2c02211.

(104) Watanabe, M.; Thomas, M. L.; Zhang, S.; Ueno, K.; Yasuda, T.; Dokko, K. Application of Ionic Liquids to Energy Storage and Conversion Materials and Devices. *Chemical Reviews*. American Chemical Society May 24, **2017**, pp 7190–7239. https://doi.org/10.1021/acs.chemrev.6b00504.

(105) Avid, A.; Ochoa, J. L.; Huang, Y.; Liu, Y.; Atanassov, P.; Zenyuk, I. V. Revealing the Role of Ionic Liquids in Promoting Fuel Cell Catalysts Reactivity and Durability. *Nat Commun* **2022**, *13* (1). https://doi.org/10.1038/s41467-022-33895-5.

(106) Kamijo, T.; Arafune, H.; Morinaga, T.; Honma, S.; Sato, T.; Hino, M.; Mizukami, M.; Kurihara, K. Lubrication Properties of Ammonium-Based Ionic Liquids Confined between Silica Surfaces Using Resonance Shear Measurements. *Langmuir* **2015**, *31* (49), 13265–13270. https://doi.org/10.1021/acs.langmuir.5b03354.

(107) Uçar, A.; Çopuroğlu, M.; Baykara, M. Z.; Arıkan, O.; Suzer, S. Tribological Interaction between Polytetrafluoroethylene and Silicon Oxide Surfaces. *J Chem Phys* **2014**, *141* (16). https://doi.org/10.1063/1.4898384.

(108) Gokturk, P. A.; Suzer, S. Probing the Dynamics of Non-Faradaic Processes in Ionic Liquids at Extended Time and Length Scales Using Xps with Ac Modulation. *Journal of Physical Chemistry C* **2021**, *125* (17), 9453–9460. https://doi.org/10.1021/acs.jpcc.1c01292.

(109) Lian, C.; Liu, K.; Van Aken, K. L.; Gogotsi, Y.; Wesolowski, D. J.; Liu, H. L.; Jiang, D. E.; Wu, J. Z. Enhancing the Capacitive Performance of Electric Double-Layer Capacitors with Ionic Liquid Mixtures. *ACS Energy Lett* **2016**, *1* (1), 21–26. https://doi.org/10.1021/acsenergylett.6b00010.

(110) Lian, C.; Liu, H.; Wu, J. Ionic Liquid Mixture Expands the Potential Window and Capacitance of a Supercapacitor in Tandem. *The Journal of Physical Chemistry C* **2018**, *122* (32), 18304–18310. https://doi.org/10.1021/acs.jpcc.8b05148.

(111) Paap, U.; Seidl, V.; Meyer, K.; Maier, F.; Steinrück, H.-P. Direct Correlation of Surface Tension and Surface Composition of Ionic Liquid Mixtures—A Combined Vacuum Pendant Drop and Angle-Resolved X-Ray Photoelectron Spectroscopy Study. *Molecules* **2022**, *27* (23), 8561. https://doi.org/10.3390/molecules27238561.

(112) Maier, F.; Cremer, T.; Kolbeck, C.; Lovelock, K. R. J.; Paape, N.; Schulz, P. S.; Wasserscheid, P.; Steinrück, H.-P. Insights into the Surface Composition and Enrichment Effects of Ionic Liquids and Ionic Liquid Mixtures. *Physical Chemistry Chemical Physics* **2010**, *12* (8), 1905. https://doi.org/10.1039/b920804f.

(113) Men, S.; Lovelock, K. R. J.; Licence, P. X-Ray Photoelectron Spectroscopy of Pyrrolidinium-Based Ionic Liquids: Cation–Anion Interactions and a Comparison to Imidazolium-Based Analogues. *Physical Chemistry Chemical Physics* **2011**, *13* (33), 15244. https://doi.org/10.1039/c1cp21053j.

(114) Men, S.; Hurisso, B. B.; Lovelock, K. R. J.; Licence, P. Does the Influence of Substituents Impact upon the Surface Composition of Pyrrolidinium-Based Ionic Liquids? An Angle Resolved XPS Study. *Physical Chemistry Chemical Physics* **2012**, *14* (15), 5229. https://doi.org/10.1039/c2cp40262a.

(115) Lockett, V.; Sedev, R.; Bassell, C.; Ralston, J. Angle-Resolved X-Ray Photoelectron Spectroscopy of the Surface of Imidazolium Ionic Liquids. *Physical Chemistry Chemical Physics* **2008**, *10* (9), 1330. https://doi.org/10.1039/b713584j.

(116) Thoms, E.; Sippel, P.; Reuter, D.; Weiß, M.; Loidl, A.; Krohns, S. Dielectric Study on Mixtures of Ionic Liquids. *Sci Rep* **2017**, *7* (1), 7463. https://doi.org/10.1038/s41598-017-07982-3.

(117) Lian, C.; Liu, H.; Wu, J. Ionic Liquid Mixture Expands the Potential Window and Capacitance of a Supercapacitor in Tandem. *The Journal of Physical Chemistry C* **2018**, *122* (32), 18304–18310. https://doi.org/10.1021/acs.jpcc.8b05148.

(118) Shin, S.; Greco, F.; Maier, F.; Steinrück, H.-P. Enrichment Effects of Ionic Liquid Mixtures at Polarized Electrode Interfaces Monitored by Potential Screening. *Physical Chemistry Chemical Physics* **2021**, *23* (18), 10756–10762. https://doi.org/10.1039/D0CP04811A.

(119) Oz, E.; Sahin, O.; Okur, H. I.; Suzer, S. Surface Propensity of Anions in a Binary Ionic-Liquid Mixture Assessed by Full-Range Angle-Resolved X-Ray Photoelectron Spectroscopy and Surface-Tension Measurements. *ChemPhysChem* **2020**, *21* (21), 2397–2401. https://doi.org/10.1002/cphc.202000750.

(120) Yin, S.; He, K.; Randle, M. D.; Barut, B.; Dixit, R.; Lipatov, A.; Sinitskii, A.; Bird, J. P. Probing the Dynamics of Electric Double Layer Formation over Wide Time Scales (10-9-10+5s) in the Ionic Liquid DEME-TFSI. *Journal of Physical Chemistry C* **2022**, *126* (4), 1958–1965. https://doi.org/10.1021/acs.jpcc.1c10067.

(121) Jia, M.; Broderick, A.; Newberg, J. T. The Influence of Water Vapor on the Electrochemical Shift of an Ionic Liquid Measured by Ambient Pressure X-ray Photoelectron Spectroscopy. *ChemPhysChem* **2021**, *22* (7), 633–640. https://doi.org/10.1002/cphc.202001041.

(122) Polat, E. O.; Balcı, O.; Kocabas, C. Graphene Based Flexible Electrochromic Devices. *Sci Rep* **2014**, *4* (1), 6484. https://doi.org/10.1038/srep06484.

(123) Park, K.; Chang, B.-Y.; Hwang, S. Correlation between Tafel Analysis and Electrochemical Impedance Spectroscopy by Prediction of Amperometric Response from EIS. *ACS Omega* **2019**, *4* (21), 19307–19313. https://doi.org/10.1021/acsomega.9b02672.

(124) Yin, S.; He, K.; Randle, M. D.; Barut, B.; Dixit, R.; Lipatov, A.; Sinitskii, A.; Bird, J. P. Probing the Dynamics of Electric Double Layer Formation over Wide Time Scales (10 –9 –10 +5 s) in the Ionic Liquid DEME-TFSI. *The Journal of Physical Chemistry C*

2022, *126* (4), 1958–1965. https://doi.org/10.1021/acs.jpcc.1c10067.

(125) Yun, C.; Hwang, S. Analysis of the Charging Current in Cyclic Voltammetry and Supercapacitor's Galvanostatic Charging Profile Based on a Constant-Phase Element. *ACS Omega* **2021**, *6* (1), 367–373. https://doi.org/10.1021/acsomega.0c04702.

(126) Uesugi, E.; Goto, H.; Eguchi, R.; Fujiwara, A.; Kubozono, Y. Electric Double-Layer Capacitance between an Ionic Liquid and Few-Layer Graphene. *Sci Rep* **2013**, *3* (1), 1595. https://doi.org/10.1038/srep01595.

(127) Singh, M.; Manoli, K.; Tiwari, A.; Ligonzo, T.; Di Franco, C.; Cioffi, N.; Palazzo, G.; Scamarcio, G.; Torsi, L. The Double Layer Capacitance of Ionic Liquids for Electrolyte Gating of ZnO Thin Film Transistors and Effect of Gate Electrodes. *J Mater Chem C Mater* **2017**, *5* (14), 3509–3518. https://doi.org/10.1039/C7TC00800G.

(128) Orazem, M. E.; Tribollet, B. *Electrochemical Impedance Spectroscopy*, 2nd ed.; John Wiley & Sons, **2017**.

(129) Aydogan Gokturk, P.; Ulgut, B.; Suzer, S. AC Electrowetting Modulation of Low-Volatile Liquids Probed by XPS: Dipolar vs Ionic Screening. *Langmuir* **2019**, *35* (9), 3319–3326. https://doi.org/10.1021/acs.langmuir.8b04099.

(130) Uzundal, C. B.; Gokturk, P. A.; Suzer, S.; Ulgut, B. Coarse-Grained Electrostatic Model Including Ion-Pairing Equilibrium That Explains DC and AC X-Ray Photoelectron Spectroscopy Measurements on Ionic Liquids. *Journal of Physical Chemistry C* **2019**, *123* (21), 13192–13200. https://doi.org/10.1021/acs.jpcc.8b11665.

(131) Kim, Y.-J.; Matsuzawa, Y.; Ozaki, S.; Park, K. C.; Kim, C.; Endo, M.; Yoshida, H.; Masuda, G.; Sato, T.; Dresselhaus, M. S. High Energy-Density Capacitor Based on Ammonium Salt Type Ionic Liquids and Their Mixing Effect by Propylene Carbonate. *J Electrochem Soc* **2005**, *152* (4), A710. https://doi.org/10.1149/1.1869232.

(132) Wang, X.; Salari, M.; Jiang, D.; Chapman Varela, J.; Anasori, B.; Wesolowski, D. J.; Dai, S.; Grinstaff, M. W.; Gogotsi, Y. Electrode Material–Ionic Liquid Coupling for Electrochemical

Energy Storage. *Nat Rev Mater* **2020**, *5* (11), 787–808. https://doi.org/10.1038/s41578-020-0218-9.

(133) Janssen, M.; Griffioen, E.; Biesheuvel, P. M.; van Roij, R.; Erné, B. Coulometry and Calorimetry of Electric Double Layer Formation in Porous Electrodes. *Phys Rev Lett* **2017**, *119* (16), 166002. https://doi.org/10.1103/PhysRevLett.119.166002.

(134) Lian, C.; Janssen, M.; Liu, H.; van Roij, R. Blessing and Curse: How a Supercapacitor's Large Capacitance Causes Its Slow Charging. *Phys Rev Lett* **2020**, *124* (7), 076001. https://doi.org/10.1103/PhysRevLett.124.076001.

(135) Wu, J. Understanding the Electric Double-Layer Structure, Capacitance, and Charging Dynamics. *Chem Rev* **2022**, *122* (12), 10821–10859. https://doi.org/10.1021/acs.chemrev.2c00097.

(136) Atkins, P.; De Paula, J.; Keeler, J. *Atkins' Physical Chemistry*, 11th ed.; Oxford University Press: London, England, **2017**.